Mechanically Alloyed Sm-Co Hard Magnetic Materials

by

Kathleen Gallagher

A thesis submitted to
the **University of Dublin**
in application for the degree of
Doctor of Philosophy

Department of Physics
University of Dublin
Trinity College

September 2002

DECLARATION

This thesis is submitted by the undersigned for examination for the degree of Doctor of Philosophy at the University of Dublin. It has not been submitted as an exercise for a degree at any other university.

This thesis, apart from the advice, assistance, and joint work mentioned in the acknowledgements and main text is entirely my own work.

I agree that the library may lend or copy this thesis freely on request.

_____

Kathleen Gallagher
September 2002

ACKNOWLEDGMENTS

This material is based upon work supported under a U.S. National Science Foundation Graduate Fellowship. The research was also supported by the European Union as part of the HITEMAG project.

I have come a long way from my first scientific experiments (investigating the effect of cooking oil on quality of popcorn) and although this volume only contains the work of 4 years, this Ph.D. has been more than 10 years in the making. It is only fitting then, that my acknowledgements should start with the people who got me started in this career path. I owe Mrs. Carole Palmer thanks for getting me interested in Science. She not only made chemistry classes interesting and encouraged me in my studies, but she also arranged for me to do research in a local foundry, Sandusky International. All of the R&D staff at Sandusky International were great, but I owe Al Castillo particular thanks for that experience. Two years of corrosion research not only lead to several state-level science awards, but also fostered my interest in Materials Science. Without that I would not have chosen to study materials in college.

In college at Carnegie Mellon I was able to continue my research interests thanks to Professors Mike McHenry and Sara Majetich who invited me to join their undergraduate research group, the CMU Buckyball Project. Mike and Sara encouraged my scientific interests then and helped to push me on to grad school. Of all the Buckyball group members, I owe thanks to Elaine Kirkpatrick and John Henry Scott. I won't forget the lesson of making undergrads change vacuum pump oil. Professor Majetich later recommended me for a summer position at Brookhaven National Laboratory working with Laura Lewis. Laura first introduced me to permanent magnets. She continually challenged me while I was there, and still does now while continuing to be a mentor. Thank you, Laura. Other people who have been helpful to me and whom I thank now are Matt Willard and Professors Marc De Graef and David Laughlin.

Now I turn to the present, and this work. I first thank Professor J.M.D. Coey for giving me the opportunity to live and study in Ireland. There have been many members of Group D over the years, and while I am grateful to all of them for their help, some deserve particular mention. I thank Dr. Vassil Skumryev, who started the Gd project, and Dr. Paul Smith who first started the mechanically alloyed Sm-Co work. Paul continues to answer any pesky questions on the subject that I have. I owe Dr. M. "Venki" Venkatesan a large debt of gratitude for his continued help and advice in my work. I really could not have done this without his guidance. I also want to thank Fernando Rhen, my fellow mechanical alloyer, for all the wonderful work he's done getting the high temperature VSM running, and for teaching me to use it. I thank James O'Sullivan, Amanda Barry O'Sullivan, and Rhian-Mari Thomas for introducing me to not only the lab, but also Dublin. We've come a long way since my days as Rhian's squatter. Thanks also to Gareth Hinds for introducing me to the joys of Leggs and Herbert Park soccer. Special thanks go to Ciara Fitzgerald and Cora O'Reilly for listening to my nearly daily accounts of the soap opera that is my life and just for the good times and

friendship. I also thank all other members of Group D, past and present, including Mazhar Bari, Laurent Clochard, Jiang Chengbao, Rui Borges, Treasa ní Mhíocháin, Janko Versluijs, Oscar Cespedes, Emma Kerr, Eoin Clifford, Guenole Jan, Rob Gunning, Alexis Douvalis and Steve Watts. I'll miss the coffee breaks and Sinterklaas.

More than a few people have paid extended visits to the group in the past four years. Of these people, I owe one summer student particular thanks. Anne le Gouil did much of the work on optimization of annealing, and made some of the alloys in this study. I also thank Professor Rex Harris for many very interesting discussions on my materials, and for reminding me of the importance of microstructural analysis. Other visitors that deserve mention are Raju and Billy Healy. While they haven't visited us to work in the lab, I also owe Dr. Nora Dempsey and Dr. Colin Tattam thanks for their continued encouragement, and for keeping HITEMAG meetings interesting.

Special thanks go to the technical staff of the Physics Department, without whom this work could not of been completed. First and foremost, I thank Jackie Armstrong, Mick O'Reilly, and Ken Concannon who continue to provide support in a timely manner (and they really know their stuff). I also thank John Kelly, Joe McCauley, Jemer, and Tom Burke. Tom, you will be missed. I also would like to thank the secretarial staff, who have been wonderful over the years, particularly Liz, Michelle, Susan, Gunilla and Michelle.

It has taken many friends outside of group D to keep me sane through all of this. First of all there have been all the members of the D.U. Ladies Association Football Club over the years, who I thank for everything. I particularly thank Paula Fitzell, Elly Mcpartlin, and Deirdre Moran, who have been there from the start. I also thank Billy Conlan and the girls at Trinity Sport and Leisure for giving me a game (and my first goal!). I thank Paul McCann and his sidekick Eoin O Cearbhaill for so much good fun, many good swims and weights sessions and for introducing me to water polo and the DUSC. Visits to the Luce Hall have become my daily de-stress. I thank all the staff there for this, but in particular I thank Peter Boland and Sorcha Stapleton not only for designing my exercise programs but also for being good friends over the last couple of years. I also thank my fellow regular in the Luce, Victor Chan.

Finally, my greatest thanks go to my family. The notes and care packages from my extended family, including Aunt Clara, Aunt Dee, Uncle Johnny, Aunt Amy, Grandpa Naffin, and Grandma and Grandpa Gallagher have been greatly appreciated over the years. My brothers, Ryan and Cullen, have been great fun since they grew up. I thank them for the good times, computer help, and mix CD's and I will forgive them for late birthday emails because they are both studying science. Oh, and thanks loads boys for eating all that popcorn all those years ago. I am so grateful to my parents, Bill and Nora. They have always encouraged and pushed me academically, and always made me believe I could do anything. How could they have known where dad's idea for the popcorn experiment would take me?

Thank you all for everything.

TABLE OF CONTENTS

SUMMARY

In the recent search for new high-temperature permanent magnet materials, research has concentrated on bulk Sm_2Co_{17}-type magnets. The usual approach to development of coercivity in bulk Sm-Co based materials is to prepare a nanophase cellular microstructure with cell walls that act as pinning sites (precipitation hardening). An alternative approach is to mechanically alloy the materials, with the goals of reducing particle size, forming metastable phases, and introducing planar crystalline defects that act as pinning sites. The objectives of this work were to produce SmZr(Co,Fe) alloys by mechanical alloying, to study the effect of composition on magnetic properties, and to assess whether these materials would make good high temperature magnets.

In this work, $Sm_zZr_y(Co_{1-x}Fe_x)_{100-z-y}$ nanocrystalline powders, where $13 \leq z \leq 15$, $0 \leq y \leq 5$, and $0 \leq x \leq 0.5$ (compositions intermediate to $SmCo_5$ and Sm_2Co_{17}), were prepared by mechanical alloying followed by an optimized annealing procedure. Powder particles were roughly spherical and ranged in size from a few micrometers in size up to 20 μm. X-ray diffraction patterns showed that the as-milled powders were amorphous, or had some very small α-Fe crystallites < 10 nm in size, depending on composition. Annealed samples showed a mixture of Sm_2Co_{17} (Th_2Ni_{17} and Th_2Zn_{17} structures) and $SmCo_5$ nanocrystalline phases, in relative amounts dependent on composition. Substitution of Fe increases the grain size and favors the formation of Sm_2Co_{17}. Addition of Zr has the opposite effect: it decreases the grain size and favors the formation of $SmCo_5$.

Room temperature hysteresis loops for all compositions studied show smooth demagnetization curves and enhanced remanence ($\sigma_r/\sigma_s > 0.60$) is achieved in all compositions, indicating intergrain exchange coupling among the fine grains. Coercivity peaks in all $Sm_x(Co_{1-z}Fe_z)_{100-x}$ for $z = 0.1$, and hence Fe content was fixed at $z = 0.1$ for studies of Zr substitution. With Zr content, coercivity increased, probably due to a decrease in grain size and an increase in the amount of $SmCo_5$ phase present. Increased Zr content caused

remanence and energy product to decrease. Maximum room temperature coercivity of 1.74 T is obtained in the composition $Sm_{14}Zr_3(Co_{0.9}Fe_{0.1})_{83}$, while a maximum energy product of 100 kJ/m^3 is achieved in $Sm_{13}Zr(Co_{0.9}Fe_{0.1})_{86}$.

A systematic investigation of magnetic properties in the temperature range $20^oC \leq T \leq 500^oC$ was carried out on compositions with x = 0.1, and various Sm and Zr contents. High temperature magnetic measurements show that the properties degrade irreversibly at temperatures above 300ºC. Loops taken at low temperature after measurement change from that of a single magnetic phase to that of a two-phase mixture. This behavior is attributed both to grain growth and to a phase change in the material at these temperatures.

Finally, magnetization reversal in these materials was investigated through measurement of virgin magnetization, recoil, and magnetic viscosity, allowing calculation of S_v and activation volume, V_a. Calculation of total susceptibility, χ_{tot} shows that these materials undergo a very sharp reversal, with the exception of the binary compound, which shows reversal of a small amount of soft material in low fields. Virgin curves and plots of reversible magnetization vs. irreversible magnetization show that there is actually very little pinning in the materials. Unlike bulk $Sm_2(Co, Fe, Cu, Zr)_{17}$-type pinning-controlled materials, these materials have a nucleation controlled nature. Calculated V_a for mechanically alloyed $Sm_{14}Zr(Co_{0.9}Fe_{0.1})_{85}$ is larger than the activation volume for commercial $Sm_2(Co, Fe, Cu, Zr)_{17}$ materials. This is because, in the absence of pinning sites, a larger volume of materials is involved in the reversal.

1 INTRODUCTION

Permanent magnets can be found everywhere today. They are used extensively in motors, generators, loudspeakers, bearings, and actuators. Of the many different permanent magnet materials, those based on alloys of rare earths and transition metals exhibit high uniaxial anisotropies, high flux densities, and high energy products. Magnets based on $Nd_2Fe_{14}B$ have the highest energy products achieved so far in permanent magnets. This fact combined with their low cost compared to that of Co-based magnets (Fe is the most abundant metal on Earth and therefore cheap) has lead to extensive use of $Nd_2Fe_{14}B$ based materials. Unfortunately, these recently developed magnets have one major drawback in that their Curie temperature is fairly low, at 312°C. Recent developments in the aeronautics industry demand magnets that can operate at temperatures in the range 400 - 500°C. Applications that will need these high temperature magnets include an IPU for electric aircraft, magnetic bearings for gas turbine engines and space power applications, and high speed starter/generator systems for unmanned combat air vehicles. These applications will be operating at high speed in high stress, high temperature, and sometimes air-only cooled environments[8]. This new demand has caused research on permanent magnets to be refocused on magnets based on Sm-Co alloys, which have Curie temperatures in the range 1000 K - 1200 K.

This work is a part of the EU funded project HITEMAG, a collaboration between NSRC Demokritos, Magnetfabrik Bonn, University of Birmingham, Magnequench, TU Vienna, IJS Ljubljana, CNRS Grenoble, FIT, Cykris, IFW Dresden, Less Common Metals, and Trinity College Dublin. The goal of HITEMAG is the development of permanent magnetic materials capable of operating at temperatures up to 400°C. These materials will not only need to have a high Curie temperature, and large room temperature coercivity, but they will also need to have a large coercivity at the operating temperature and good temperature dependence of the magnetic properties.

1.1 THE BASICS

1.1.1 Origin of Magnetic Moments

Ferromagnetism is the result of ordering of atomic magnetic moments. Atoms derive their magnetic moments from electrons, which have two sources from which a magnetic moment can be obtained. The first source is currents associated with orbital motion of the electrons around the nuclei (the orbital angular momentum). The magnitude of this moment can be obtained from a current loops analogy, and yields a moment of evR/2 where e is the charge of the electron, v is its velocity, and R is the radius of the orbit. The angular momentum (= $m_e v$R where m_e is the mass of the electron) is quantized. Consequently, the magnetic moment is quantized in units of the Bohr Magneton

$$\mu_B = \frac{e\hbar}{2m_e} = 9.274 \times 10^{-24}\ \text{A m}^2 \ . \tag{1.1}$$

The second source of the magnetic moment of electrons is based on the spin angular momentum, ħ/2, of the electrons. It can be shown that the spin moment is given by

$$\mu_S = \sqrt{3}\mu_B \ . \tag{1.2}$$

The orbital and spin magnetic moments combine into a resultant magnetic moment through the spin-orbit interaction. This results from interaction of the magnetic fields produced by orbital motion and spin motion. As a result, L and S, the orbital and spin quatum numbers of the atom, respectively, couple to form the total angular momentum. $J = L + S$ if the shell is more than half full, and $J = L - S$ if the shell is less than half full. The magnetic moment of an ion is then

$$\mu = -g\mu_B J \tag{1.3}$$

where g is given by the Landé equation

$$g = 1 + \frac{J(J+1) + S(S+1) - L(L+1)}{2J(J+1)} \ . \tag{1.4}$$

This description is valid for free atoms or ions. However, when the atom is incorporated into a solid, there is an additional electrostatic interaction with

the surrounding atoms, known as the crystal field. If the crystal field interaction is stronger than the spin-orbit interaction, then the atomic current loops are disrupted, and the orbital magnetic moment is said to be quenched. This is the case for 3d ferromagnets such as Fe, Ni, and Co, which derive their magnetic moments from electrons in the outermost 3d subshell. Their moments are due entirely to spin. The opposite occurs for the rare earths. The magnetic moments of these elements are due to the 4f subshells, which are seated inside the 5s and 5p subshells. The magnetic electrons are so well screened from the crystal fields that there is no quenching of the orbital moment.

More detailed descriptions can be found elsewhere. See, for example, Chen's Magnetism and Metallurgy of Soft Magnetic Materials[1], or Skomski and Coey's Permanent Magnetism[2].

1.1.2 Aligning the Moments

Any observed net magnetization in a material is the result of an interaction between the atomic magnetic moments that results in an alignment. This is first understood by considering a paramagnetic system, i.e. a system with magnetic moments that have no alignment mechanism other than application of an external magnetic field.

1.1.2.1 Langevin Paramagnetism

Consider a paramagnetic system containing N magnetic atoms each with a magnetic moment μ. The component of the magnetic moment must be quantized in the direction of the magnetic field H. Based on this, the Langevin theory of paramagnetism shows that the average magnetization in a magnetic field M is given by

$$M = NgJ\mu_B\left(\frac{2J+1}{2J}\coth\frac{2J+1}{2J}\alpha - \frac{1}{2J}\coth\frac{\alpha}{2J}\right), \quad (1.5)$$

where

$$\alpha = \frac{g\mu_0\mu_B JH}{k_B T}, \quad (1.6)$$

$k_B = 1.38 \times 10^{-23}$ J/K is the Boltzman constant, and T is the absolute temperature. The function in parentheses is known as the *Brillouin function* and is denoted by $B_J(\alpha)$.

If an infinitely strong field is present or at temperatures near absolute zero, M will approach a saturation value. Under these conditions, coth $\alpha \rightarrow 1$ and hence $B_J(\alpha) \rightarrow 1$. Then

$$M_S = NgJ\mu_B \ . \tag{1.7}$$

For $\alpha << 1$, the Brillouin function can be expanded as

$$B_J(\alpha) = \frac{J+1}{3J}\alpha - \frac{\left[(J+1)^2 + J^2\right](J+1))}{90J^3}\alpha^3 + \ldots \ . \tag{1.8}$$

Taking only the first term for the Brillouin function, the susceptibility, χ=M/H is now given by

$$\chi = \frac{Ng^2 J(J+1)\mu_0^2 \mu_B^2}{3kT} = \frac{C}{T} \tag{1.9}$$

This is known as the *Curie law*, and the constant $C = Ng^2J(J+1)\mu_B^2/3k$ is the *Curie constant*, so named because Pierre Curie first observed that the susceptibility of paramagnetic materials is inversely proportional to temperature.

1.1.2.2 Weiss Theory of Ferromagnetism

The Weiss theory of ferromagnetism postulates the existence of an internal field H_w in ferromagnetic materials. This so-called *molecular field* is responsible for the parallel coupling of atomic moments. The intensity of the molecular field is assumed to be proportional to the magnetization, i.e. $H_w = \lambda M$. Now M is still

$$M = NgJ\mu_B B_J(\alpha), \tag{1.10}$$

but now α is given by

$$\alpha = \frac{g\mu_0\mu_B J(H + \lambda M)}{k_B T} \ . \tag{1.11}$$

Both equations 1.10 and 1.11 must be solved simultaneously with the same value of α. Now the susceptibility is given by

$$\chi = \frac{C}{T - T_c}, \tag{1.12}$$

where $T_c = \lambda C$ is the Curie temperature, or the temperature above which the long-range magnetization of a ferromagnet vanishes due to thermal agitation. The Curie temperature is an intrinsic property of a material.

The Weiss model accurately predicts ferromagnetism, but it does not explain the physical origin of the molecular field. Heisenberg first explained this in terms of a positive exchange interaction between spins in neighboring atoms[3]. This interaction is a strictly quantum mechanical effect and is of an electrostatic nature. The exchange interaction energy U_{ij} between two atoms with spins $\mathbf{S_i}$ and $\mathbf{S_j}$ is given by

$$U_{ij} = -2J_{ij}S_i \cdot S_j \tag{1.13}$$

where J_{ij} is the exchange integral and is related to the overlap of the charge distributions of the two atoms. Depending on the sign of J_{ij}, a parallel or anitparallel spin arrangement will occur. Understanding this force requires the Pauli exclusion principle, which states that the overall wave function for a quantum state must be antisymmetric. The relative displacement of two spins is determined by their spin configurations. This displacement changes the Coulomb energy between the electrons.

1.1.3 Magnetocrystalline Anisotropy

When a ferromagnetic material is subjected to an applied field, the observed magnetization depends both on the magnitude of the field and the crystallographic direction along which the field is applied. The preference for a magnetic moment to lie along a certain crystallographic direction is known as the *magnetocrystalline anisotropy* and is an intrinsic property of the material. Each material has a crystallographic direction for which the magnetization reaches its saturation value, M_s, in lower applied fields than for other directions. This direction is known as the easy direction (or easy axis); correspondingly, the direction that takes the largest applied field to reach M_s is called the hard direction. For simple ferromagnetic materials, there may be more than one equivalent easy direction determined by the crystal system. For

example, Fe, with its body centered cubic structure and (001) type anisotropy has 3 easy axes because there are 3 equivalent (001) axes in the cubic system. Ni, which has a fcc structure and (111) type anisotropy has four equivalent easy axes. Co, on the other hand, has only one easy axis because of its uniaxial hexagonal close packed structure. For systems with more than one magnetic element, determination of the number of easy axes can be more complicated. For permanent magnetic systems it is usually desirable to have a uniaxial system, so that there is only one easy axis.

The magnetocrystalline anisotropy energy for a uniaxial crystal is expressd

$$E_a = K_1 \sin^2\theta + K_2 \sin^4\theta + \cdots \qquad (1.14)$$

where θ is the angle between the magnetization direction and the easy direction and K_1 and K_2 are anisotropy constants. The field required to rotate the magnetization vector 90º away from the easy direction is defined by the anisotropy field and is given by

$$H_A = \frac{2K_1}{\mu_0 M_S} \ . \qquad (1.15)$$

1.1.4 Domains

Though ferromagnetic materials are spontaneously magnetized, they may show no observable magnetization. This is due to the existence of magnetic domains, regions in a ferromagnetic material over which all moments are parallel. Domains form spontaneously to reduce the magnetostatic energy that results from leakage of magnetic flux into the surrounding airspace. The domains reduce the magnetostatic energy by confining magnetic flux within the magnetic body. However, formation of domains requires the formation of domain walls, surfaces where the orientation of the magnetization changes abruptly (within 10 – 100 nm). This costs energy. Consequently, the final domain structure is a result of balancing of magnetostatic, domain wall, magnetocrystalline, and exchange energies. Formation of domain walls is illustrated in Figure 1.1.

The domain wall energy, γ, is a balance of competing exchange and anisotropy energies, $\gamma = \gamma_{ex} + \gamma_a$. It can be shown that

$$\gamma = \sqrt{AK_1} \ , \tag{1.16}$$

where A is the exchange constant and K_1 is the first magnetocrystalline anisotropy constant for the material. The width of the domain wall is also determined by the balance between exchange and anisotropy energies and is given by

$$\delta_w = \pi \sqrt{\frac{A}{K_1}} \ . \tag{1.17}$$

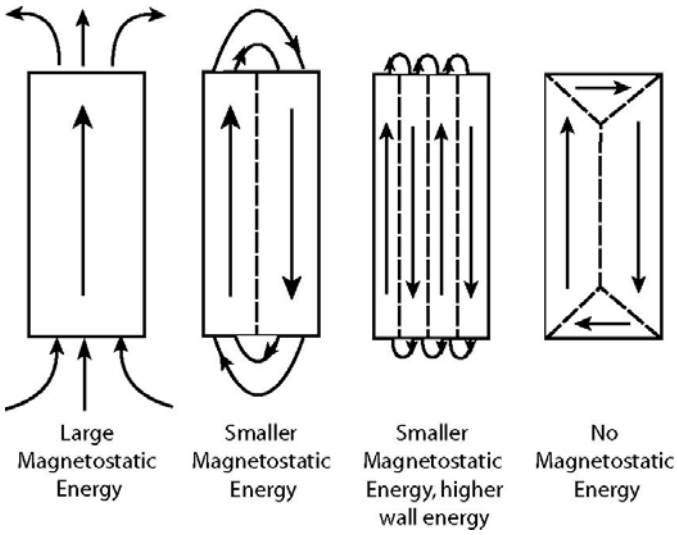

Figure 1.1. Formation of domains in a ferromagnetic material. The single domain state (left) has high magnetostatic energy. Introduction of 180º domain walls reduces magnetostatic energy, but raises wall energy. Introduction of 90º closure domains eliminate the magnetostatic energy, but increase anisotropy energy.

1.1.5 The Hysteresis Loop

A magnetic material can be characterized by measuring its magnetization, M, as a function of external applied field, H. A schematic M(H) curve, also known as a hysteresis loop, is shown in Figure 1.2(a). The material starts in a demagnetized state (domains canceling to zero magnetostatic energy). With application of a small field, reversible rotation of magnetization within the domain and reversible motion of domain walls

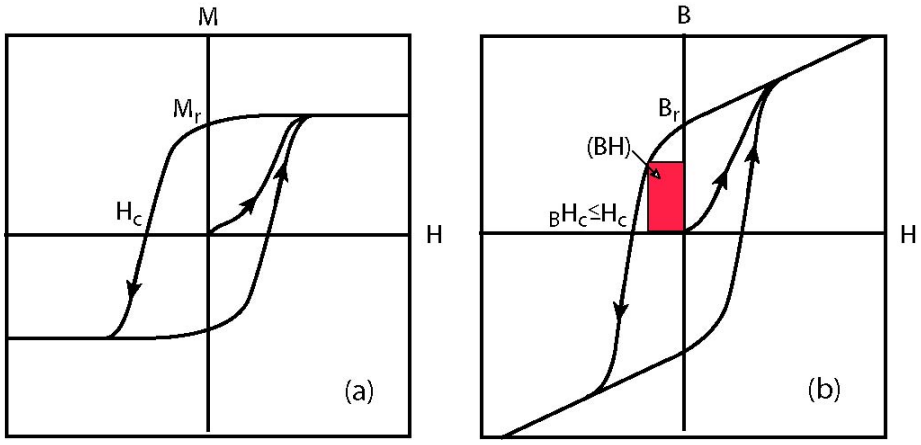

Figure 1.2. (a) M(H) loop of a permanent magnetic material, and (b) B(H) loop of a permanent magnetic material. The red rectangle in the second quadrant represents the energy product. The two plots are related by the equation $B = \mu_0(M+H)$

occurs. As the field increases, domains with their moments aligned parallel to the applied field grow at the expense of domains with other orientations due to irreversible domain wall motion. This part of the curve is referred to as the *virgin curve*, or *initial magnetization curve*. At sufficiently high field, the spontaneous magnetization is reached and there are no longer domain walls. The material is then uniformly magnetized with $M = M_s$.

When the external magnetic field is removed, the value of magnetization measured is non-zero and is called the remanent magnetization M_r. The magnitude of this remanent magnetization depends upon the distribution of easy axes in the material. For a perfectly aligned material, the remanent magnetization is equal to the spontaneous magnetization, and $M_r/M_s = 1$. For a material with isotropic orientation of grains, this ratio, called the remanence ratio, is $M_r/M_s = 0.5$.

When a sufficiently large reverse field is applied, the magnetization will be reduced to zero at the coercivity, H_c. This occurs by non-reversible rotation of the magnetization or by the nucleation and propogation of reverse domains. The coercivity is a measure of the magnet's resistance to demagnetization by reverse fields. Coercivity mechanisms will be discussed in more detail later. The coercivity, H_c, of the M(H) loop is known as the intrinisic coercivity and is sometimes labelled $_iH_c$ or H_{ci}.

Both M_r and H_c are extrinsic properties. They depend on particle size and shape and microstructure. Permanent (or hard) magnet materials are distinguished from soft magnetic materials by their high values of coercivity, $H_c \geq M_s/2$.

The figure of merit for permanent magnet materials is the energy product, $(BH)_{max}$. This is defined as the maximum product of B and H in the second quadrant of the B(H) loop. B is the magnetic flux density and is related to M, the magnetization by

$$B = \mu_0 (M + H) \tag{1.18}$$

where $\mu_0 = 4\pi x10^{-7}$ H·m^{-1} is the permeability of free space.

A schematic B(H) loop is shown in Figure 1.2(b). To distinguish the coercivity of this B(H) loop from the intrinisic coercivity, the symbol $_BH_c$ is sometimes used. Generally $_BH_c \leq H_c$. The energy product is frequently represented as the largest rectangle that will fit into the second quadrant of the B(H) loop, as shown in Figure 1.2(b). It is a measure of how much magnetic flux a magnet can provide.

The magnetization of an ideal permanent magnet should not be influenced by the magnetic field. In reality, M and H cannot be entirely independent. Dipole fields from poles at the surfaces of a magnet oppose the magnetizing field so the internal field that M responds to is less than the applied field. This dipole field is called the *demagnetizing field* H_d. The internal field is the sum of the applied field and the demagnetizing field, $H_{int} = H + H_d$, and $H_d = -DM$. D is called the *demagnetizing factor*, and is a function of the shape of the magnet. For an infinitely long cylinder magnetized along its length, D = 0. If it is magnetized perpendicular to its length, D = ½. A sphere has D = 1/3 along each of its three orthogonal axes.

1.2 PERMANENT MAGNET DEVELOPMENT

An exponential growth in $(BH)_{max}$ has been achieved over the last century through discovery of new materials and improved processing routes (Figure 1.3). At the start of the twentieth century, carbon steels were the most widely used permanent magnets. The energy product of steels was improved in the first few decades of the century with the discovery of the Co magnet

steels, and steels based on Co-Mo and Co-Cr showed energy products[4] of around 8 kJ/m^3.

In the 1930s, a family of Fe-Al-Ni-Co alloys, known as the Alnicos, was developed. The Alnicos showed much higher coercivity than the steels used at the time, but had a similar energy product. Their development is significant, however, because the Alnicos were the first truly hard magnetic materials. Their coercivity is due to the complex microstructure that is developed on spinodal decomposition of the alloy from a single phase into a Fe-rich phase and a bcc Ni-Al rich phase[4]. The result of this spinodal decomposition is a microstructure composed of two interpenetrating networks of rods of Fe and NiAl. Coercivity is a result of the shape anisotropy of the Fe rods. Co is usually added to increase M_s and T_c of the Fe phase.

The next significant development in permanent magnet materials came with the development in the 1950s of synthetic hard ferrite materials, usually $BaFe_{12}O_{19}$ or $SrFe_{12}O_{19}$. Fe cations in these materials interact through an antiferromagnetic superexchange interaction via an oxygen anion. The structure includes cation sublattices with unequal populations, giving rise to a ferrimagnetic structure[2]. Consequently, these hexagonal ferrites have strong uniaxial anisotropy, but they do not achieve high energy products. However, the ferrites are cheap and effective magnets. Today they still account for roughly 90% of the market by mass, and 50% by value.

The greatest advances came with the discovery of magnetic materials

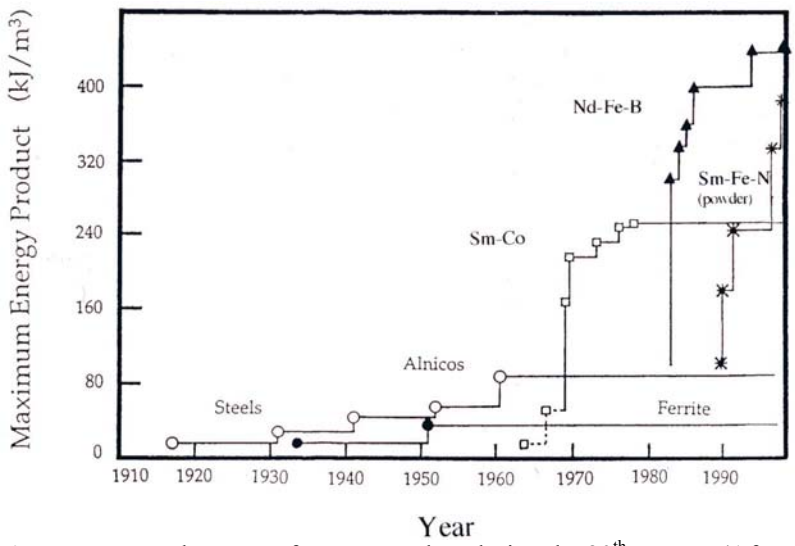

Figure 1.3. Development of energy product during the 20th century (After R. Skomski and J.M.D. Coey, 1999)

based on alloys of rare earths and transition metals in the late 1960s. Interestingly, the Manhattan Project set the groundwork for this by first making it possible to separate the rare earths, which are usually found mixed together in ores. Even more interesting is the fact that Karl Strnat, who discovered these alloys in 1966[5], was actually trying to find a good soft magnetic material. The first rare earth magnet was produced in 1967, when Velge and Buschow succeeded in bonding $SmCo_5$ in resin to yield an energy product[6] of 65 kJ/m^3. It was soon discovered that small substitutions of Cu lead to the precipitation of a nonmagnetic phase that pinned domain walls an hence increased coercivity. The additional Cu also allowed for substitution of Fe into $SmCo_5$.

The idea of magnetic hardening by Cu precipitates in $Sm(Co, Fe, Cu)_z$ was extended from z = 5 to z = 7.2 - 8.5, leading to the development of the second generation of Sm-Co magnets in the mid 1970s. These magnets were based on the Sm_2Co_{17} phase. The important discovery that Zr promoted formation of the cellular microstructure observed in $Sm(Co, Fe, Cu)_z$ magnets where domains were pinned at $SmCo_5$ boundaries surrounding the Sm_2Co_{17} phase made it possible to achieve energy products in excess of 200 kJ/m^3. These magnets opened the door for applications where miniaturization was needed.

Political difficulties with the world cobalt supply in the late 1970s caused a push for a cheaper rare earth magnetic material. It was obvious to look at Fe and Nd, because Fe is the most abundant metal on Earth, and Nd is the most abundant magnetic light rare earth[6]. However, there is not a suitable binary alloy of Nd and Fe. In 1983, both Sumitomo Special Metals and General Motors Research Laboratories announced success in manufacturing magnets based on the $Nd_2Fe_{14}B$ intermetallic phase. The first magnets based on this phase had energy products of around 300 kJ/m^3.

Over the last two decades, improvement in the properties of rare earth magnets has occurred primarily through control of the alloy composition and processing techniques. A record high energy product of 451 kJ/m^3 was reported this year for a Nd-Fe-B alloy[7]. This result was achieved through careful control of the microstructure.

In recent years, focus in rare earth magnets research has returned to the Sm-Co alloys. There was very little work in the area for over a decade after the discovery of $Nd_2Fe_{14}B$. In 1996, the United State Air Force sponsored a research initiative in high temperature magnetic materials that included military, industrial, and academic laboratories. A similar project was started in Europe in 1999 (this work is part of that project). The goal of these projects was to develop materials that operate at temperatures in excess of 400ºC. Consequently, research needed to focus on the Sm_2Co_{17}-based materials, with Curie temperatures in the range of 800 – 900ºC, rather than the $Nd_2Fe_{14}B$-based materials that only had Curie temperatures around 300ºC. Fingers and Rubertus present a good review of applications that require high temperature magnets[8].

1.3 COERCIVITY

Along with energy product, coercivity is a key measure of the quality of a permanent magnet. Consequently, it is useful to understand the mechanisms of coercivity and magnetization behavior, so the information can be used to develop better permanent magnetic materials.

1.3.1 Types of Magnetization Behavior

Magnetization reversal of small crystals comprising real magnets generally proceeds by domain wall motion. It is usual to distinguish between two basic behavior patterns and accordingly classify magnets as "nucleation controlled" or "pinning controlled." The two types can be identified by typical initial magnetization curves and the dependence of the remanence and intrinsic coercivity on peak magnetizing field. These two types of behavior are the limiting cases; some magnets are of “mixed type”, as in the case of high H_c Sm_2Co_{17}-type magnets.

1.3.1.1 Nucleation Controlled

In nucleation controlled magnets, the movement of existing domain walls within a given grain is easy, while the "nucleation" of a reversed domain after removal of the walls is difficult[9]. Figure 1.4 shows schematic

magnetization curves for the two types. For nucleation controlled magnets, the low-field susceptibility of the virgin curve is large, providing a measure of the reversible displacement of walls[10]. Minor loops indicate mostly reversible wall motion and low remanence and coercivity. As the magnetizing field H_m is increased, B_r rises slowly and H_{ci} rises even more slowly. Grains are increasingly cleared of domain walls and reversed domains must be formed at the nucleation field H_N before its magnetization can be reversed. Very high magnetizing fields are required to fully develop the best possible major demagnetization curve. Unfortunately, the details of the nucleation process are still unclear. Researchers argue whether a truly new nucleus is formed in a previously saturated grain, or whether the reversal starts from a highly compressed residual domain left from the prior opposite magnetization state[11]. Nucleation controlled behavior is characteristic of binary $SmCo_5$.

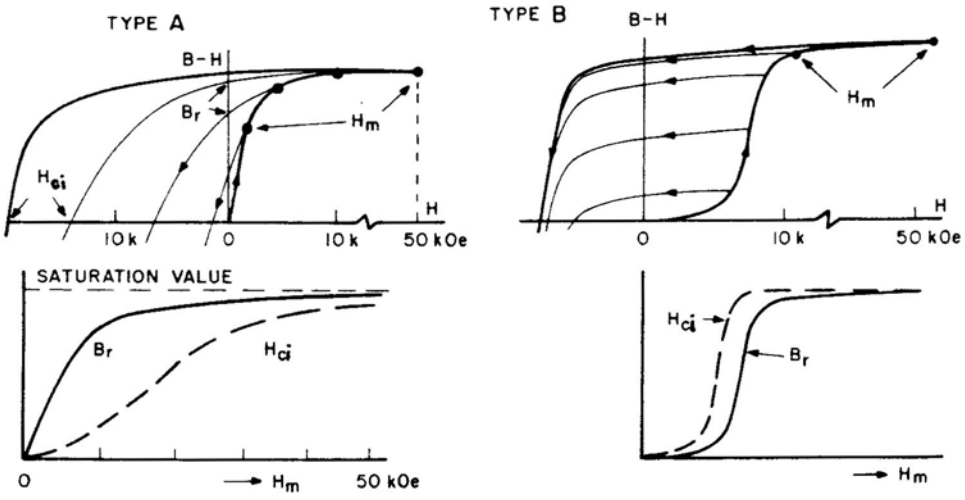

Figure 1.4. Schematic magnetization curves for "nucleation controlled" magnets, type A, like $SmCo_5$; and for "pinning controlled" magnets, type B, like Sm (Co, Cu, TM)$_x$. (after K.J. Strnat and R.M.W. Strnat 1991)

1.3.1.2 Pinning Controlled

In pinning controlled magnets, small reversed domains exist in all grains at all times or they form easily in low demagnetizing fields, but obstacles present in most of the magnet volume strongly impede the movement of walls. The presence of defects or magnetic inhomogeneities that act as pinning centers inside the grain has important consequences for the low-field behavior.

The initial susceptibility is very low until the field is sufficiently high to allow the walls to overcome the potential barriers associated with the pinning centers[10], at which point the curve rises to near saturation in a narrow range of H_m. When H is reduced and reversed, there is little magnetization change until the negative field range near H_{ci} is reached. The coercive field and remanence of minor loops remains low at first, then rise steeply as H_m is increased. The homogeneous precipitates inside the main phase grains pin walls wherever they are located, and therefore are responsible for this behavior. For the precipitates to be effective pins they must be crystallographically coherent, have basic magnetic properties that differ significantly from those of the matrix phase, and they must have the right size and spacing[9]. This type of behavior is characteristic of low coercivity $Sm_2(Co, Fe, Cu, Zr)_{17}$ magnets.

1.3.1.3 Mixed

Magnets based on $Sm_2(Co, Fe, Cu, Zr)_{17}$ with very high coercivity show another form of the virgin curve, as illustrated in Figure 1.5. Strnat[9] calls this "mixed type", but that name is perhaps a bit misleading. This behavior occurs when the domain wall pinning strength is non-uniform[12], and has been interpreted as a mixture of localized and homogeneous wall pinning[11].

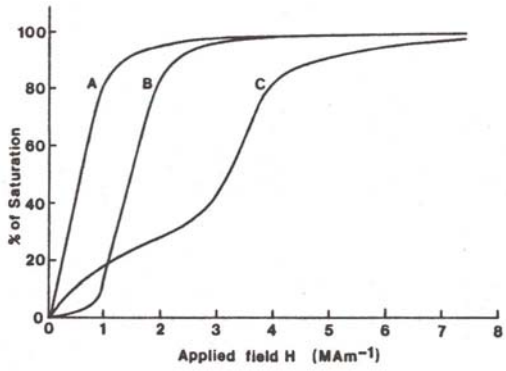

Figure 1.5. Comparison of the virgin magnetization curves for typical magnets of three basic behavior types. A is nucleation controlled; B is pinning controlled; and C is mixed (or pinning with very nonuniform pin strength). (After R.A. McCurrie, 1994)

1.3.2 Magnetization Reversal and Magnetic Viscosity

When a uniformly magnetized grain is placed in a reversed field less than H_c, its state corresponds to a metastable energy minimum. The state where the magnetization is parallel to the direction of the applied field is more stable. Between these two minima there exists an energy barrier, as illustrated in Figure 1.6. This barrier is the origin of coercivity. The existence of this barrier implies an anisotropy of the magnetic energy. This anisotropy can have two origins. The first is atomic-scale anisotropy acting on the individual moments; this is due to local dipolar or magnetocrystalline interactions. The second origin is macroscopic scale anisotropy acting on the magnetization; this is due to anisotropy of the demagnetizing field, related to the shape of the grains[13].

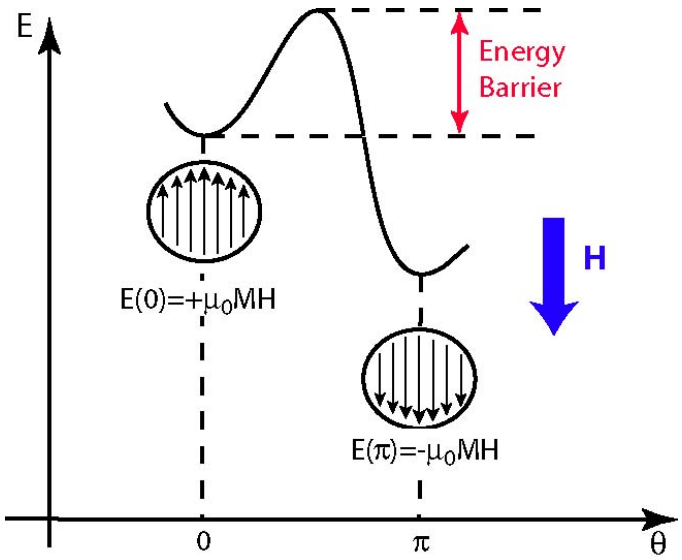

Figure 1.6. The metastable coercive state for θ=0 and the energy barrier for a magnet

Before discussing magnetization reversal in a real material, it is useful to consider the single grain of a homogenous material in more detail. If the system has strong magnetocrystalline anisotropy the movement of any of the magnetic moments away from their equilibrium position costs energy. Reversal can occur either by *uniform coherent rotation*, where all moments remain parallel and rotate in unison, or by some nonuniform process. In the former, the moments must pass by the hard direction, and so H_c is equal to the

anisotropy field H_a. This process was first analyzed in detail by Stoner and Wohlfarth[14] for ellipsoidal grains, and is a basic model for analysis of magnetization reversal. Any nonuniform processes cost more energy than uniform coherent rotation because of additional exchange and dipolar energy terms that become significant when the moments are not parallel to each other.

If the system has no magnetocrystalline anisotropy, then shape anisotropy dominates. Consider again a single ellipsoidal grain of homogenous material that is initially saturated. Shape anisotropy is due to the fact that the energy of the sample in its demagnetizing field is minimum when **M** is parallel to the major axis of the ellipsoid and maximum perpendicular to the major axis. For uniform coherent rotation, when the ellipsoid is subjected to an increasing reverse field H_c is equal to the shape anisotropy field, $H_a^{sh} = (N_{\perp} - N_{\parallel})M_s$ where $N_{\parallel}$ and $N_{\perp}$ are demagnetizing factors parallel and perpendicular to the major axis of the ellipsoid[13]. Processes other than uniform coherent rotation may occur, but these processes cause a loss of exchange energy.

Magnetocrystalline and shape anisotropies coexist in nearly all magnets. In a homogeneous material magnetization reversal through uniform coherent rotation occurs in a field equal to the total anisotropy field, $H_a^{tot} = H_a + H_a^{sh}$. In real systems, the shape anisotropy barrier can often be bypassed less expensively through a nonuniform process. In addition, real systems are seldom homogeneous. Structural heterogeneities lead to the existence of small critical volumes where magnetization reversal is nucleated before spreading across the system[13]. These non-collective processes are important in materials with high magnetocrystalline anisotropy because they allow the magnetization to be reversed without having to pay the very large anisotropy energy[15].

In a real hetereogeneous material, magnetization reversal starts with the nucleation of a domain of reverse magnetization on a defect within a grain that has a lower anisotropy barrier than the bulk. This first nucleus is a local magnetic deviation from saturation, and consequently, the characteristic length for such a deviation is the domain wall width[13] δ_w. Reversal continues as the domain wall passes from the defect into the bulk and then expands. There is

possible pinning of the domain wall on defects or magnetic heterogeneities known as pinning sites[†].

Temperature affects these processes firstly, by changing the intrinsic magnetic properties K_1 and M_s that define the height of the barriers, and secondly by providing energy that can overcome some energy barriers locally. This can be observed as a time dependence of magnetization of the material at constant field, known as the *magnetic viscosity* or *magnetic after-effect*.

Two main approaches to describe coercivity in rare-earth magnets have been developed. The first, the micromagnetic approach, aims to determine the external conditions of field and temperature required to produce a magnetization reversal for a given mechanism. In this model, the energy barrier is assumed to be proportional to the magnetocrystalline anisotropy energy and nucleation is considered to occur at the first local departure from saturation. Analysis in the micromagnetic approach is based on the Kronmüller equation[2]

$$H_c = \alpha_\psi \frac{2K_1}{\mu_0 M_s} - N_{eff} M_s \qquad (1.19)$$

where α_ψ and the effective demagnetization factor N_{eff} are related to the degree of grain orientation in a real magnet (which is an assembly of grains that are not fully aligned).

The second approach is a phenomenological "global" approach. In the global approach, the critical phenomenon for magnetization reversal is considered to be the formation of a magnetic heterogeneity, typically a domain wall. The energy involved is that of a domain wall in the region, and the size of the smallest possible reversed nucleus must be related to the characteristic domain wall width in that region.

Both models have the weakness that characteristics of the defects are unknown, and so energy defined inside the hard magnetic phase is used as the energy reference. The micromagnetic approach differentiates between the reversal mechanisms, but the global approach cannot. However, thermal

[†] The term "pinning sites" can be misleading because these are not point defects, but rather long range linear or planar defects.

activation effects are included in the gloabal approach, but neglected in the micromagnetic approach[13]. Here we adopt the global approach. A more detailed description of both approaches can be found in Givord and Rossignol's chapter in *Rare Earth Iron Permanent Magnets*[13].

For a flat distribution of energy barriers at a fixed external field, the magnetization decays as

$$M(t) = A + S \ln t \tag{1.20}$$

where A is a constant related to the initial conditions. The magnetic viscosity coefficient S is related to the irreversible susceptibility $\chi_{irr,}$ by $S_v = S/\chi_{irr}$, where both S and χ_{irr} have been corrected for demagnetization effects. The parameter S_v is dependent both on field and magnetization and can be related to the energy barriers of reversal within the material by

$$S_v = \frac{-k_B T}{\partial E / \partial H \mid_{M_{irr}}} \tag{1.21}$$

where T is the absolute temperature, and (∂E/∂H) is the rate of change of the energy barrier with field. This relation is the basis for interest in magnetic viscosity measurements because it enables the measurements to be used as a probe of the rate of change of the energy barrier with field, which is directly determined by the reversal mechanism[16]. Unfortunately, the actual reversal mechanism usually cannot be determined directly from measurement of S_v[17].

The volume V_a of material involved in magnetization reversal is

$$V_a = \frac{k_B T}{S_v \mu_0 M_s} \ . \tag{1.22}$$

This parameter is termed the activation volume. It is an important parameter in coercive processes, but numerous simplifications were made in the derivation of V_a, so the value obtained experimentally should only be used as an evaluation[15].

Two experimental methods are commonly used for measurement of χ_{irr} for use in the above calculations. In the first method, called the χ_{rev} method, a small minor loop on the order of 0.01 T is measured at the end of a magnetic viscosity experiment. The mean slope of this minor loop is identified with the reversible susceptibility χ_{rev} and χ_{irr} is determined as the difference χ_{tot}-χ_{rev},

where $\chi_{tot}=\partial M/\partial H$ from the hysteresis loop. In the second method, known as the DCD method, the full recoil loop is measured, i.e. to $H_{int} = 0$. Now

$$\chi_{rev} = \left(\frac{dM_{rev}}{dH_{\text{int}}} \right)_{Mirr} . \tag{1.23}$$

Recoil curves are curves of constant M_{irr} in (M, H_{int}) space, so χ_{rev} is the slope of the recoil curve. χ_{irr} is again the difference χ_{tot}-χ_{rev}. Neither method is strictly correct, but Crew and coworkers have shown that the DCD method, when properly corrected, gives a more similar value to the 'true value' of S_v for a given material[16].

Experimentally, the DCD method involves measuring recoil curves to zero internal field from a number of starting fields that begin on the major hysteresis loop of the sample. The irreversible magnetization M_{irr} for a material with magnetization M at a field H is the value of the magnetization measured when the field H is reduced to zero. The reversible magnetization M_{rev} of the materials in the state (M,H) is equal to M-M_{irr}. Figure 1.7 illustrates these definitions.

Analysis of the data from recoil curves is based upon the constitutive equation

$$dM_{rev} = \chi_{rev} dH_{\text{int}} + \eta dM_{irr} \tag{1.24}$$

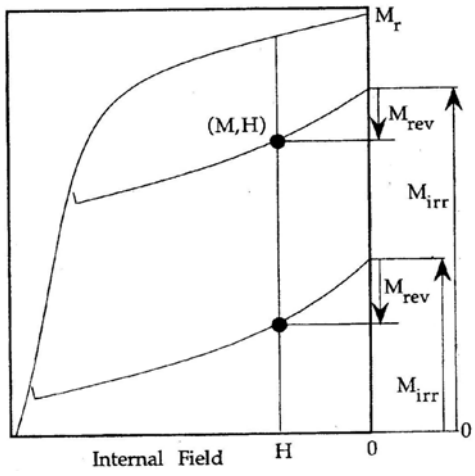

Figure 1.7. An illustration of the DCD definition of Mirr and how the curves of M_{rev} vs M_{irr} are built up from points on individual recoil curves. Here 'H' means internal field, refered to as 'H_{int}' in the text (After D.C. Crew, R.C. Woodward, and R. Street, 1999)

where $H_{int} = H - DM$ is the internal magnetic field (D is the demagnetizing factor), χ_{rev} is the reversible susceptibility defined in Equation 1.22 and η is a parameter defined by

$$\eta = \left(\frac{dM_{rev}}{dM_{irr}} \right)_{H_{int}} . \qquad (1.25)$$

The parameter η is calculated by building up curves of M_{rev} vs M_{irr} at constant internal field. η is the slope of these curves[18]. Experimentally, η is calculated at the rightmost end of the M_{rev} vs M_{irr} curves, i.e., closest to the major hysteresis loop. Now $\chi_{irr} = \chi_{tot} - \chi_{rev}$, where $\chi_{tot} = \partial M / \partial H$ from the major hysteresis loop. When reversible magnetization is a large proportion of the total magnetization (e.g. in isotropic systems) it is necessary to make a correction to S_v determined using the value of χ_{irr} calculated from the DCD method. This correction is

$$S_v^{\eta} = \frac{S_v}{1+\eta} \qquad (1.26)$$

Another method to calculate the activation volume was developed by Givord *et al*[19]. In this method, results from the magnetic viscosity measurements are used to construct hysteresis loops in the second quadrant for different waiting times, as shown in Figure 1.8. Two loops for different waiting times t_i and t_j are selected. The difference in the coercivities of the two loops can be used to calculate S_v using the equation

$$\Delta H_{ij} = S_v \ln(t_i / t_j) . \qquad (1.27)$$

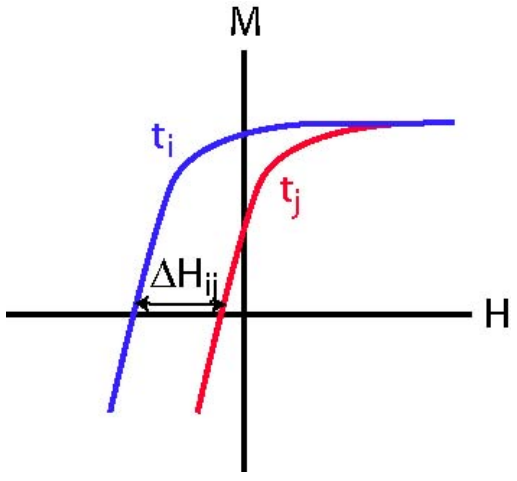

Figure 1.8. Givord method of constructing hysteresis loops for different waiting times t_i and t_j from magnetic viscosity measurement.

1.4 THE SM-CO SYSTEM

Magnets based on alloys of Sm with Co are often referred to as "Sm-Co", or "1-5" and "2-17" for their main subcategories. These designations are quite simple, and hide the complex nature of these magnets. While the materials are indeed based on the intermetallic compounds $SmCo_5$ or Sm_2Co_{17}, the real magnets are actually multi-phase alloys with complex microstructures. They are generally not in an equilibrium state and practical magnets always contain more than two elements[9]. Before discussing the microstructures and resulting properties of the real magnets it is important to understand the phase relations, structure, and properties of the basic $SmCo_5$ and Sm_2Co_{17} intermetallics.

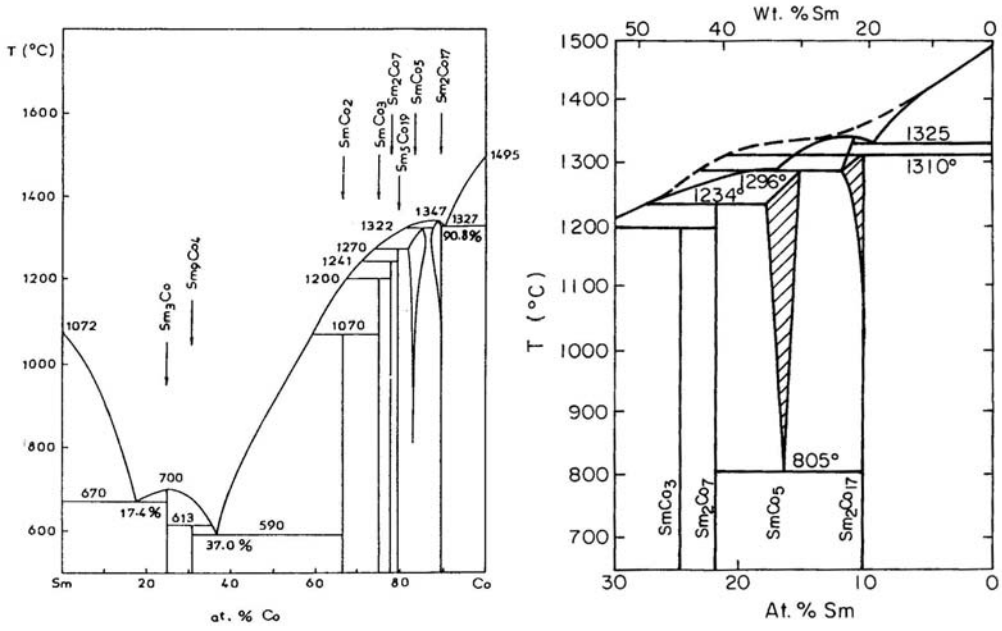

Figure 1.9. The Sm-Co equilibrium phase diagram. (a) shows the full diagram (after Ge *et al* 1993) while (b) shows detail of the Co-rich portion (after R.C. O'Handley 2000)

1.4.1 Phase Relations

The binary Sm-Co equilibrium phase diagram is shown in Figure 1.9[20]. While there are many binary Sm-Co phases, few of them show any solid solubility. The exceptions to this are $SmCo_5$, and Sm_2Co_{17} which show homogeneity regions at high temperatures. The presence of these regions is

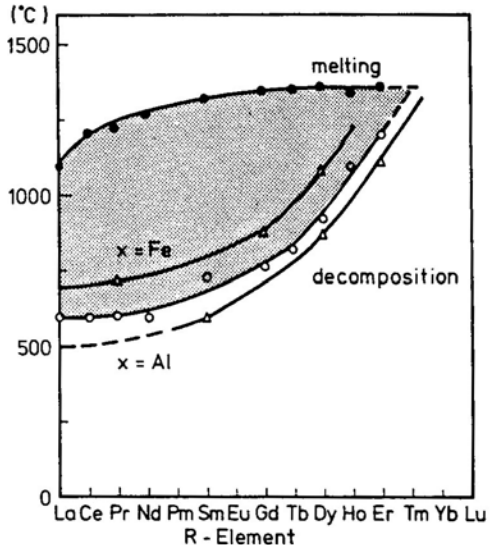

Figure 1.10. Stability ranges for RCo_5 phases showing solidus temperature and eutectoid decomposition temperature and illustrating the effect of small third element substitution, x= 3% Fe or Al. (after K.J. Strnat 1988)

probably related to the possibility of their crystal structures to replace Sm atoms by a dumbbell of Co atoms and vice versa[10].

Another important feature of the Sm-Co phase diagram is the eutectoid decomposition of $SmCo_5$ below 805°C into Sm_2Co_7 and Sm_2Co_{17}. This means that $SmCo_5$ is metastable at room temperature. However, in practice long-range diffusion in $SmCo_5$ is negligible below approximately 700°C and the decomposition can be suppressed by moderate cooling to room temperature. It is also possible to shift the decomposition temperature to a more useful range by substituting other elements for Co, as shown in Figure 1.10. Because of the metastability of $SmCo_5$, its use is limited to temperatures below which kinetics prevent transformation to the stable Sm_2Co_7 and Sm_2Co_{17} phases[4].

1.4.1.1 $SmCo_5$

The structure of $SmCo_5$, shown in Figure 1.11, is rather simple. The structure is of the $CaCu_5$ type, with hexagonal space group *P6/mmm*, and consists of[2] alternating planes consisting of Co and Sm in 2*c* sites and 1*a* sites respectively at z=0 and planes of Co in 3*g* sites at z=1/2. The lattice parameters[12] are a = 0.4995 nm and c = 0.3978 nm, giving c/a = 0.7964. The Curie temperature of pure $SmCo_5$ is 1020 K. Of all the phases from 1-3 to 2-

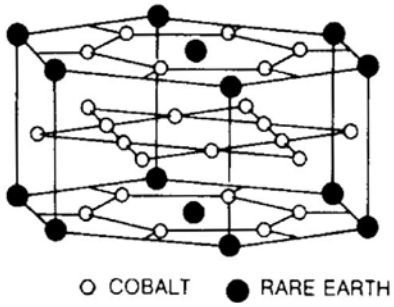

Figure 1.11. $CaCu_5$ type crystal structure of $SmCo_5$ (after K.J. Strnat 1988)

17 stoichiometry, the 1-5 phase is unique because it does not have a rhombohedral form[9].

1.4.1.2 Sm_2Co_{17}

Figure 1.12 illustrates the two different structures that Sm_2Co_{17} can have: the rhombohedral $R\bar{3}m$ structure of Th_2Zn_{17} type, and the hexagonal $P6_3/mmc$ structure of Th_2Ni_{17} type. The structures of Sm_2Co_{17} are derived from that of $SmCo_5$ by replacing one third of the Sm by pairs of cobalt atoms known as "dumbbells". In the rhombohedral form, the planes containing the dumbbells have stacking sequence ABCABC… while in the hexagonal form the sequence is ABAB…[2]. Lattice parameters of the rhombohedral form are a = 0.8402 nm and c = 1.2172 nm, while lattice parameters of the hexagonal

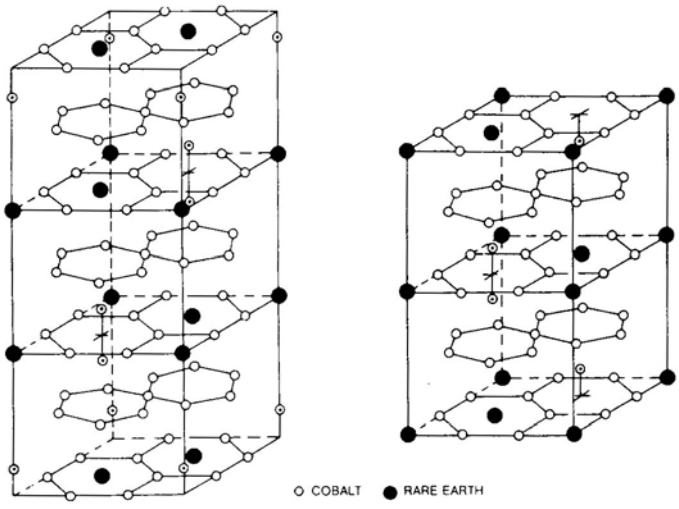

Figure 1.12. Crystal structure of Sm_2Co_{17} compounds: Rhombohedral Th_2Zn_{17} (left) and hexagonal Th_2Ni_{17} (right). (After K.J. Strnat 1988)

form are a = 0.8373 nm and c = 0.8165 nm.

Sm_2Co_{17} usually crystallizes in the rhombohedral form, as at equilibrium the hexagonal form is only stable above 1300°C [21]. This phase has a higher magnetization and Curie temperature (T_c = 1190 K) than $SmCo_5$ because of the lesser amount of rare earth in the structure. Recently, researchers using nonequilibrium synthesis techniques have also been able to make Sm-Co alloys with a $TbCu_7$ type structure, with space group *P6/mmm*[22]. This can be understood as being an intermediate structure between 1-5 and 2-17, where fewer than one third of the Sm are replaced by Co dumbbells. Table 1.1 summarizes intrinsic properties of $SmCo_5$ and Sm_2Co_{17}.

Table 1.1. Intrinsic properties of Sm-Co compounds

	a (nm)	c (nm)	T_c (K)	$\mu_0 M_s$ (T)	K_1 (MJ/m^3)	$\mu_0 H_A$(T)
$SmCo_5$	0.4995	0.3978	1020	1.07	17.2	35
Sm_2Co_{17}(R)	0.8402	1.2172	1190	1.22	3.3	6.5

1.4.2 Magnetic Structure and Anisotropy

$SmCo_5$ and Sm_2Co_{17} exhibit easy axis anisotropy with the c axis as the easy axis. Figure 1.13 illustrates magnetization curves measured parallel and perpendicular to the easy axis of $SmCo_5$ and Sm_2Co_{17}. The slope of the magnetization curve perpendicular to c is $\mu_0 M_s^2/2K_1$, so that the anisotropy field $H_A = 2K_1/\mu_0 M_s$; $\mu_0 H_A$ is about 35 T for $SmCo_5$.

The magnetic structure of rare earth (RE) transition metal (TM) compounds is usually described as consisting of two ferromagnetic sublattices comprising the RE and TM atoms, respectively. (Atoms of the same species in non-equivalent sites may, however, have different moments.) As a first approximation, the RE and TM species interact separately with the crystal lattice, the total magnetic anisotropy of the compound being the sum of the individual sublattice anisotropies[9]. The intersublattice coupling constant J_{CoR} is negative, so the RE and Co sublattices couple parallel for light rare earth elements (LRE) and antiparallel for heavy rare earth (HRE) elements[10]. The net moments of these two sublattices therefore add for the LRE compounds,

while they subtract for the HRE. As a result, the room temperature magnetization for the former group of R-Co is higher than for the latter group, to the extent that only compounds with LRE, such as Sm, qualify for permanent magnet purposes[10].

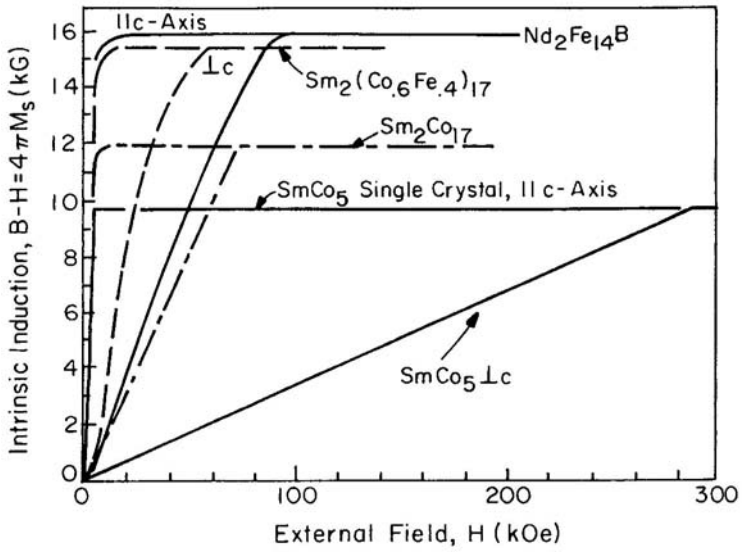

Figure 1.13. Hard and easy axis magnetization curves for $SmCo_5$ and Sm_2Co_{17} (after R.C. O'Handley 2000)

The anisotropy of the RE sublattice is considered to be due to the influence on the localized R^{3+} ion of the electronic field of its local atomic environment ("crystal field") and to that of the molecular field (R-Co exchange interaction). A single-ion anisotropy model is satisfactory for the mathematical description. The nature of the TM anisotropy, particularly that of the Co sublattice in RCo_5, is less clear, with the 3d-electrons having been treated either as localized or itinerant by theoreticians. However, it seems that in RCo_5, the Co-sublattice anisotropy can also be fairly well described by a single-ion model with a large orbital component of the Co-ion moment being responsible for the easy axis anisotropy[9].

The permanent magnet properties of $SmCo_5$ are ultimately attributable to its exceptionally high magnetocrystalline anisotropy energy; the uniaxial structure together with the orbital angular moment of the RE species is the main source of magnetocrystalline anisotropy in the RCo_5 system[4]. The average zero-temperature cobalt moment is reduced by the presence of the rare

earth from the pure Co value of 1.7 μ_B to 1.5 μ_B in $SmCo_5$. The cobalt moments on the two sites differ slightly and measurements of the nuclear quadrupole interaction by ^{59}Co nuclear magnetic resonance indicate that the larger orbital moment (about 0.3 μ_B) resides on 2c sites, where it makes a substantial contribution to the uniaxial anisotropy[2].

The 3d sublattice anisotropy in R_2Co_{17} compounds leads to an easy plane magnetization ($K_1 < 0$) and consequently easy axis behavior is rather the exception, shown only by the compounds of Sm, Er, and Tm. The unfavorable easy plane type of anisotropy has generally been attributed to the dumbbell pairs of Co atoms in the R_2Co_{17} structure, which destroy the easy-axis character[10]. However, moderate substitutions of certain third elements, especially iron, for most of the Co can induce easy axis anisotropy in most other R_2Co_{17} (except R = Nd or Dy)[9].

The rare earth sublattice anisotropy in R_2Co_{17} is substantially lower than in RCo_5 due to a reduced crystal-field interaction at the 6c sites[2]. Unlike $SmCo_5$, it is difficult to develop adequate coercivity for a permanent magnet in pure Sm_2Co_{17} because the magnetocrystalline anisotropies of R_2Co_{17} phases (3-4 x 10^6 J/m^3) are generally less than those of the corresponding 1-5 phases (11-20 x 10^6 J/m^3)[4]. However, the 2-17 saturation magnetizations and Curie temperatures are generally greater because of the lesser amount of rare earth in the structure[2].

At high temperatures, approaching the Curie points of the RCo_5 or R_2Co_{17}, the RE moments are largely disordered and the strongly ordered TM sublattice determines the overall anisotropy behavior. For this reason all RCo_5 have easy axis anisotropy at high temperatures. At low temperatures approaching 0 K, the anisotropy of the RE sublattice makes itself strongly felt. Different rare earths favor either *c*-axis alignment (as with Sm in $SmCo_5$), or basal-plane orientation of their moments. In the first case, the uniaxial Co anisotropy is strengthened[9].

1.5 PRACTICAL SM-CO MAGNETS

1.5.1 Microstructure

The metallurgical microstructure clearly controls the coercivity of Sm-Co magnets. As a result, much effort has been devoted to microstructure and magnetic-domain studies of these magnets. Unfortunately, the structural features responsible for wall pinning or nucleation are so small that they can barely be seen by high resolution transmission electron microscopes. It is still difficult to identify compositions and structures of some of the significant precipitates and grain boundary phases even with today's best instruments. Even so, the typical microstructures associated with different magnets and behavior types are fairly well established.

1.5.1.1 $SmCo_5$-type magnets

The $SmCo_5$ magnets have a nearly single phase, featureless microstructure. The grain size is kept small, ≤ 10 μm, to keep the probability that they contain a nucleating defect low. Parallel alignment of the c-axes of the grains is desirable and can easily be made nearly perfect through special processing techniques[11]. This minimizes the amount of disorder at the grain

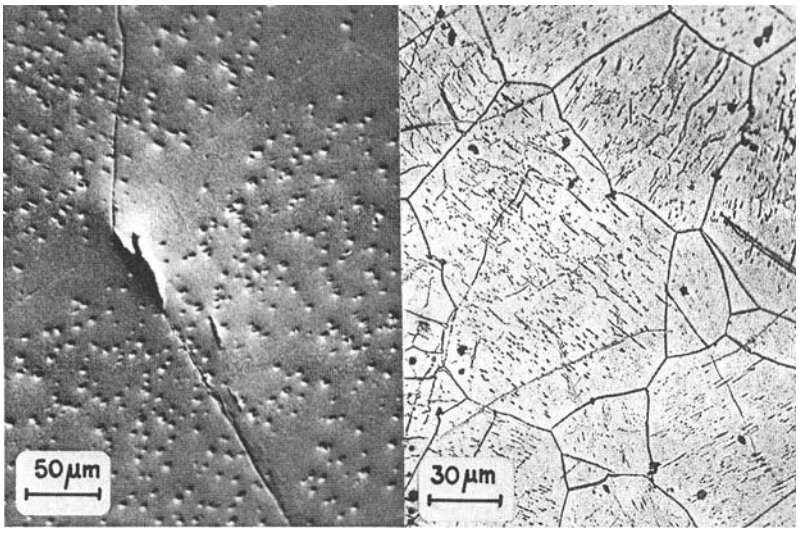

Figure 1.14. Example of precipitation microstructures found in 1-5 type RE-Co magnets bulk hardened with Cu: $Sm_{3.5}Cu_{1.0}Fe_{0.5}$ homogenized at 1100°C/3h and quenched. Left: SEM image after aging at 575°C/4h. Right: Light micrograph after additional aging at 525°C/4h (after K.J. Strnat 1988).

boundary, and along with the lack of oxides and secondary phases in well-prepared magnets, makes the boundaries thin and clean looking. Despite the apparently clean grain boundaries, H_c can still be high, so the boundaries must still block the movement of domains from grain to grain. Otherwise, the magnetization would quickly reverse after the first nucleation event. So, it must be assumed that there are imperfections associated with the grain boundaries that, although not visible under the microscope, are capable of strongly pinning domain walls.

Cu substitution for Co in $SmCo_5$ is known to produce needle-like precipitates (Figure 1.14) that pin domain walls and lead to high coercivity. The precipitates appear to be Co-modified $SmCu_5$ while the matrix is $SmCo_5$ with some dissolved Cu. There was some disagreement as to the origin of this phase separation, and the quasi-binary $SmCo_5$-$SmCu_5$ system has been studied extensively as a result. All studies confirmed that there is complete mutual solid solubility at high temperatures and a wide miscibility gap at room temperature, enabling the precipitation. The coercivity is due to the precipitates which have magnetic properties that are different from the matrix phase.

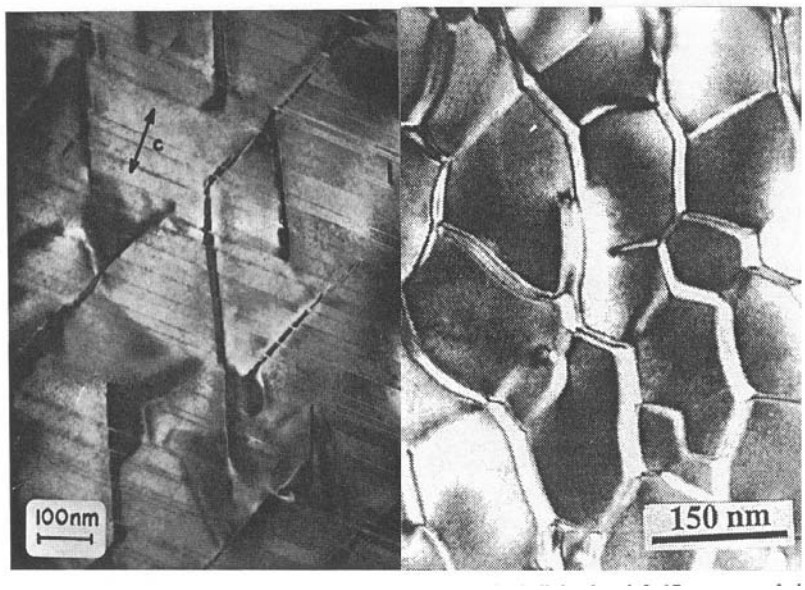

Figure 1.15. Example of precipitation microstructures found in bulk-hardenend high H_c 2-17 magnets. Left: section contains the c-axis (after Strnat 1988); note the rhomboid cells of the twinned 2-17R matrix, the 1-5 boundary phase surrounding the cells, and the thin bands of "Z-phase" in the basal plane crossing many cells and walls. Right: basal plane section (after G.C. Hadjipanayis 1999)

1.5.1.2 Sm_2Co_{17}-type magnets

The microstructure of magnets based on Sm_2Co_{17} as the principal phase is more complicated than that of 1-5 type magnets. The main feature of the microstructure, shown in Figure 1.15, is a well-developed network of small cells of a matrix phase surrounded by a thin boundary phase of 1-5 stoichiometry and $CaCu_5$ structure. The cells have a roughly rhombic shape, elongated along *c*, while they have an irregular cross-section in the basal plane. The cell interior has the rhombohedral Th_2Zn_{17} structure and is heavily twinned, with the twin boundaries in the basal plane. In low H_c 2-17 magnets, cells have dimension of ~50 nm, while the walls are ~4-10 nm in width, while the high H_c versions have cells ~100 nm in size[23]. The high H_c magnets have the added feature of thin lamellae, ~3.0 nm, superimposed on the cellular microstructure. These lamellae, also called the "platelet phase" or "Z-phase" are normal to the [0001] axis, and run across many cells and cell boundaries. It has been suggested that the lamellae have a RCo_3 structure, but it is now generally accepted that they have the hexagonal Th_2Ni_{17} structure[12,23]. In good magnets, all three phases are crystallographically coherent. Figure 1.16 shows a schematic of the microstructure, indicating locations of the various phases.

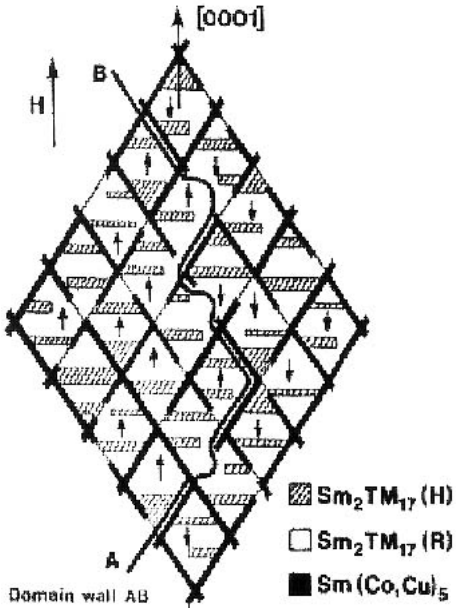

Figure 1.16. Detailed microstructure of the rhombic cells shown in Figure 8. AB represents a domain wall pinned by the boundary phase (after R.A. McCurrie 1994)

The hard magnetic properties of the high H_c, precipitation-hardened $Sm_2(Co, Fe, Cu, M)_{17}$-type magnets can be achieved only through series of complex heat treatments[23]. The samples are first solutionized at ~1200°C and then quenched to room temperature. Then they are heat treated in the temperature range 800-850°C. It is during this heat treatment that the cellular structure and lamellae develop, but there is not significant coercivity after the treatment. Development of coercivity requires yet another heat treatment at around 400°C, or slow cooling from the 800°C heat treatment to 400°C is used. The microstructure doesn't show any visible differences after this heat treatment, but the magnetic properties are significantly improved. Recent energy-dispersive x-ray analysis suggests a diffusion of the various additive elements during the treatment, with an increase of Cu content in the cell boundaries[23]. Such an increase causes a dilution of the magnetic properties of the 1-5 phase, which leads to a greater difference between the properties of the cells and the boundary, and more domain wall pinning at the boundary. It is believed that the Z-phase provides diffusion paths for the Cu to get to the grain boundaries during the final heat treatment[12].

Lorentz microscopy shows domains in Sm_2Co_{17}-type magnets with wavy walls (Figure 1.17). The walls run parallel to the *c*-axis, but they follow the zigzag path of the 1-5 cell boundary phase. The domains appear to be smaller in the higher H_c materials, and do not seem to be affected by the

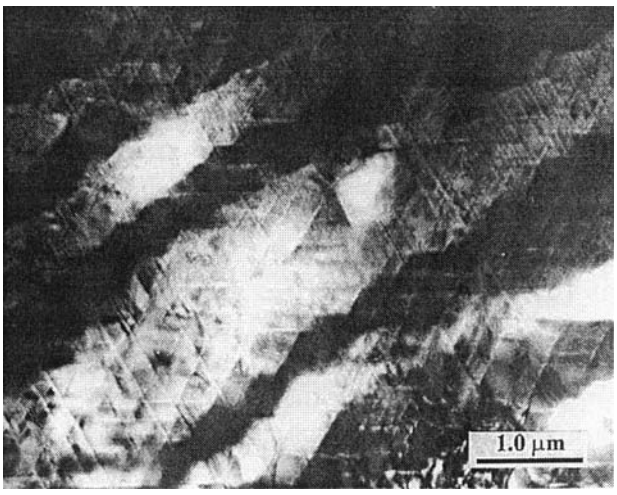

Figure 1.17. Magnetic domains in 2-17 magnets. The walls run parallel to the c-axis, but follow the path of the 1-5 cell boundary phase (after G.C. Hadjipanayis 1999)

presence of lamellae[23]. The wavy nature of the walls does not change after the application of a magnetic field, confirming that they are indeed pinned by the cell boundaries, as illustrated in Figure 1.18. The most probable interpretation is that the domain wall has a lower energy in the 1-5 phase than in the 2-17 cell interior; this implies an attraction by the cell boundary[9].

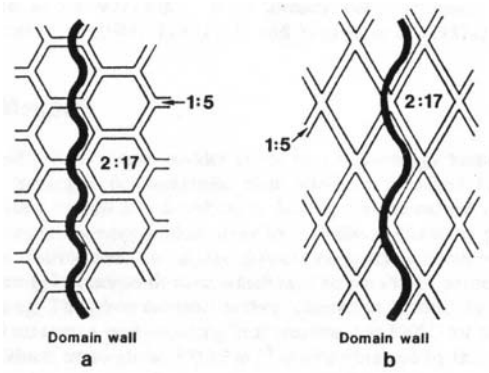

Figure 1.18. Domain walls pinned by a $Sm(Co, Cu)_5$ phase: (a) in a plane perpendicular to the easy [0001] axis; (b) in a plane parallel to the easy axis (after R.A. McCurrie 1994).

1.5.2 Effect of Alloying

Sm-Co based permanent magnets never contain just samarium and cobalt. Not only is it difficult to keep the compound pure during industrial processing, but it is also known that the addition of certain elements can have a positive effect on the magnetic properties of the material. As a result, several transition metals, including Cu, Fe, and Zr are substituted for Co in commercial magnets and the effects of rare earth substitution for the Sm has also been investigated.

1.5.2.1 Copper substitution

Copper substitution for Co in 1-5 magnets was one of the first substitutions investigated and has lead to the development of 2-17 type magnets. As mentioned above, in $SmCo_5$-type magnets, Cu causes precipitates that pin walls and lead to high H_c. It has the added benefit in 1-5

magnets of allowing co-substitution of Fe for Co, lowering the eutectoid decomposition temperature and therefore stabilizing the 1-5 phase, and it broadens the homogeneity range to higher transition metal contents[9]. The one major drawback is that Cu addition reduces B_r.

In Sm(Co, Fe, Cu, Zr)$_Z$ 2-17-type alloys, the Cu goes to the 1-5 cell boundary phase, causing a large difference in the magnetic properties of the boundary and cell phases, increasing domain wall pinning, and hence H_c. Too high a Cu content can cause the Sm_2Co_{17} phase to destabilize, because the Sm_2Cu_{17} phase does not exist[9]. Without Cu, the favorable cellular microstructure will not form. When the ideal Cu content is combined with a low Z value a finer microstructure and a very good temperature dependence of coercivity can be achieved[23]; this is important for high temperature applications. In fact, magnets with the cellular microstructure and carefully controlled Cu content can actually exhibit a positive temperature dependence of coercivity[24]. This abnormal behavior is attributed to a decrease in the anisotropy constant K_1 of the Sm(Co, Cu)$_5$ with Cu content[25].

1.5.2.2 Iron Substitution

Iron is added to Sm_2Co_{17} and Sm(Co, Cu)$_5$-type magnets mainly because it increases B_s. It is not possible to add Fe to $SmCo_5$ magnets without Cu, because there is no $SmFe_5$ phase. In 2-17 type magnets, Fe stabilizes the c-axis anisotropy of the matrix phase. However, too much Fe can destabilize the 2-17 phase on cooling through T_c, because of strong negative exchange interactions due to small Fe-Fe spacing at the dumbbell sites[23]. This leads to the formation of undesirable soft Fe-Co phases.

1.5.2.3 Zirconium substitution

Substitution of Zr (or Hf, Ti) allows for greater substitution of Fe in the rhombohedral 2-17 phase. In addition, it increases the magnetocrystalline anisotropy and assists in the formation of the lamella phase in Sm_2Co_{17}-type magnets. The increase in the lamella phase enables Cu to diffuse to the cell boundaries, increasing wall pinning and correspondingly, H_c. As such, high concentrations of Zr can be found in the lamella phase.

1.5.2.4 Rare earth substitution

Unlike the compounds of light-rare earths and Co, compounds with the heavy rare earths are ferrimagnetic. Because of the weak exchange between the rare earth and the cobalt, the two sublattices have very different temperature dependences[2]. The magnetization of the rare earth falls off much more quickly than that of the Co, due to the weak RKKY interaction in the former. If the magnetization of the RE sublattice is greater than that of the Co sublattice, then the M-T curve will have a compensation point, as in the curve labeled "$GdCo_5$" in Figure 1.19[9]; above the compensation point, the magnetization actually rises with increasing temperature before decreasing again. This has the important consequence that substituting the right amount of a HRE, such as Gd, for Sm, can cause M_S to be nearly temperature independent in the desired operating range.

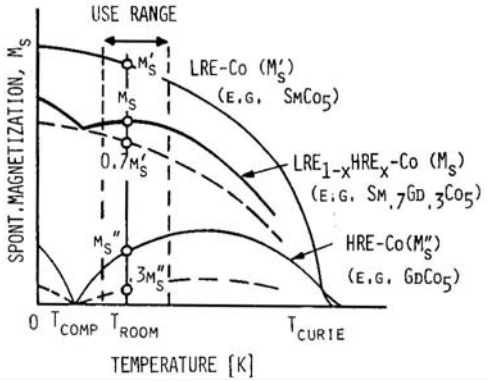

Figure 1.19. Temperature variation of the spontaneous magnetization in LRE-TM and HRE-TM alloys (qualitative), and principle of internal temperature compensation in rare earth permanent magnets (after K.J. Strnat 1988)

1.6 NANOCRYSTALLINE MAGNETS

The recent trend in both soft and hard magnet development has been the development of materials with grain size on the order of nanometers. This trend started with the development of FINEMET in 1988. FINEMET is produced by melt spinning $Fe_{73.5}CuNb_3Si_{13.5}B_9$ and then annealing the resultant amorphous alloy to recrystallize a bcc Fe structure with grain size

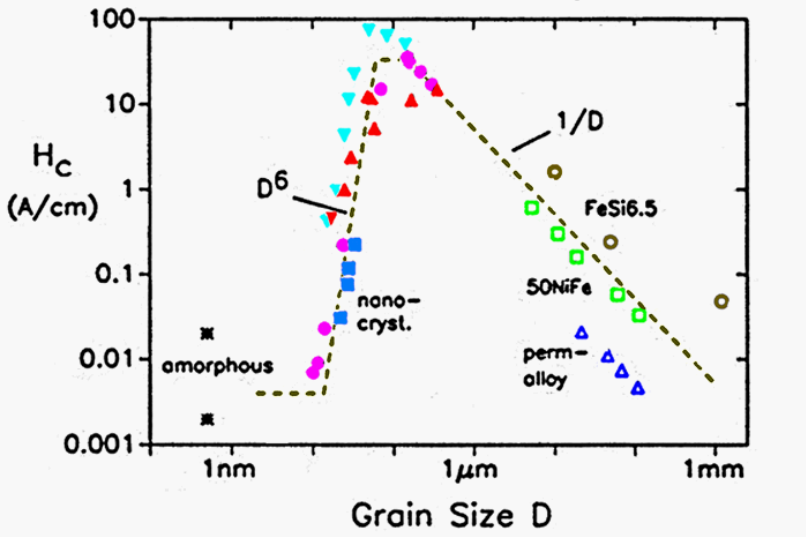

Figure 1.20. Coercivity H_c versus grain size for various soft magnetic metallic alloys. The data of the nanocrystalline material refer to (▲) FeNbSiB, (●) FeCuNbSiB, (◆) FeCuVSiB, (■) FeZrB, and (▼) FeCoZr (after G. Herzer 1992).

approximately 10 nm. FINEMET exhibits excellent soft magnetic properties, i.e. an extremely low coercivity, but the reason for this was not initially understood. Herzer[26], upon studying the temperature dependence of M_s for the alloy, found that it actually had 2 magnetic phases: α-Fe(Si) grains; and a grain boundary phase 4-5 atomic layers thick. He then made FINEMET alloys of grain size 10 nm to 150 nm, and Fe-Si 6.5 wt%, 50 Ni-Fe, and Permalloy alloys with grain size 1 μm to 1 mm. Herzer's results are summarized in Figure 1.20[27]. He found the coercivity, H_c followed a D^6 dependence for grain size D < 40 nm, while it followed a 1/D dependence for D > 150 nm.

Herzer explains the small grain size behavior in terms of the random

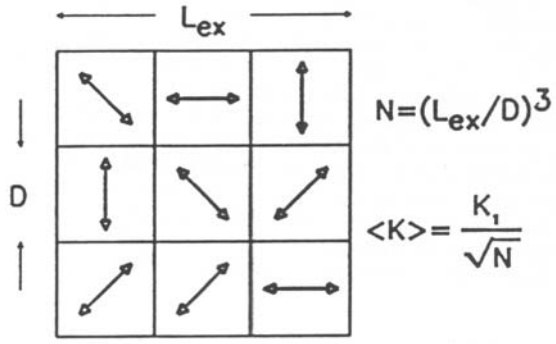

Figure 1.21. Schematic representation of the random anisotropy model. The arrows indicate the randomly fluctuating magnetocrystalline anisotropies (after G. Herzer 1990).

anisotropy model, originally developed for amorphous ferromagnets. The basic idea of the random anisotropy model, sketched in Figure 1.21, starts from an assembly of ferromagnetically coupled grains of size D, with magnetocrystalline anisotropy directions oriented randomly.

It is assumed the $D << L_{ex}$, the ferromagnetic exchange length defined as $L_{ex} = (A/K_1)^{1/2}$, where A is the exchange stiffness[‡]. The exchange length thus defined is simply proportional to the domain wall width (Equation 1.17). In the volume $V = L_{ex}^3$, the effective anisotropy will result from averaging over the N grains within the volume. For a finite number of grains there will always be some easiest direction determined by the statistical fluctuations. As a result, the anisotropy density, <K>, is determined by the mean fluctuation amplitude of the anisotropy energy of the N grains

$$\langle K \rangle \approx \frac{K_1}{\sqrt{N}} = K_1 \left(\frac{D}{L_{ex}} \right)^{3/2} . \qquad (1.28)$$

The exchange length is now related self-consistently to the average anisotropy by substituting <K> for K_1 in the definition of L_{ex}, yielding $L_{ex} = (A/\langle K \rangle)^{1/2}$. This renormalization of L_{ex} is a result of the counterplay of anisotropy and exchange energy: as the magnetocrystalline anisotropy is suppressed by the exchange interaction, the scale on which the exchange interactions dominate expands, and so the local anisotropies are averaged out more effectively.

Substituting the renormalized definition of L_{ex} into equation 1.28 yields

$$\langle K \rangle \approx \frac{K_1^4}{A^3} D^6 \qquad (1.29)$$

Now, if the coercivity is related to <K> using Stoner's results for coherent spin rotation,

$$H_c \propto \frac{\langle K \rangle}{\mu_0 M_s} \approx \frac{K_1^4 \cdot D^6}{\mu_0 M_s \cdot A^3} \qquad (1.30)$$

[‡] It should be noted that there are conflicting definitions of L_{ex} in the magnetism community. L_{ex} is also defined as $(A/\mu_o M_s^2)^{1/2}$, see for example R. Skomski and J.M.D. Coey 1999.

and the D^6 grain size dependence of <K> when $D << L_{ex}$ should be reflected in the soft magnetic properties. Herzer also points out that these results are not limited to the case of coherent magnetization rotation, but can also be derived assuming domain wall pinning where

$$H_c \approx \frac{\sqrt{A \cdot K}}{\mu_0 M_s \cdot L} \tag{1.31}$$

where L denotes the typical wavelength of the effective anisotropy fluctuations, which is given by the exchange length in this case. Substituting the renormalized L_{ex} and equation 1.28 into equation 1.31 again yields equation 1.30.

For $D = L_{ex}$, the coercivity approaches its maximum value, $H_c \propto K_1/\mu_0 M_s$. If the grain size exceeds the exchange length ($D > L_{ex}$), the effective anisotropy <K> is given by K_1. If the grain size exceeds the domain wall width, $\delta_w = \pi L_{ex} = \pi(A/K_1)^{1/2}$, the magnetization process is determined by domain wall pinning at the grain boundaries, and

$$H_c \propto \frac{\sqrt{A \cdot K_1}}{\mu_0 M_s \cdot D}. \tag{1.32}$$

In the case of FINEMET, Herzer found L_{ex} = 35 nm and δ_w=110 nm, which is in good agreement with the data. Commercially produced FINEMET usually has grain size D = 10 nm which is less than L_{ex}, and so has very good soft magnetic properties. In the case of permanent magnets, we would like to be at the plateau region around L_{ex} and δ_w, in order to achieve the maximum coercivity. For $SmCo_5$, L_{ex} = 1.1 nm and δ_w = 3.6 nm, and so a grain size on the order of a few nanometers would achieve optimum coercivity.

1.7 MECHANICAL ALLOYING

High energy ball milling has recently been explored as a method to synthesize magnetic materials. This method is useful because it not only produces fine particles, but also can be used to synthesize metastable phases in a similar manner to rapid solidification. Also, amorphous milled powders can be annealed to crystallize a very fine nanocrystalline microstructure. Mechanical alloying is not seen as a commercially viable process because the

yields are very low, but it may be a better method for Sm-based alloys than rapid solidification because it avoids the problem of Sm evaporation from the melt used as a precursor to melt spinning.

A conventional ball mill, used for mixing powders or reducing particle sizes, consists of a rotating horizontal drum half-filled with small steel balls. As the drum rotates, the balls drop on the powder that is being ground. The rate of grinding increases with the speed of motion. At a critical high rotation speed, however, the centrifugal force acting on the steel balls exceeds the force of gravity, and the balls are pinned to the wall of the drum. At this point the grinding action stops. If the mill is of large enough diameter (on the order of meters) and is operated just short of the critical rotation speed, the tumbler mill can be considered to be a high energy ball mill.

Obviously, such large mills are inappropriate for laboratory use, so a number of different types of small mills have been developed to obtain high energies without the balls being pinned to the wall. Two of these laboratory scale mills are the Fritsch P5 "planetary ball mill" and Spex 8000 "mixer mill". The planetary ball mill consists of a sun disk, rotating at an angular velocity Ω, on which milling containers are rotating at an angular velocity ω, in the direction opposite to that of the sun disk. The balls actually spend much of the time stuck to the container wall, so long milling times (on the order of days) are required for alloy formation. The milling time can be reduced by using a Spex mill. The Spex mill, used in this study, operates by shaking the container in a figure eight motion, which increases the energy and avoids the problem of balls sticking to the wall, thereby decreasing the time required for alloy formation.

In high energy mills, particles of the metal powder are repeatedly flattened, fractured, and rewelded. The powder particles are trapped between colliding steel balls and the balls colliding with the walls of the container. The force of the impact deforms the particles and creates new atomically clean surfaces. When two clean surfaces come into contact, they weld together. At early stages in the process, the particles are still relatively soft and tend to weld together into larger particles. As the process continues, the particles harden, and fracture more easily as a result. Eventually, the tendency to weld

and the tendency to fracture come into balance, and the particles' size becomes constant within a narrow range. The rate of refinement of the internal structure of the particles is approximately logarithmic with processing time, so starting from coarse powders does not greatly extend the processing time. After long milling times, the rate of refinement of the internal structure decreases as a result of accumulation of strain energy in the particles, causing them to become extremely hard. At this point, in a mechanical alloying experiment, where elemental powders are used as the precursor material, the metals have formed a true solid solution. Pre-alloys may also be used instead of the mixtures of elemental powders. This process is referred to as "mechanical milling". Generally, the result of mechanical milling is the same as mechanical alloying for an equivalent powder mixture, possibly with some microstructural differences.

Because of the high energies involved, mechanical alloying can be used to synthesize metastable and/or amorphous phases in the same way that rapid solidification is used. However, the precursor phases in the case of mechanical alloying are crystalline solids, rather than liquid, so the thermodynamics and kinetics can be very different. In general, milling produces metastable and amorphous phases by introducing defects into an equilibrium intermetallic compound. These defects raise the free energy of the crystalline compound to the point where the amorphous state is energetically favored. The defect energy stored during severe cold working of metals and alloys is typically 1-2 kJ/mol. These energies are comparable to the energy differences between the crystalline and amorphous states in many alloy systems. It is therefore assumed that this cold working is the driving force for amorphization in high energy mechanical alloying and mechanical milling.

---

[1] Chih-Wen Chen, Magnetism and Metallurgy of Soft Magnetic Materials (New York: Dover Publications, Inc., 1986).
[2] R. Skomski and J.M.D. Coey, *Permanent Magnetism* (Bristol: Institute of Physics Publishing, 1999).
[3] Sóshin Chikazumi, *Physics of Ferromagnetism*, 2nd ed. (Oxford: Clarendon Press, 1997).
[4] R.C. O'Handley, *Modern Magnetic Materials: Principles and Applications* (New York: John Wiley & Sons, Inc., 2000).

[5] R.T. Fingers, J.C. Howarth, M. Huang, and Z. Turgut, "Applications of Rare Earth Magnets in the Military," *Proceedings of the Seventeenth International Workshop on Rare Earth Magnets and Their Applications* (Newark, DE, 2002), 822-830

[6] J.M.D. Coey, ed. *Rare-Earth Iron Permanent Magnets* (Oxford:Clarendon Press, 1996).

[7] W. Rodewald, B. Wall, M. Katter, K. Üstüner, and S. Steinmetz, "Extraordinary Strong Nd-Fe-B Magnets by a Controlled Microstructure," *Proceedings of the Seventeenth International Workshop on Rare Earth Magnets and Their Applications* (Newark, DE, 2002), 25-36

[8] Richard.T. Fingers, and C. Scott Rubertus, "Application of High Temperature Magnetic Materials," *IEEE Transactions on Magnetics* 36, no. 5 (Sept 2000), 3373-3375

[9] K.J. Strnat, "Rare-earth-cobalt permanent magnets," in vol. IV of *Ferromagnetic Materials* (Amsterdam: North-Holland, 1988).

[10] K.H.J. Buschow, *Permanent Magnet Materials*, vol. 3A of *Materials Science and Technology: A Comprehensive Treatment* (Cambridge: Weinheim, 1991).

[11] K.J. Strnat and R.M.W. Strnat, "Rare earth-cobalt permanent magnets," *Journal of Magnetism and Magnetic Materials* 100 (1991), 38-56.

[12] R.A. McCurrie, *Ferromagnetic Materials: Structure and Properties* (London: Harcourt Brace & Company, 1994).

[13] D. Givord and M.F. Rossignol, "Coercivity" in J.M.D. Coey, ed. *Rare-Earth Iron Permanent Magnets* (Oxford:Clarendon Press, 1996).

[14] E.C. Stoner, and E.P. Wohlfarth, *Philosophical Transactions of the Royal Society* 240A, (1948).

[15] D. Givord, Q. Lu, M.F. Rossignol, P.Tenaud, and T. Viadieu, "Experimental Approach to Coercivity Analysis in Hard Magnetic Materials," *Journal of Magnetism and Magnetic Materials* 83 (1990) 183-188.

[16] D.C. Crew, S.H. Farrant, P.G. McCormick, and R. Street, "Measurement of Magnetic Viscosity in a Stoner-Wohlfarth Material," Journal of Magnetism and Magnetic Materials 163 (1996), 299-312

[17] D.C. Crew, P.G. McCormick, and R. Street, "The Interpretation of Magnetic Viscosity," *Journal of Physics D: Applied Physics* 29 (1996), 2313-2319.

[18] D.C. Crew, R.C. Woodward, and R. Street, "Reversible magnetization behavior in $Sm_2(Co, Fe, Cu, Zr)_{17}$, *Journal of Applied Physics* 85, no. 8 (1999), 5675-5677.

[19] D. Givord, M.F. Rossignol, V. Villas-Boas, F. Cebollada, and J.M. González, *Proceedings of the 9th International Symposium on Magnetic Anisotropy and Coercivity in Rare-Earth Transition Metal* Aloys, São Paulo, Brazil, 1996.

[20] W.Q. Ge, C.H. Wu, and Y.C. Chang, "Reinvestigation of the Sm-Co binary system," *Zeitschrift fur Metallkunde* 84 (1993), 165-169.

[21] T.B. Massalski, ed., *Binary Alloy Phase Diagrams* (Metals Park, OH: American Society for Metals).

[22] C.B. Jiang, M. Venkatesan, K. Gallagher, and J.M.D. Coey, "Magnetic and Structural Properties of $SmCo_{7-x}Ti_x$ magnets," *Journal of Magnetism and Magnetic Materials* 236 (2001), 49-55; and M.Q. Huang, W.E. Wallace, M. McHenry, Q. Chen, and B.M. Ma, *Journal of Applied Physics* 83 (1998) 6718.

[23] G.C. Hadjipanayis, "Nanophase Hard Magnets," *Journal of Magnetism and Magnetic Materials* 200 (1999), 373-391.

[24] J.F. Liu, T. Chui, D. Dimitrov and G.C. Hadjipanayis, "Abnormal temperature dependence of coercivity in Sm(Co, Fe, Cu, Zr)z Powder materials," *Applied Physics Letters* 73 (1998), 3007-3009.

[25] W. Tang, Y. Zhang, A.M. Gabay, H. Kronmuller, and G.C. Hadjipanayis, "Effect of Composition and Processing on the Microstructure and Magnetic Properties of $Sm(Co_{bal}Fe_vCu_yZr_x)_z$ magnets," *Proceedings of the Seventeenth International Workshop on Rare Earth Magnets and Their Applications* (Newark, DE, 2002),685-695.

[26] G. Herzer, "Grain Size Dependence of Coercivity and Permeability in Nanocrystalline Ferromagnets," *IEEE Transactions on Magnetics* 26 (1990), 1397-1402.

[27] G. Herzer, "Nanocrystalline Soft Magnetic Materials," *Journal of Magnetism and Magnetic Materials* 112 (1992), 258-262.

2 EXPERIMENTAL PROCEDURES

2.1 MECHANICAL ALLOYING

$Sm_xZr_y(Co_{1-z}Fe_z)_{100-x-y}$ samples were mechanically alloyed from a mixture of $SmCo_5$ ingot and elemental 99.8% pure Co powder, 99.9% pure Fe powder and Zr filings. $SmCo_5$ was used in preference to Sm powder to provide a majority of the Sm content while avoiding the oxidation problems that arise with Sm powder. When it wasn't possible to achieve the desired Sm composition using $SmCo_5$, then 99.9% pure Sm powder was used in addition to the $SmCo_5$ ingot. The $SmCo_5$ was obtained from Less Common Metals, Merseyside, England in ingot form. The ingot's composition, as determined by ICP was 33.3 wt.% Sm, 0.14 wt.% Cu, 0.63 wt.% Fe, 0.058 wt.% C, 0.08 wt.% Sn, <5 ppm B, Co balance. The ingot was broken into pieces and ground into a powder using a mortar and pestle in a glove box. The MBraun Labmaster 130 glovebox used throughout these procedures maintains an Ar atmosphere under a positive pressure. The atmosphere contained less than 3 ppm O_2 and 3 ppm H_2O, as monitored by the built-in H_2O/O_2 analyzer, and most of the time these values were less than 1 ppm. The precursor powders and ingot were stored in the glovebox.

The precursor powder mixture was weighed out in the glovebox and poured into the tool steel milling pot which was sealed with a viton o-ring inside the glovebox. Ten millimeter chrome steel (AISI 52100) balls with mass approximately 4 g each were used inside the milling pot. The pot was loaded with 16 balls and 7 g of powder, giving a charge ratio of 9.3:1. Alloys were milled using the Spex 8000 mixer/mill for12 hours. Milling pots and balls were cleaned with methanol between each use and dried in a drying cabinet at 60°C for at least 30 minutes before they were brought into the glovebox. Balls were changed every 100 hours and o-rings were changed every 50 hours, to prevent sample contamination due to wear. After milling, pots were opened and emptied inside the glovebox. Yields averaged 2.2 g of powder; the remainder could not be recovered from the pot and ball surfaces. Table 2.1 summarizes the compositions prepared. Note that the Sm content for

all compositions is intermediate to that of Sm_2Co_{17} (10.5 at%) and $SmCo_5$ (17 at%).

Table 2.1. $Sm_xZr_y(Co_{1-z}Fe_z)_{100-x-y}$ compositions prepared

Series	**x**	**y**	**z**
1	x = 13	y = 0	$0 \le z \le 0.5$
2	x = 14	y = 0	$0 \le z \le 0.5$
3	x = 15	y = 0	$0 \le z \le 0.5$
4	x = 13	$1 \le y \le 5$	z = 0.1
5	x = 14	$1 \le y \le 5$	z = 0.1
6	x = 15	$1 \le y \le 5$	z = 0.1

2.2 ANNEALING

About 250 mg of the as-milled powder was loaded into a 6 mm quartz tube with one sealed end inside the glove box. Quartz wool was stuffed into the open end of the tube to prevent powder from coming out later during evacuation. The small quartz tube was put inside a large 24 mm quartz tube that was then sealed using a brass fitting with an o-ring seal and a high vacuum valve. The assembled tube and valve were removed from the glovebox and attached to a diffusion pump system that was specifically designed for vacuum annealing. The tube was evacuated to 10^{-6} mbar. Once the tube reached the desired pressure, the tube was pushed into a tube furnace so that the sample at the end of the tube was in the hot zone of the furnace. The temperature was ramped at 10°/min from room temperature to the desired temperature. The tube was held at the chosen temperature for the desired length of time, and then cooled inside the furnace at a rate of 5°/min. The tube was continuously evacuated while in the furnace. When annealing was finished, the tube and valve assembly was put inside the glove box and the sample tube and sample were removed.

Annealing procedures were optimized using $Sm_{14}Co_{86}$ and $Sm_{13}Co_{87}$ powders. As-milled powders were annealed at various temperatures between 650°C and 850°C to determine the optimum annealing temperature. Then as-milled powders were annealed for times varying from five minutes to two hours at the optimum temperature to determine the optimum annealing time.

2.3 X-RAY DIFFRACTION

Powder x-ray diffraction (XRD) was carried out on both as-milled and annealed powders to determine the phases present. Diffraction patterns were taken in air using a Siemens D500 diffractometer using a 40 kV Cu tube to generate Cu-Kα radiation, $\lambda = 0.154$ nm. Samples were mounted on a glass slide using double-sided adhesive tape. Theta-two theta step scans were taken from 20° to 85° 2θ using 0.05° steps and a 3 s count time for each step. The XRD data was analyzed to determine the phases present, the lattice parameters of those phases, and the relative amounts of phases present.

2.4 SCANNING ELECTRON MICROSCOPY

Scanning Electron Microscopy (SEM) was performed at the TCD Center for Microscopy Analysis to study the morphology of the powder. Powders were studied loose or set in Bakelite metallographic mount and polished with progressively finer grades of Buehler Carbimet paper followed by diamond paste down to 0.25 μm. Energy dispersive x-ray analysis was attempted in the SEM as a means of evaluating the chemical composition of the powders, but was found to be inaccurate for evaluation of rare earth content.

2.5 VIBRATING SAMPLE MAGNETOMETRY

Room temperature vibrating sample magnetometery (VSM) was performed in a benchtop magnetometer where the variable field was created by two concentric Halbach cylinders[1]. The magnitude of the field was changed by rotating the cylinders so that the vector sum of their fields added to the desired applied field, up to a maximum of 1.1T. The sample was vibrated at 29.4 Hz along the bore of the cylinders (H ⊥ bore). This induces a voltage in a set of quadrupole pick up coils, also inside the bore, which can be converted

into a magnetic moment after calibration with a nickel standard. Samples were prepared outside the glovebox by mixing approximately 20 mg of annealed powder with Lecoset 7007 cold curing resin inside a 4 mm by 4 mm cylindrical Perspex bucket. The samples were then magnetized in an 8 T pulsed field prior to measurement.

Samples with room temperature coercivity 0.8 T < $\mu_0 H_c$ < 1.2 T were characterized in a standard electromagnet-based VSM. The magnetometer works on the same principle as the benchtop VSM. The sample was vibrated at 80 Hz perpendicular to the field direction while the sample's response was measured by pick up coils between the poles of the electromagnet. The maximum applied field was 1.4 T. Samples for room temperature measurement were set in Lecoset resin and magnetized before measurement.

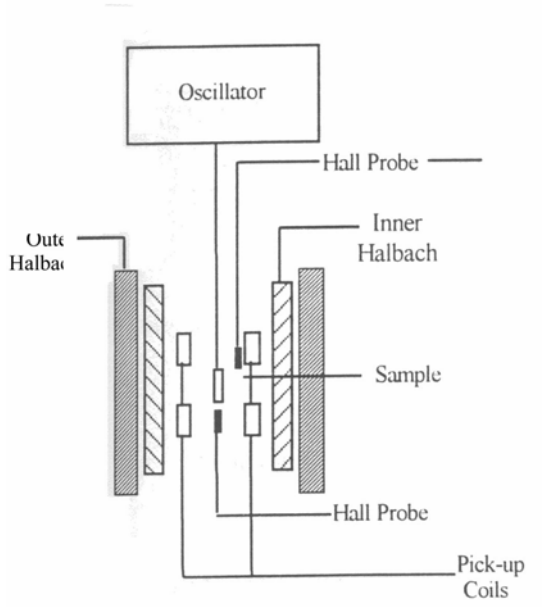

Figure 2.1. Schematic of Halbach cylinder based VSM used for magnetic characterization.

Measurements of hysteresis loops at high temperatures were also performed inside the electromagnet-based VSM, using a PAR furncace attachment (Figure 2.2). Approximately 10 mg of powder for high temperature measurement were sealed inside a 3 mm quartz tube using high temperature cement. Quartz wool was used as a buffer between the cement and the powder to prevent reaction between the two. Prepared samples were left in the

glovebox overnight to cure, and were then magnetized in an 8 T pulsed field before measurement. Hysteresis loops at 200, 300, and 400°C were measured under Ar in fields up to 1.4 T. A final loop was taken at 200°C after measurement at higher temperatures to check whether the sample had changed during the course of measurement.

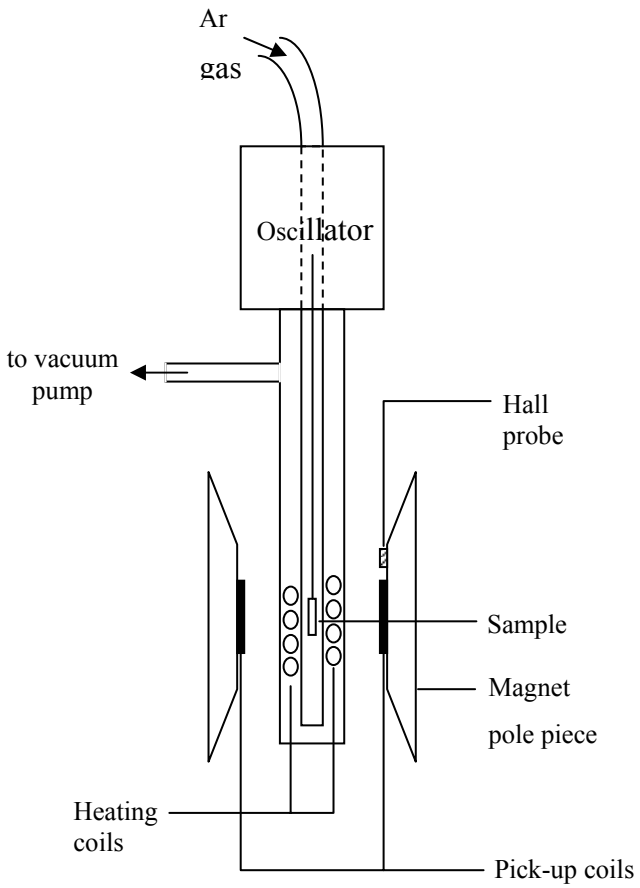

Figure 2.2. Schematic diagram of high temperature VSM

2.6 SQUID MAGNETOMETRY

Samples with large coercivity, greater than 1.2 T, were characterized using a Quantum Design Magnetic Properties Measurement System (MPMS), better known as a SQUID magnetometer. In this system, a superconducting magnet, a superconducting quantum interference device (SQUID) detection system and a high-performance temperature control system are integrated. This allows for rapid precision measurements over a temperature range of 1.9 to 400 K, and in fields up to 5 T. Automatic control and data collection are

provided for the system by a computer and two independent subsystem controllers.

Functional components of the system, shown in Figure 2.3, include a temperature control module, superconducting magnet system, SQUID detector system, sample handling system, and a gas handling system[2]. These components are all contained within a liquid nitrogen-jacketed liquid helium dewar. The liquid helium provides refrigeration for the superconducting components as well as providing for operation at low temperatures.

The temperature control system is under active control of the computer and control system electronics. Two thermometers are used for temperature sensing; one located at the center of the SQUID pick-up coils, and the other just below the sample chamber. Both sensors are used at temperatures above

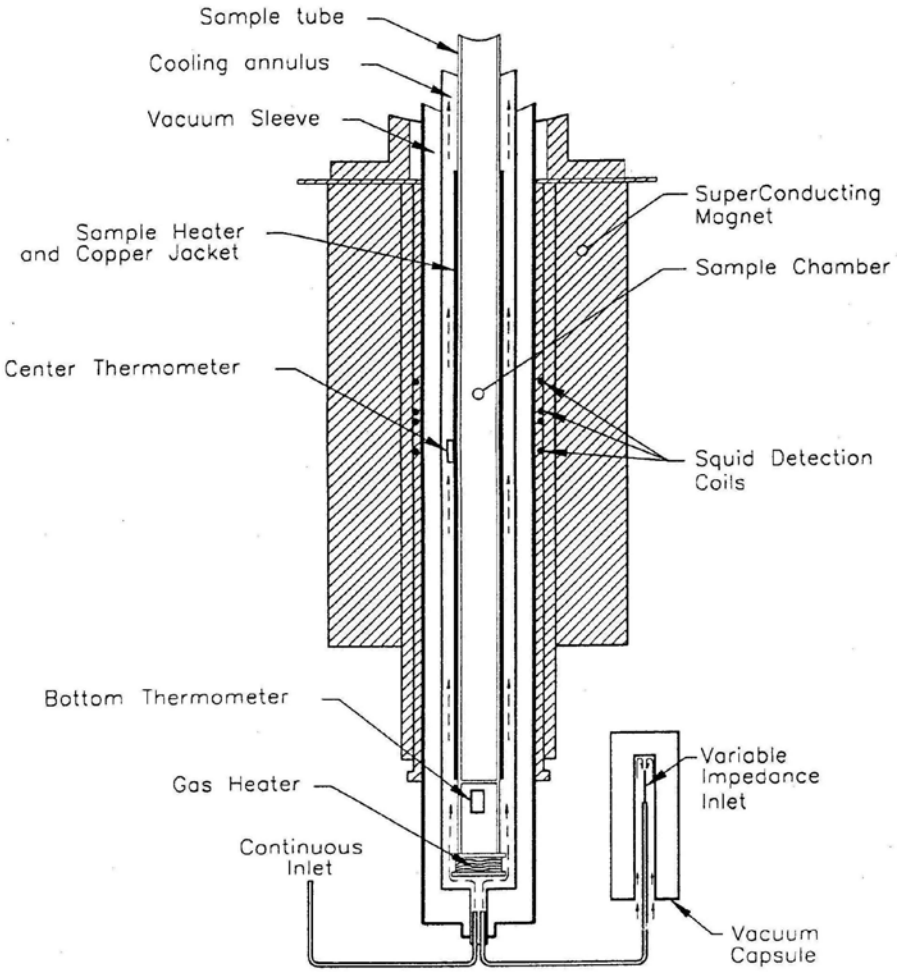

Figure 2.3. Schematic of SQUID magnetometer (after MPMS Hardware Reference Manual)

14 K, while at lower temperatures only the latter is active. This is to avoid inaccuracies caused by the presence of strong magnetic fields. Cooling from room temperature down to 4.2 K is provided by allowing a controlled amount of liquid He to enter the sample chamber, the He turns to gas and cools the chamber. To achieve lower temperatures, the system pressurizes this small reservoir of liquid helium. Sample space heating is achieved through a combination of a gas heater and chamber heater. These heaters can be used to achieve temperatures up to 400 K without any special attachments.

The field in the system is automatically changed by the MPMS control system when a magnetic field value is specified. The magnetic field generated by the superconducting solenoid is controlled through careful monitoring of the current supplied to the solenoid. The field is sustained by trapping a persistent current in the solenoid. The field is then changed either by injecting or removing current to get the desired field. In low resolution mode field is controlled to within 10^{-5} T, while in high resolution it is controlled to within 10^{-6} T.

The sample response is detected by a longitudinal SQUID system. This detection system is comprised of SQUID sensing loops, a superconducting transformer and the SQUID sensor and control electronics. The SQUID sensing loops are configured as a highly balanced second-derivative coil set with a total length of approximately 3 cm. The coils are designed to reject the field from the superconducting magnet to a precision of approximately 0.1%, making the SQUID detector relatively insensitive to drifts in the magnet. The coils measure the sample response to sensitivity of 10^{-11} J/T.

Measurements were performed using the Reciprocating Sample Option (RSO) sample handling system, rather than the standard DC (extraction) system. For this option, the sample is vibrated in the field, in the same way as in a VSM, but this time the vibration direction is parallel to the field direction. The main advantage of this option is shorter measurement times as compared to the DC system. Samples for room temperature measurements were prepared in the same way as for room temperature VSM; approximately 10 mg of powder was mixed with Lecoset resin inside a small perspex bucket. Samples were magnetized in an 8 T pulsed magnetic field before

measurement, and then mounted in a gelatin capsule inside a clear drinking straw for measurement. All measurements were controlled by the computer system. Sequence files were written to dictate the temperature, and measure hysteresis loops up to 5 T applied field. Examples of sequence files for all measurements using the SQUID magnetometer can be found in Appendix B.

2.7 RECOIL AND MAGNETIC VISCOSITY

Recoil curves and magnetic viscosity were measured along the demagnetization curve at various temperatures using the multiple step per loop method[3]. Measurements were taken along the demagnetization curve. The sample was first saturated in a 5 T field in the SQUID magnetometer. The field was then ramped to the required (negative) recoil field and held constant for 100s while the time dependence of the magnetization was recorded. Recoil curves were then measured by ramping the field to zero and then back to the recoil field. The field was then ramped in the negative direction to the next recoil field and the process repeated. An illustration of this is shown in Figure 1.7. Eight to twelve recoil fields were used per loop. Measurements were performed on each sample at 300, 200, 100, and finally 375 K. For the first measurement, at 300 K, the initial magnetization curve was measured on the virgin sample. Samples were prepared for these measurements by mixing

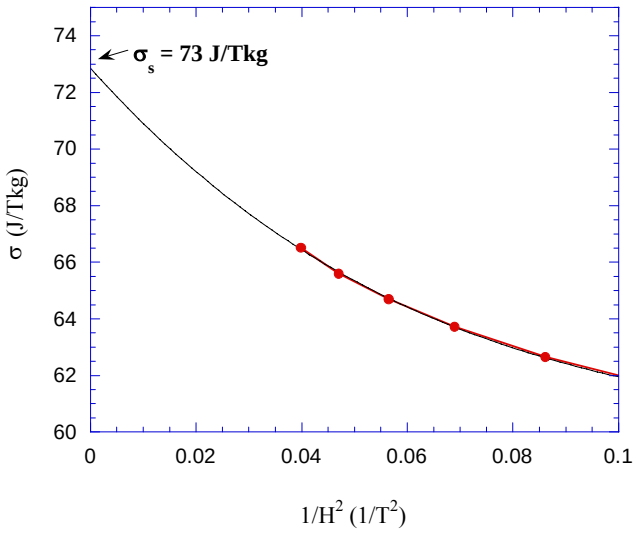

Figure 2.4. Example of calculation of σs for $Sm_{14}Zr_5(Co_{0.9}Fe_{0.1})_{81}$

the sample with high temperature cement. The mixture was then pushed into a brass mold and allowed to set. The final samples were approximately 2 mm in diameter and 1 cm long. The samples were not magnetized prior to measurement.

2.8 CALCULATION OF MAGNETIC QUANTITIES

Materials in this study did not fully saturate in a field of 5 T. As a result, it was necessary to use an extrapolation to determine σ_s. For all samples, σ_s was determined by plotting σ from the demagnetization curve vs $1/(\mu_0 H)^2$ and extrapolating to $1/(\mu_0 H)^2 = 0$ (i.e. $\mu_0 H = \infty$). This is illustrated in Figure 2.4.

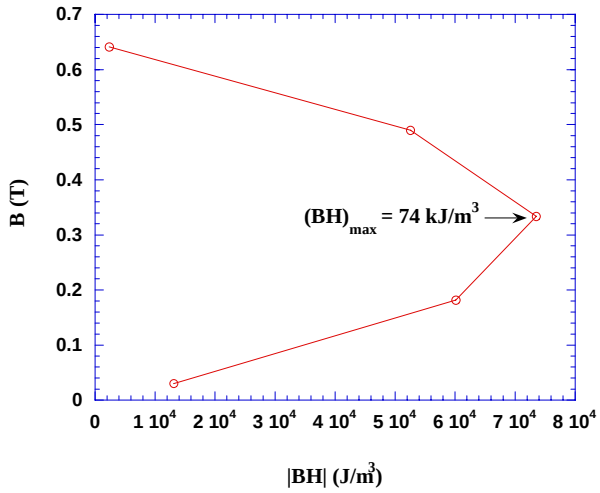

Figure 2.5. Example of calculation of energy product, $(BH)_{max}$ for $Sm_{14}Zr_3(Co_{0.9}Fe_{0.1})_{83}$

Calculation of the energy product $(BH)_{max}$ first required conversion of the data from σ(J/Tkg) and $\mu_0 H$ (T) to B(T) and H(A/m). A density of ρ = 8400 kg/m^3 was assumed for the materials, and then $M(A/m) = \sigma \cdot \rho$. The applied field was determined by dividing $\mu_0 H$ by $\mu_0 = 4\pi x10^{-7}$ Tm/A to get H(A/m). Now, the internal field $H_{int} = H - DM$, where the demagnetization factor, D, was assumed to be 1/3 because the particles were spherical (see section 3.1). Then $B = \mu_0(H_{int}+M)$ and B was plotted versus the absolute value of the product B·H to find $(BH)_{max}$ as illustrated in Figure 2.5.

[1] O. Cugat, R. Byrne, J. McCauley, and J.M.D. Coey, "A Compact Vibrating-Sample Magnetometer with Variable Permanent-Magnet Flux Source," *Review of Scientific Instruments* 65, no. 11 (1994), 3570-3573.

[2] *Magnetic Property Measurement System MPMS XL Hardware Reference Manual* (San Diego: Quantum Design, 1996)

[3] L. Folks and R. Street, "Analysis and interpretation of time dependent magnetic phenomena," *Journal of Applied Physics* 76 no. 10 (1994), 6391-6395; and D.C. Crew, R.C. Woodward, and R. Street, "Reversible magnetization behavior in $Sm_2(Co,Fe,Cu,Zr)_{17}$," *Journal of Applied Physics* 85 no. 8 (1999),5675-5677.

3 RESULTS

3.1 POWDER MORPHOLOGY

Figure 3.1 shows SEM photomicrographs of the $Sm_{14}Co_{86}$ as-milled powder. The powder particles are more or less spherical, with a rough popcorn-like appearance. Individual particles range from a few microns in size up to 20 μm, while agglomerations of particles can be up to 50 μm in size. This morphology is typical of the as-milled powders. This information combined with the grain size, estimated from x-ray line broadening, in the range of 10-20 nm (Section 3.3) suggests that each particle is composed of

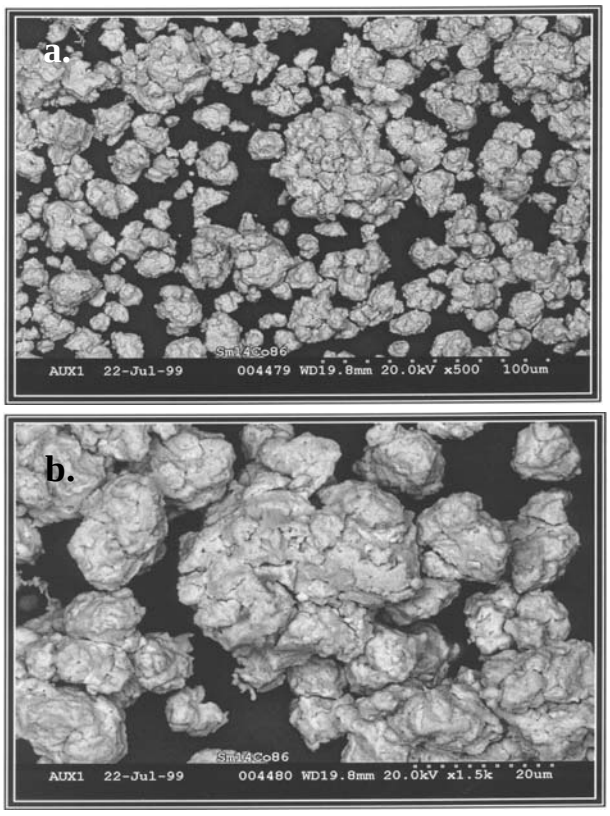

Figure 3.1. (a) SEM photomicrograph of Sm14Co86 as-milled powder, and (b) detail.

several grains. Chemical analysis performed on the binary compositions reveals an average of 0.06 wt% N_2 and 0.25 wt% O_2 in the samples. The oxygen would preferentially combine with Sm to form Sm_2O_3, harming the magnetic properties of the materials. This oxygen level is low enough to limit the Sm loss due to oxide formation to 4 at%. Actual Sm loss due to milling

was in the range of 2 – 3 wt %, as measured using ICP. This means that the $Sm_{14}Co_{86}$ nominal composition sample has an actual composition of $Sm_{12.5}Co_{87.5}$. ICP also showed that contamination from the milling pot was minimal, with < 5 wt% Fe, and < 0.1 wt% Cr. This analysis was performed by Sheffield Analytical Services, UK.

3.2 ANNEALING OPTIMIZATION

Figure 3.2 shows the dependence of coercivity and remanence ratio, M_r/M_s, on annealing temperature for $Sm_{14}Co_{86}$. Both properties peak for 750°C < T_{ann} < 800°C. Consequently, 775°C was chosen as the best

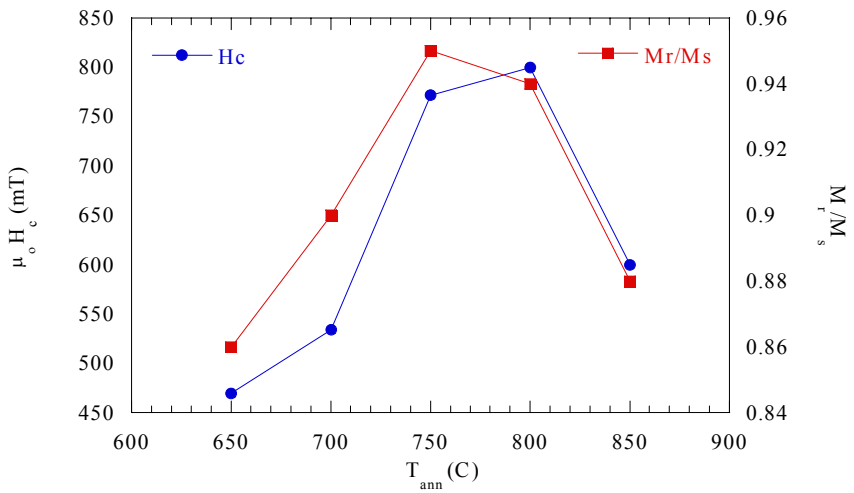

Figure 3.2. Dependence of room temperature coercivity and remanence ratio on annealing temperature

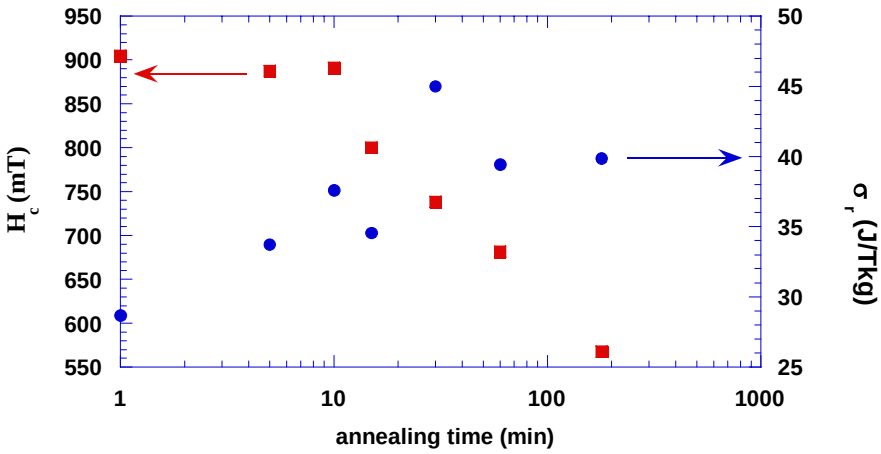

Figure 3.3. Dependence of room temperature H_c and σ_r on annealing time at 775°C for $Sm_{13}Co_{87}$

temperature for annealing the materials.

The dependence of coercivity on annealing time at 775°C for $Sm_{13}Co_{87}$ is shown in Figure 3.3. Coercivity decreases with increasing annealing time. This is probably due to an increase in grain size with increased annealing time. Five minutes was finally chosen as the best annealing time because it gave the best value of σ_r with the least loss in coercivity at room temperature (Figure 3.3). All samples were annealed for 5 minutes at 775°C after this optimization.

3.3 Structure and Phase Analysis

Typical powder x-ray diffraction patterns for the as-milled materials showed only a broad hump around 44° 2θ, as shown in Figure 3.4. This is indicative of an amorphous structure. Substitution of large amounts of Fe lead to the emergence of some α-Fe peaks, which were so broad as to indicate a very small crystallite size of approximately 10 nm. No such crystalline peaks were observed with Zr substitution (Figure 3.5)

Figure 3.6 shows X-ray patterns typical for samples annealed at 650°C ≤ T_{ann} ≤ 800°C. At high temperatures, peaks corresponding to fcc Co begin to emerge. This is indicative of a loss of Sm during annealing at these temperatures. This is confirmed by the presence of a metallic coating on the quartz tube after annealing at high temperature.

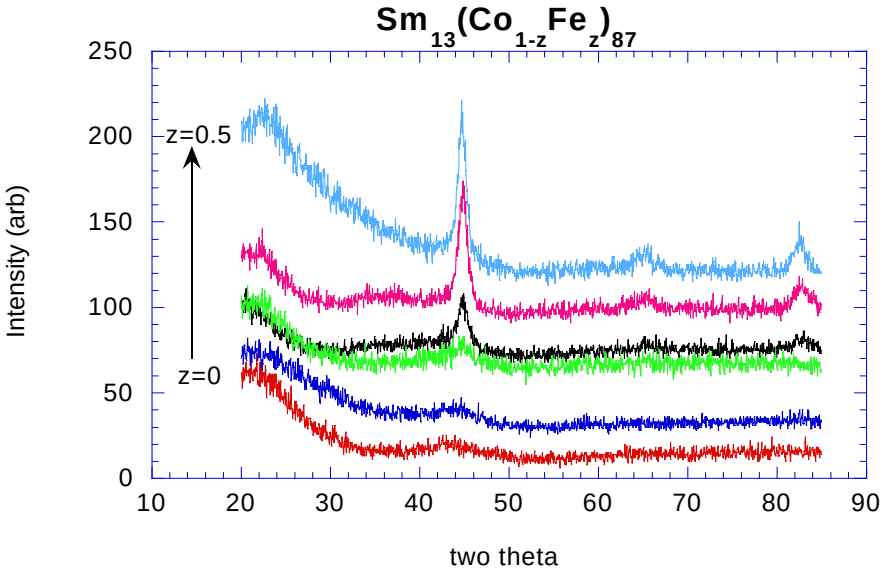

Figure 3.4. Typical X-ray diffraction patterns for as-milled materials with Fe substitution

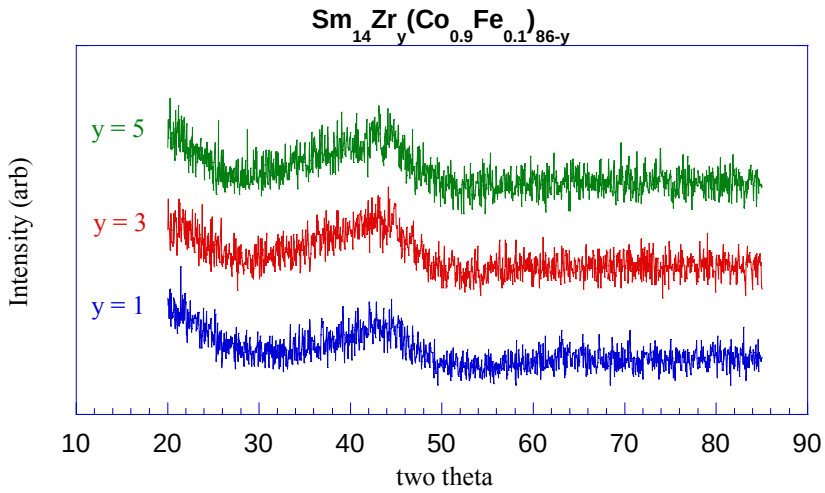

Figure 3.5. Typical X-ray diffraction patterns for as-milled materials with Zr substitution

Figure 3.7 shows a selection of x-ray patterns for samples annealed using the optimized procedure. The patterns show peaks for both $SmCo_5$ and Sm_2Co_{17} phases. The Sm_2Co_{17} peaks that are present are the main reflections that are shared by both the hexagonal (Th_2Ni_{17}) and rhombohedral (Th_2Zn_{17}) structure types. It is probable that both structure types are present in the Sm_2Co_{17} phase. In samples with no substitution, or small amounts of Fe, it is difficult to resolve the $SmCo_5$ (111) and Sm_2Co_{17} (220) and (302)/(303) peaks at around 44° 2θ. As more Fe is added, the peaks become narrower, more distinct, and more intense. This is indicative of an increase in grain size of the samples. The addition of Zr has the opposite effect. With addition of Zr, the peaks become broader, less intense, and more difficult to separate, indicating a decrease in grain size. Lattice parameters for both phases were calculated using a least squares method that included all peak positions[1]. Lattice parameters for the $SmCo_5$ phase were in the range 0.500 nm < **a** < 0.510 nm and 0.393 nm < **c** < 0.405 nm, and were in the range 0.841 nm < **a** < 0.849 nm and 0.810 nm < **c** < 0.828 nm for the Sm_2Co_{17} phase. Lattice parameters **a** and **c** for both phases increased with substitutions of Fe, and remained relatively constant or slightly increased with Zr substitution. The ratio **c**/**a** increased very slightly with both Fe and Zr substitution, and was around 0.79 for the $SmCo_5$ and 0.97 for the Sm_2Co_{17} phase.

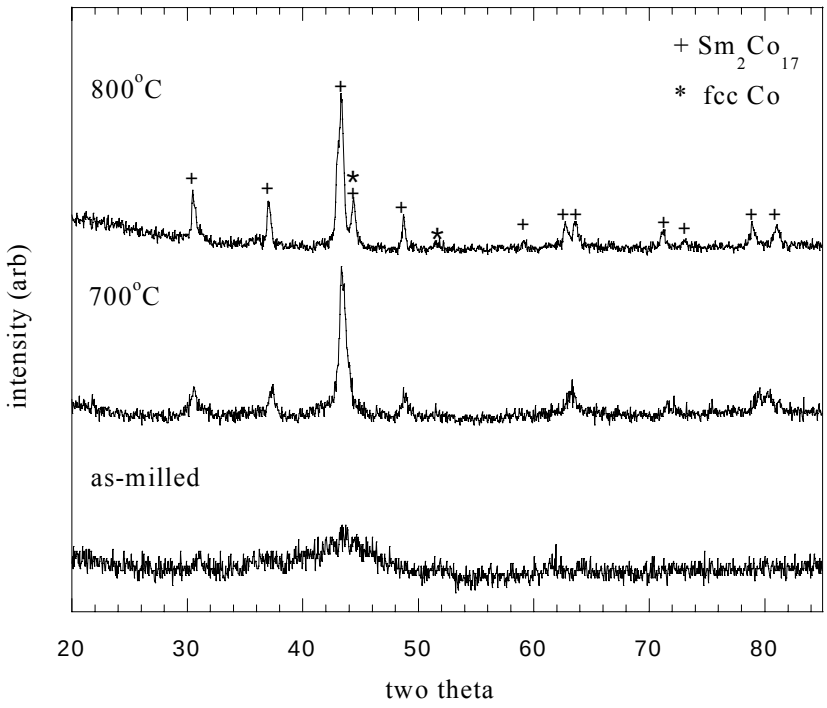

Figure 3.6. Typical X-ray diffraction patterns for $Sm_{14}Co_{86}$ annealed at various temperatures during annealing optimization. Sm loss at high temperatures is evidenced by the appearance of fcc Co peaks in the XRD patterns.

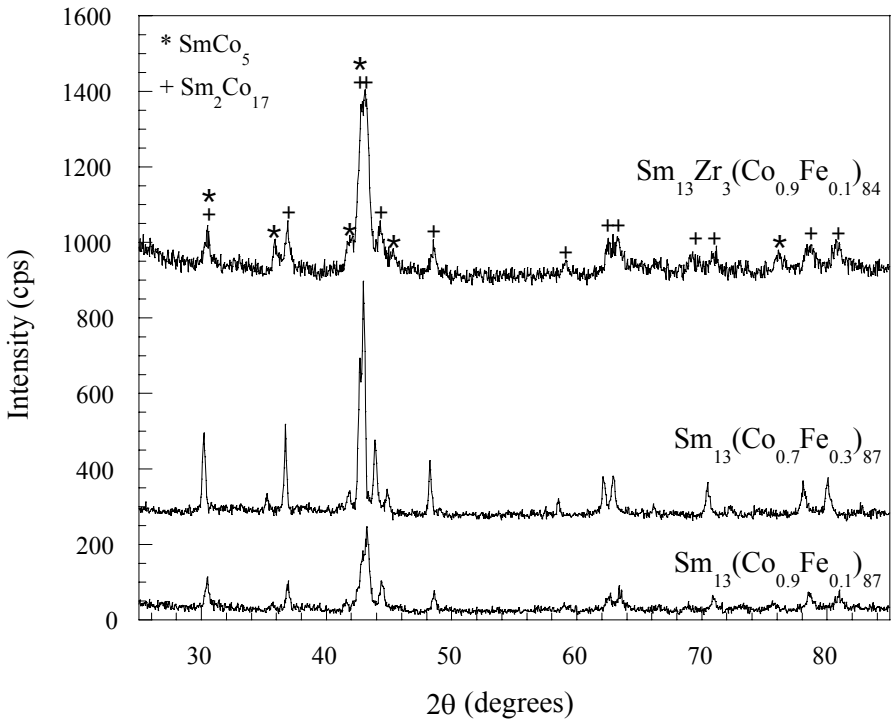

Figure 3.7. X-ray diffraction patterns for $Sm_{13}Zr_y(Co_{1-x}Fe_x)_{87-y}$ materials. $SmCo_5$ and Sm_2Co_{17} (hexagonal and rhombohedral) phases are present in all samples.

The grain size in the materials was estimated from X-ray diffraction data using the Sherrer formula[2]

$$t = \frac{0.9\lambda}{B\cos\theta_B} \qquad (3.1)$$

where t is the thickness of the grain, λ is the wavelength of the X-ray radiation, 0.154 nm in this case, B is the full width at half maximum of a chosen peak in the X-ray pattern, and θ_B is the Bragg angle of the peak. Calculations were made using the $SmCo_5$ (110) and Sm_2Co_{17} (300) reflections, and revealed an average grain size of 35 nm for the $SmCo_5$ phase, and 30 nm for the Sm_2Co_{17} phase. These numbers should only be used as an indication because the Sherrer formula does not take into account line broadening due to effects other than size, e.g. strain. Also, the Sm_2Co_{17} (300) peak is common to both the hexagonal and rhombohedral structure types, and so here it is impossible to know which phase is being measured, if not both.

Relative amounts of the phases present were determined using the direct comparison method described by Cullity[2], where integrated intensities are compared using the relation

$$\frac{I_\gamma}{I_\alpha} = \frac{R_\gamma c_\gamma}{R_\alpha c_\alpha} \qquad (3.2)$$

where c_α and c_γ are the volume fractions of the phases present and $c_\gamma + c_\alpha = 1$. R is given by

$$R = \left(\frac{1}{v^2}\right)\left[|F|^2\ p\left(\frac{1+\cos^2 2\theta}{\sin^2\theta\cos\theta}\right)\right]\left(e^{-2M}\right) \qquad (3.3)$$

where v is the volume of the unit cell (in m^3), F is the structure factor, p is the multiplicity factor, and e^{-2M} is the temperature factor, related to the Debye temperature. For a hexagonal crystal, $v = (\sqrt{3}/2)a^2c$. The structure factor is given by

$$F_{hkl} = \sum_1^N f_n e^{2\pi i(hu_n + kv_n + lw_n)}\ , \qquad (3.4)$$

3.4 MAGNETIC PROPERTIES

3.4.1 Room Temperature

Room temperature magnetization curves for the binary compounds are shown in Figure 3.9. These curves, like all of those observed at room temperature in this study, show smooth demagnetization and enhanced remanance (σ_r/σ_s >0.5), indicating intergrain exchange coupling among fine grains. The binary compounds exhibit large coercivities, in excess of 1 T, increasing with Sm content. Figure 3.10 shows selection of demagnetization curves for $Sm_{14}(Co_{1-z}Fe_z)_{86}$, demonstrating the effect of Fe substitution on the room temperature demagnetization curves. Addition of Fe increases σ_r and σ_s, with maximum values occurring for z = 0.3 – 0.4. Coercivity reaches a maximum for z =0.1 for all Sm compositions (Figure 3.11). Consequently, z = 0.1 was chosen as the best Fe content regardless of Sm content to give an

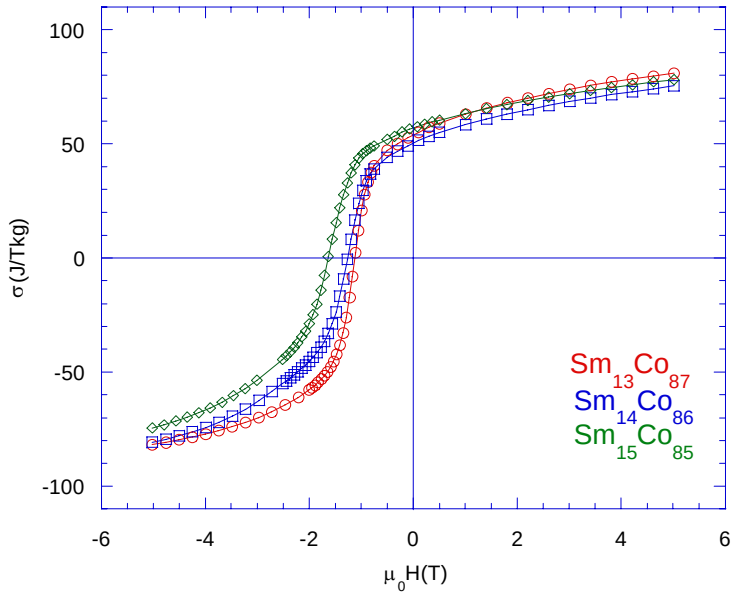

Figure 3.9. Room temperature demagnetization curves for Sm_xCo_{100-x}

increase in remanence without decrease in coercivity. Further work studying Zr substitution into these compounds was carried out with z = 0.1.

Selection of an optimum Zr content is less straightforward. Figure 3.12 shows the influence of Zr content on μ_0H_c and $(BH)_{max}$. Coercivity and σ_r/σ_s increase with increasing Zr (or Sm), while $(BH)_{max}$, σ_r, and σ_s all decrease with increased Zr (or Sm). Figure 3.13 plots coercivity versus energy product.

summed over the N atoms in the unit cell, where (u_n,v_n, w_n) are the coordinates of the atoms, and f_n are the atomic scattering factors of those atoms. The expression in parentheses is the Lorentz-polarization factor,

$$\text{Lorentz-polarization factor} = \frac{1+\cos^2 2\theta}{\sin^2\theta\cos\theta}. \qquad (3.5)$$

This factor is a combination of geometrical factors that affect the intensity of reflections. The temperature factor e^{-2M} was assumed to be approximately the same for the two phases, and so cancelled in the calculation.

The $SmCo_5$ (110) and Sm_2Co_{17} (300) reflections were used for the calculation of volume fraction of the phases present. The results, shown in figure 3.8, show that addition of Fe favors the formation of the Sm_2Co_{17} phase, while addition of Zr favors the formation of the $SmCo_5$ phase. This holds true for all Sm contents studied.

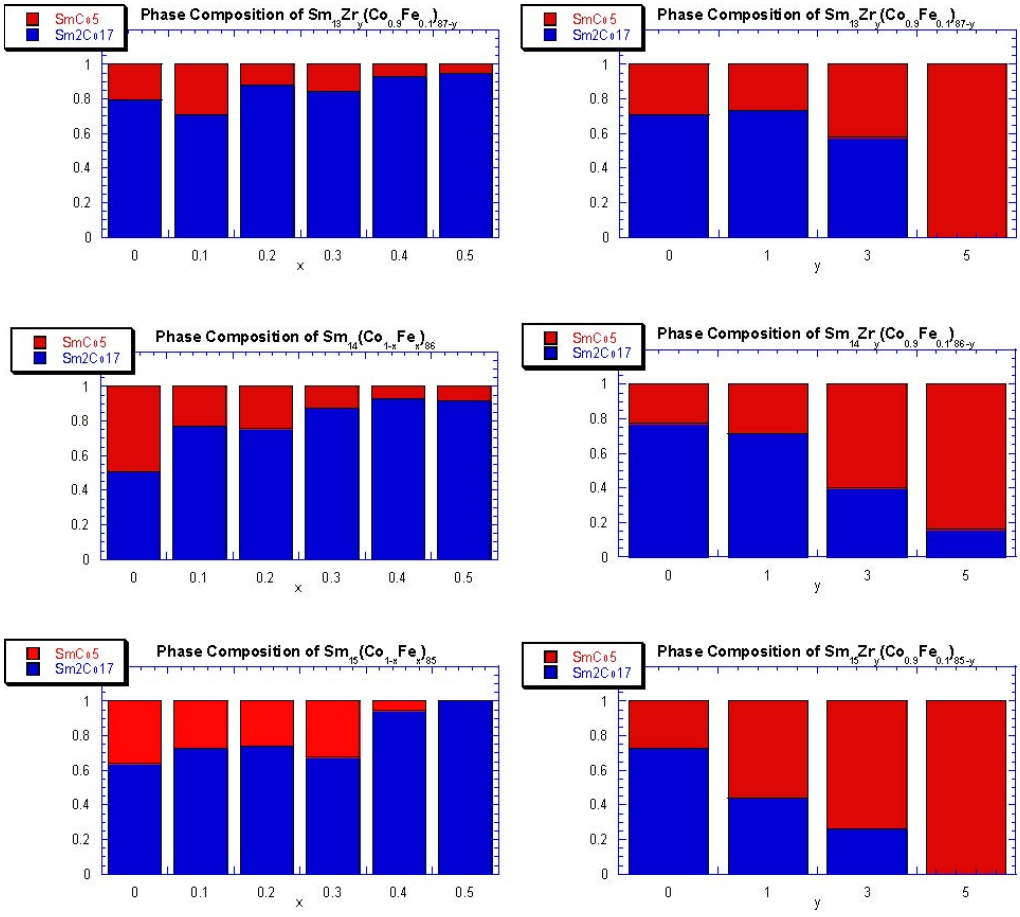

Figure 3.8. Calculated phase constitution of mechanically alloyed $Sm_zZr_y(Co_{1-x}Fe_x)_{100-z-y}$

Table 3.1 summarizes room temperature magnetic properties for all compositions. Figure 3.14 shows the demagnetization curves for the compositions with best energy product ($Sm_{13}Zr_1(Co_{0.9}Fe_{0.1})_{86}$), best remanence ratio ($Sm_{14}Zr_5(Co_{0.9}Fe_{0.1})_{81}$), and best coercivity ($Sm_{15}Zr_5(Co_{0.9}Fe_{0.1})_{80}$). From the phase analysis (Section 3.3), the first composition contained around 75% Sm_2Co_{17} phase, the second had around 80% $SmCo_5$ phase, and the latter was nearly entirely (>95%) $SmCo_5$ (XRD cannot reveal secondary phases if there is less than 5% present).

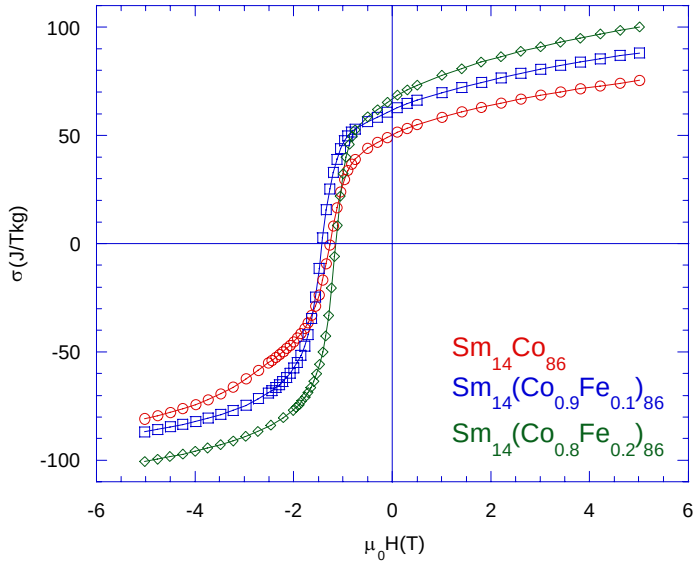

Figure 3.10. Room temperature demagnetization curves for $Sm_{14}(Co_{1-z}Fe_z)_{86}$

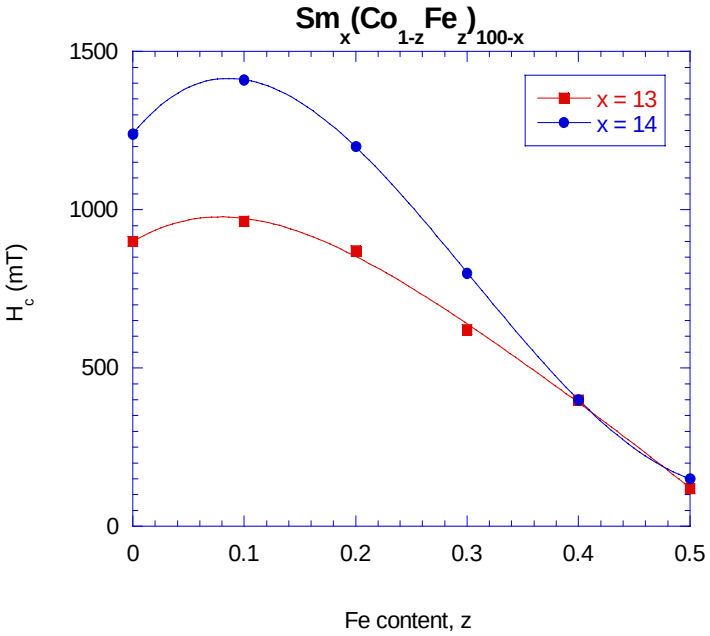

Figure 3.11. Effect of Fe content on coercivity for $Sm_x(Co_{1-z}Fe_z)_{100-x}$

Table 3.1. Summary of room temperature properties

composition	μ_0Hc(T)	σ_r(J/Tkg)	σ_s(J/Tkg)	σ_r/σ_s	$(BH)_{max}$ (kJ/m^3)
$Sm_{13}Co_{87}$	1.1	54	88	0.62	61
$Sm_{13}(Co_{0.9}Fe_{0.1})_{87}$	1.2	68	110	0.62	100
$Sm_{13}(Co_{0.8}Fe_{0.2})_{87}$	1.0	63	107	0.59	85
$Sm_{13}(Co_{0.7}Fe_{0.3})_{87}$	0.7	72	107	0.68	107
$Sm_{13}(Co_{0.6}Fe_{0.4})_{87}$	0.4	61	106	0.58	73
$Sm_{13}(Co_{0.5}Fe_{0.5})_{87}$	0.1	32	128	0.25	31
$Sm_{13}Zr_1(Co_{0.9}Fe_{0.1})_{86}$	1.3	69	108	0.64	101
$Sm_{13}Zr_3(Co_{0.9}Fe_{0.1})_{84}$	1.6	67	102	0.65	94
$Sm_{13}Zr_5(Co_{0.9}Fe_{0.1})_{82}$	1.8	50	75	0.67	54
$Sm_{14}Co_{86}$	1.2	50	85	0.59	53
$Sm_{14}(Co_{0.9}Fe_{0.1})_{86}$	1.4	62	101	0.61	80
$Sm_{14}(Co_{0.8}Fe_{0.2})_{86}$	1.1	67	116	0.58	94
$Sm_{14}(Co_{0.7}Fe_{0.3})_{86}$	0.8	64	91	0.71	85
$Sm_{14}(Co_{0.6}Fe_{0.4})_{86}$	0.4	58	99	0.59	66
$Sm_{14}(Co_{0.5}Fe_{0.5})_{86}$	0.2	40	133	0.30	48
$Sm_{14}Zr_1(Co_{0.9}Fe_{0.1})_{85}$	1.6	63	97	0.65	85
$Sm_{14}Zr_3(Co_{0.9}Fe_{0.1})_{83}$	1.7	58	87	0.67	74
$Sm_{14}Zr_5(Co_{0.9}Fe_{0.1})_{81}$	2.0	50	73	0.68	53
$Sm_{15}Co_{85}$	1.6	57	90	0.63	70
$Sm_{15}(Co_{0.9}Fe_{0.1})_{85}$	1.0	61	101	0.61	77
$Sm_{15}(Co_{0.8}Fe_{0.2})_{85}$	1.2	57	102	0.56	66
$Sm_{15}(Co_{0.7}Fe_{0.3})_{85}$	1.1	57	97	0.59	65
$Sm_{15}(Co_{0.6}Fe_{0.4})_{85}$	0.5	60	97	0.62	74
$Sm_{15}(Co_{0.5}Fe_{0.5})_{85}$	0.2	41	124	0.33	44
$Sm_{15}Zr_1(Co_{0.9}Fe_{0.1})_{84}$	1.8	60	90	0.67	78
$Sm_{15}Zr_3(Co_{0.9}Fe_{0.1})_{82}$	2.0	52	76	0.68	58
$Sm_{15}Zr_5(Co_{0.9}Fe_{0.1})_{80}$	2.1	38	57	0.67	32

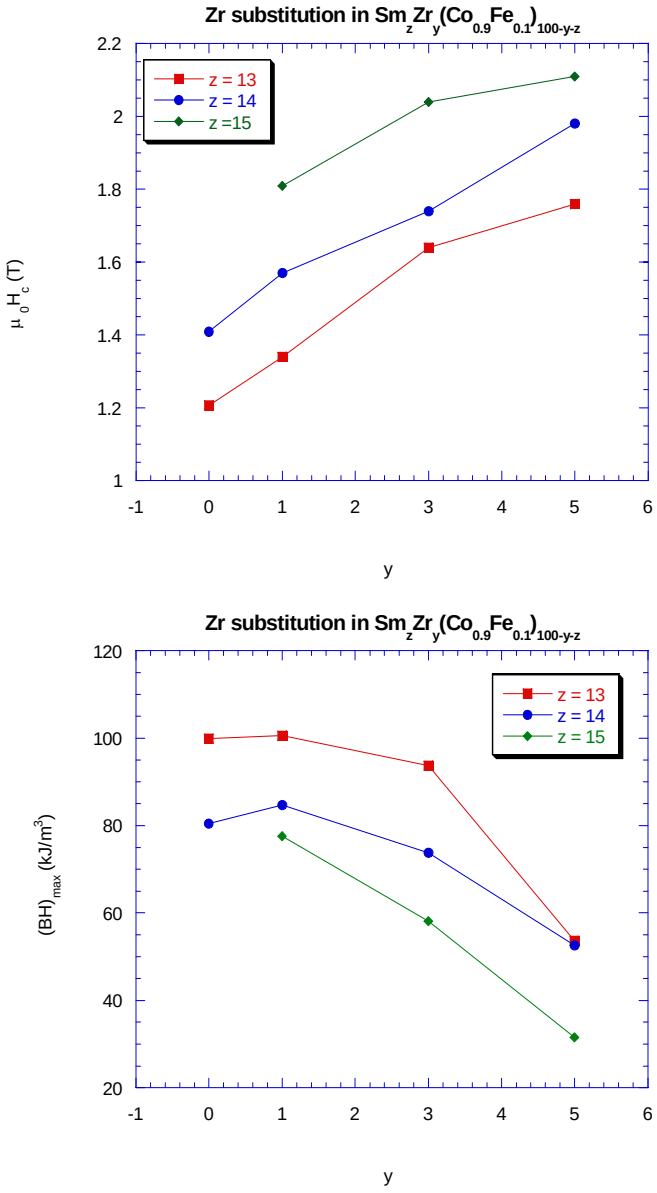

Figure 3.12 Effect of Zr substitution on coercivity and energy product

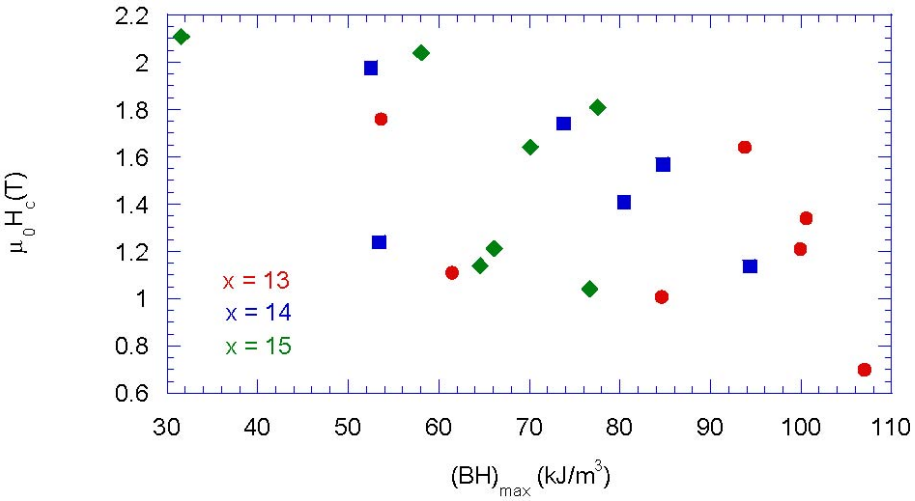

Figure 3.13. Coercivity versus energy product for $Sm_xZr_v(Co_{1-z}Fe_z)_{100-x-v}$ at room temperature

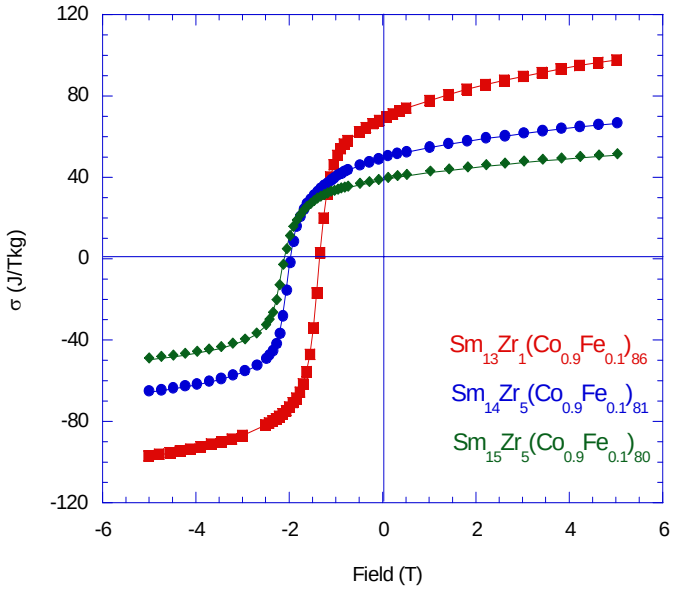

Figure 3.14. Room temperature demagnetization curves showing the best properties

3.4.2 High Temperature

Typical high temperature hysteresis loops for Zr-substituted samples are shown in Figure 3.15 (a). As temperature is increased, the formerly smooth demagnetization curve becomes that of a two-phase mixture. At 400°C, σ(1.4 T) is larger than it had been at 200°C and 300°C, and the loop crosses over itself as it returns to the maximum positive field. This suggests that the sample is undergoing some irreversible change as it is held at high temperature for the duration of the measurement, which is approximately 30 minutes per loop. The final loop taken at 200°C confirms this. This loop, shown in Figure 3.15(b), is significantly different from the first loop taken at 200°C. X-ray diffraction on a Zr-substituted sample offers little insight. The peaks are very slightly narrower. There is also a small suggestion of the presence of the cubic Zr_6Co_{23} phase, but it is difficult to resolve because the lines for the phase overlap with those for the $SmCo_5$ and Sm_2Co_{17} phases.

The high temperature loops for compositions without Zr are significantly different (Figure 3.16). In these compositions, the demagnetization curves are smoother than those of Zr-containing alloys, and the increase in σ(1.4 T) is

smaller. In addition, there is not as great a difference between the two loops taken at 200°C.

The temperature dependence of coercivity for mechanically alloyed $Sm_xZr_y(Co_{0.9}Fe_{0.1})_{100-x-y}$ is shown in Figure 3.17. No matter what the composition or room temperature coercivity, μ_0H_c at 300°C is around 0.6 T. The temperature coefficient of coercivity, β(20-300), was calculated for the samples. The point at 300°C was used instead of the one at 400°C because the samples did not seem to undergo irreversible changes at the lower temperature. The values for β(20-300) were in the range –0.2%/°C to –0.3%/°C. The values for samples without Zr were smaller than those for samples with Zr, with the most obvious difference for the samples with x = 13. Table 3.2 summarizes the data for temperature dependence of coercivity.

Table 3.2 Summary of magnetic properties

composition	μ_0H_c(20°C) T	$(BH)_{max}$(20°C) (kJ/m^3)	β(20–300) %/°C
$Sm_{13}(Co_{0.9}Fe_{0.1})_{87}$	1.2	100	-0.22
$Sm_{13}Zr_1(Co_{0.9}Fe_{0.1})_{86}$	1.3	101	-0.27
$Sm_{13}Zr_3(Co_{0.9}Fe_{0.1})_{84}$	1.6	94	-0.25
$Sm_{13}Zr_5(Co_{0.9}Fe_{0.1})_{82}$	1.8	54	-0.24
$Sm_{14}(Co_{0.9}Fe_{0.1})_{86}$	1.4	80	-0.21
$Sm_{14}Zr_1(Co_{0.9}Fe_{0.1})_{85}$	1.6	85	-0.23
$Sm_{14}Zr_3(Co_{0.9}Fe_{0.1})_{83}$	1.7	74	-0.23
$Sm_{14}Zr_5(Co_{0.9}Fe_{0.1})_{81}$	2.0	53	-0.25
$Sm_{15}Zr_1(Co_{0.9}Fe_{0.1})_{84}$	1.8	78	-0.23
$Sm_{15}Zr_3(Co_{0.9}Fe_{0.1})_{82}$	2.0	58	-0.24
$Sm_{15}Zr_5(Co_{0.9}Fe_{0.1})_{80}$	2.1	32	-0.25

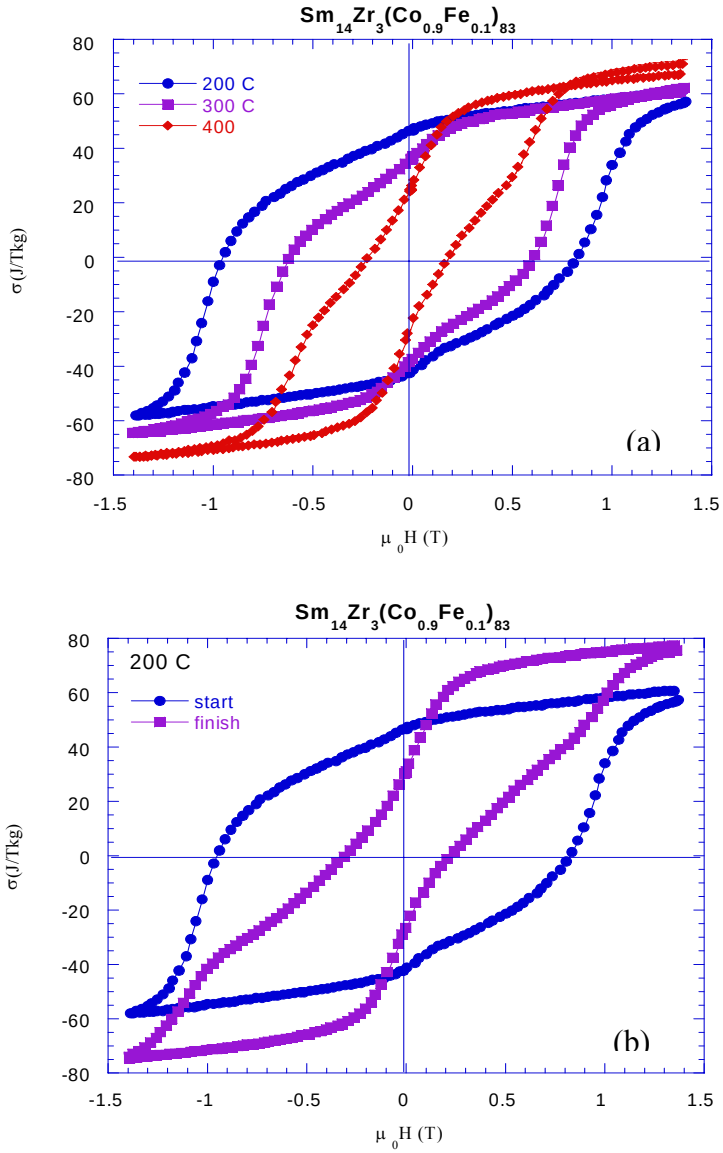

Figure 3.15. (a) High temperature hysteresis loops for $Sm_{14}Zr_3(Co_{0.9}Fe_{0.1})_{83}$. The loops start to show two phase character and σ(1.4 T) increases for T > 300°C, suggesting irreversible changes in the sample. (b) Comparison of hysteresis loop taken at 200°C after measurement up to 400°C with 200°C loop taken before measurement.

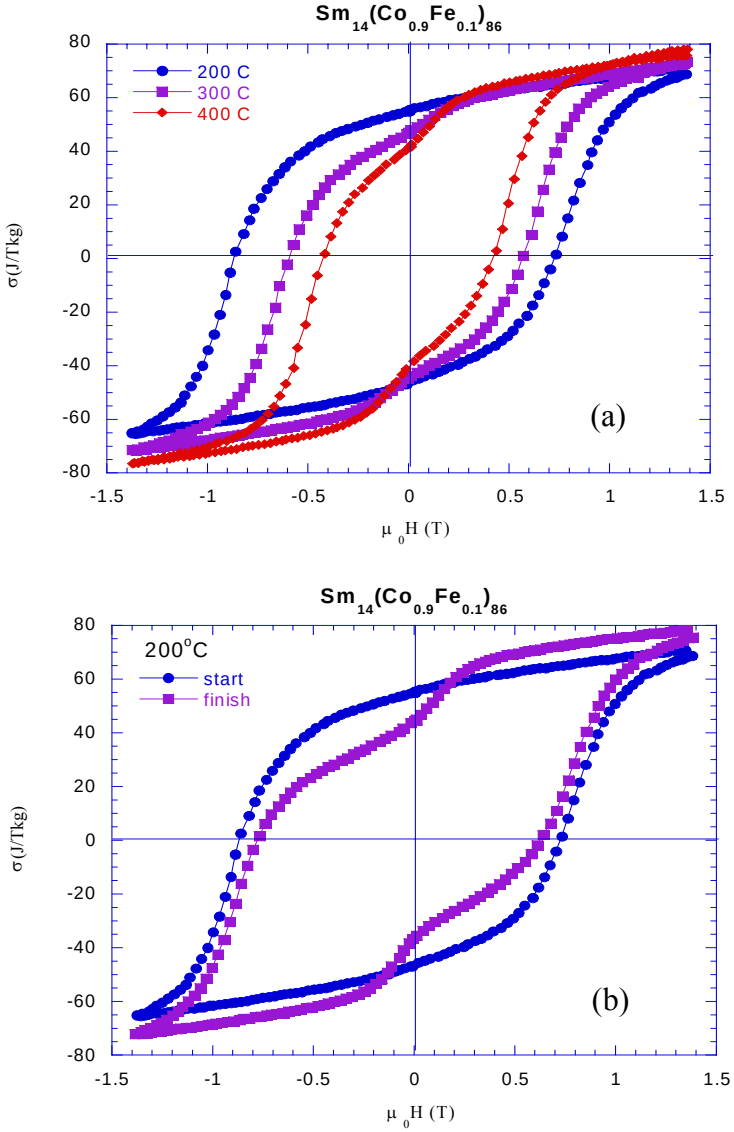

Figure 3.16. (a) High temperature hysteresis loops for $Sm_{14}(Co_{0.9}Fe_{0.1})_{86}$. (b) comparison of hysteresis loop taken at 200°C after measurement up to 400°C with 200°C loop taken before measurement up to 400°C. The samples without Zr do not suffer as badly from irreversible changes as the samples with Zr substitution.

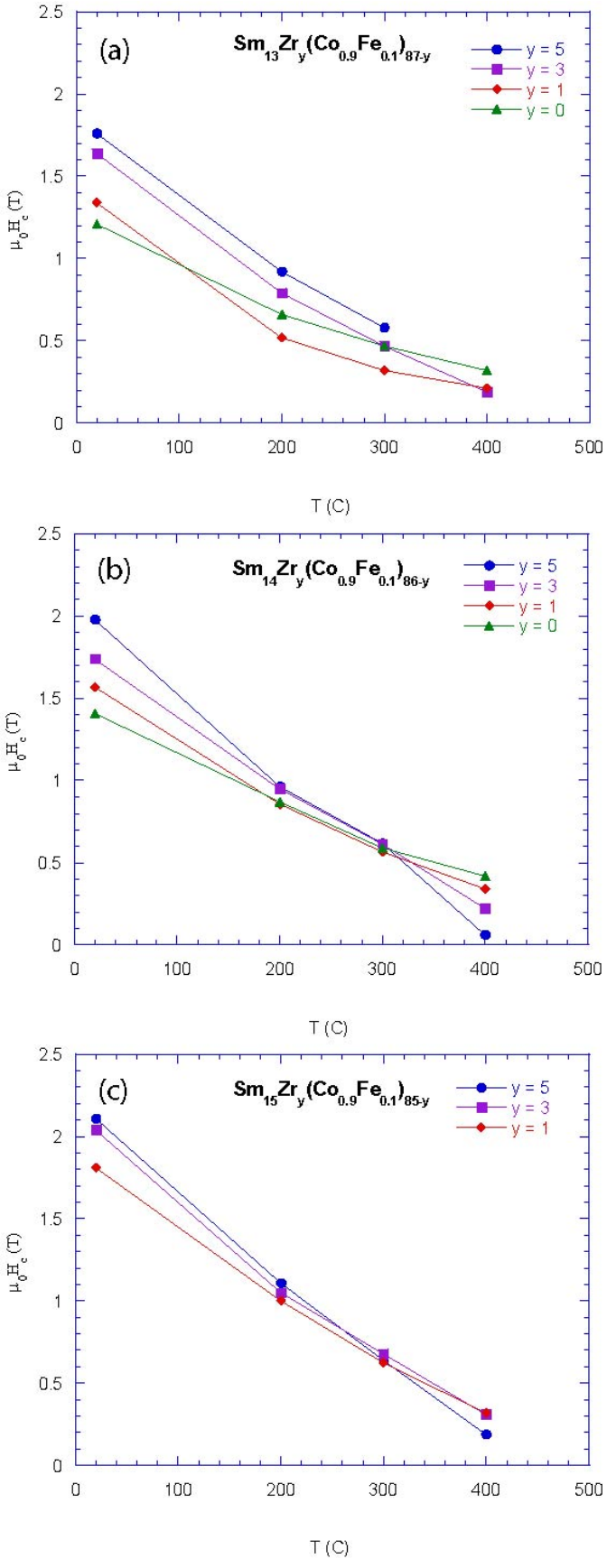

Figure 3.17. Temperature dependence of coercivity in (a) $Sm_{13}Zr_y(Co_{0.9}Fe_{0.1})_{87-y}$, (b) $Sm_{14}Zr_y(Co_{0.9}Fe_{0.1})_{86-y}$, and (c) $Sm_{15}Zr_y(Co_{0.9}Fe_{0.1})_{85-y}$

3.5 RECOIL AND MAGNETIC VISCOSITY

Typical experimental results for the recoil and magnetic viscosity measurements are shown in Figure 3.18. The initial magnetization curves, shown in Figure 3.19, are of mixed type for all compositions studied (Section 1.3.1.3). Addition of Fe has no effect on the nature of the curve, while Zr addition very slightly shifts the initial curve towards a more pinning-type nature.

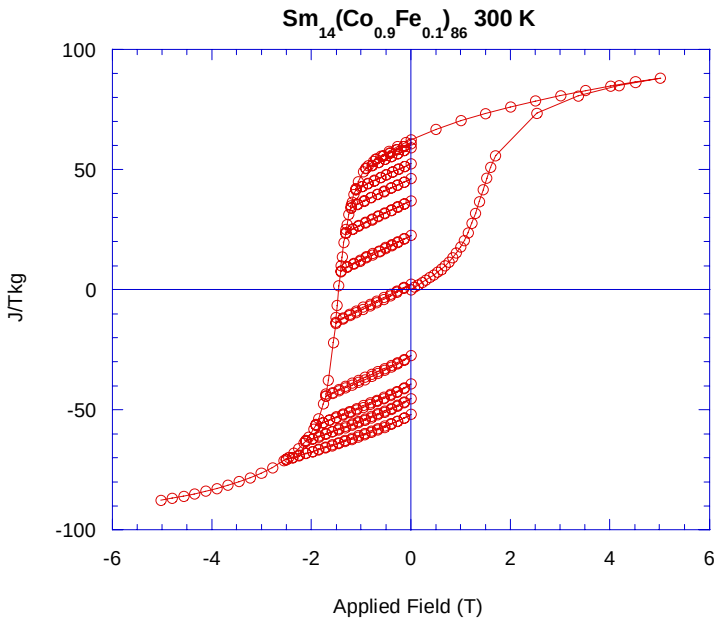

Figure 3.18 Example of recoil and magnetic viscosity results

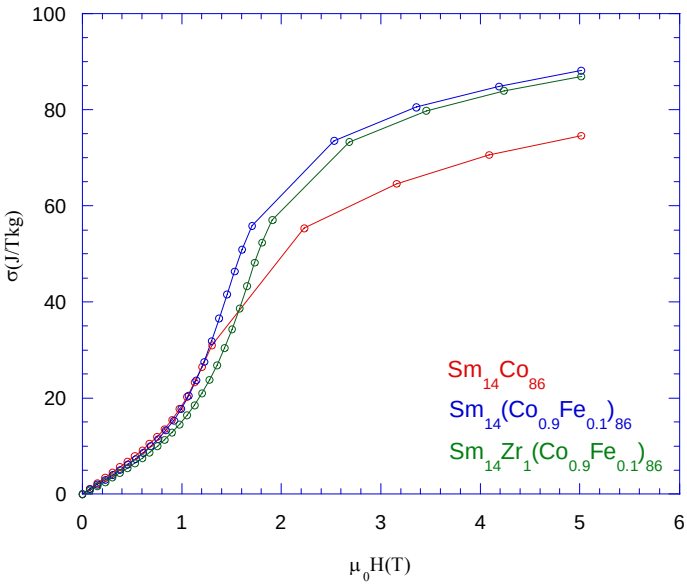

Figure 3.19. Initial magnetization curves, showing mixed nucleation and pinning type character for all compositions

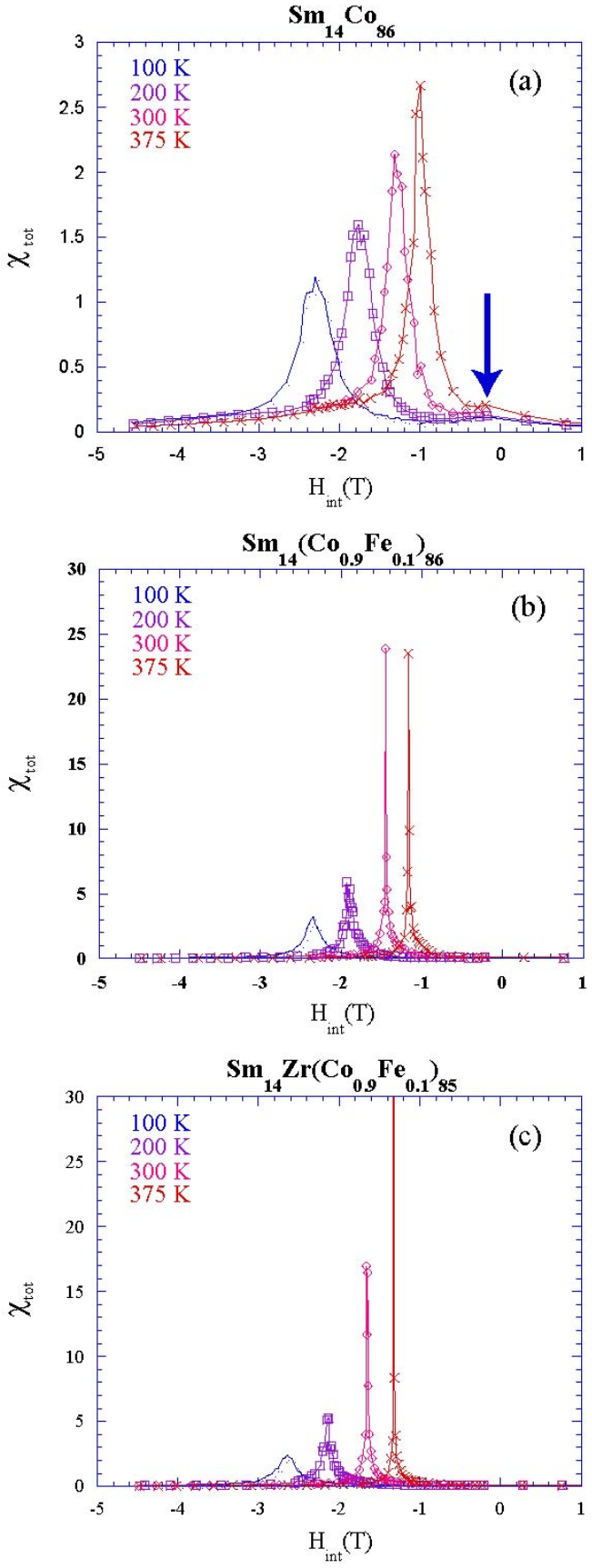

Figure 3.20. χ_{tot} for all compositions and temperatures studied. (a) shows reversal of a soft phase at small reverse fields, indicated by the arrow, followed by a sharp reversal of the hard phases. (b) and (c) show increasingly sharp reversal with Fe and Zr substitution and no evidence of soft phase.

Plots of χ_{tot} (=∂M/∂H of the major loop) are shown in Figure 3.20. These plots reveal that binary compound actually has a small amount of soft phase present. This is revealed by the trace of a small peak in χ_{tot} just below H_{int} = 0 at all temperatures. This shows up in the derivative curve, but is not evident in the σ(H) curve (Figure 3.9). Careful examination of the curves for the Fe- and Zr-substituted compounds reveals no such peak. At the coercivity, all compositions studied show a sharp reversal, which is enhanced by both Fe and Zr additions.

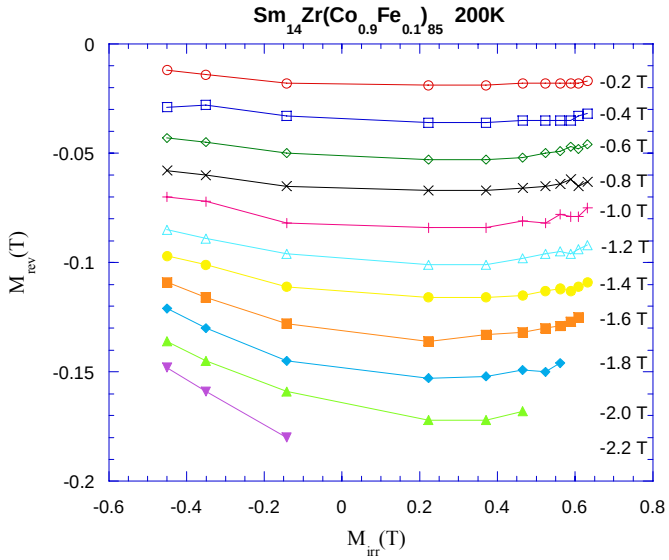

Figure 3.21. M_{rev} vs M_{irr} curves for $Sm_{14}Zr(Co_{0.9}Fe_{0.1})_{85}$

Figure 3.21 shows a typical M_{rev} vs M_{irr} plot. All plots were similar, regardless of composition or temperature. The curves have a very shallow curving nature.

Temperature dependence of activation volume is shown in Figure 3.22. The standard method and Givord method of calculating the activation volume give similar results. The results from the Givord method are slightly smaller, but they are within experimental error. Correction to the standard result by η does not significantly change the results. Error bars are shown on results for V_a from both the standard method and the corrected standard method because these methods actually give a range of values with H_{int}. Addition of Fe does not greatly change V_a, but Zr addition slightly lowers it (Figure 3.23).

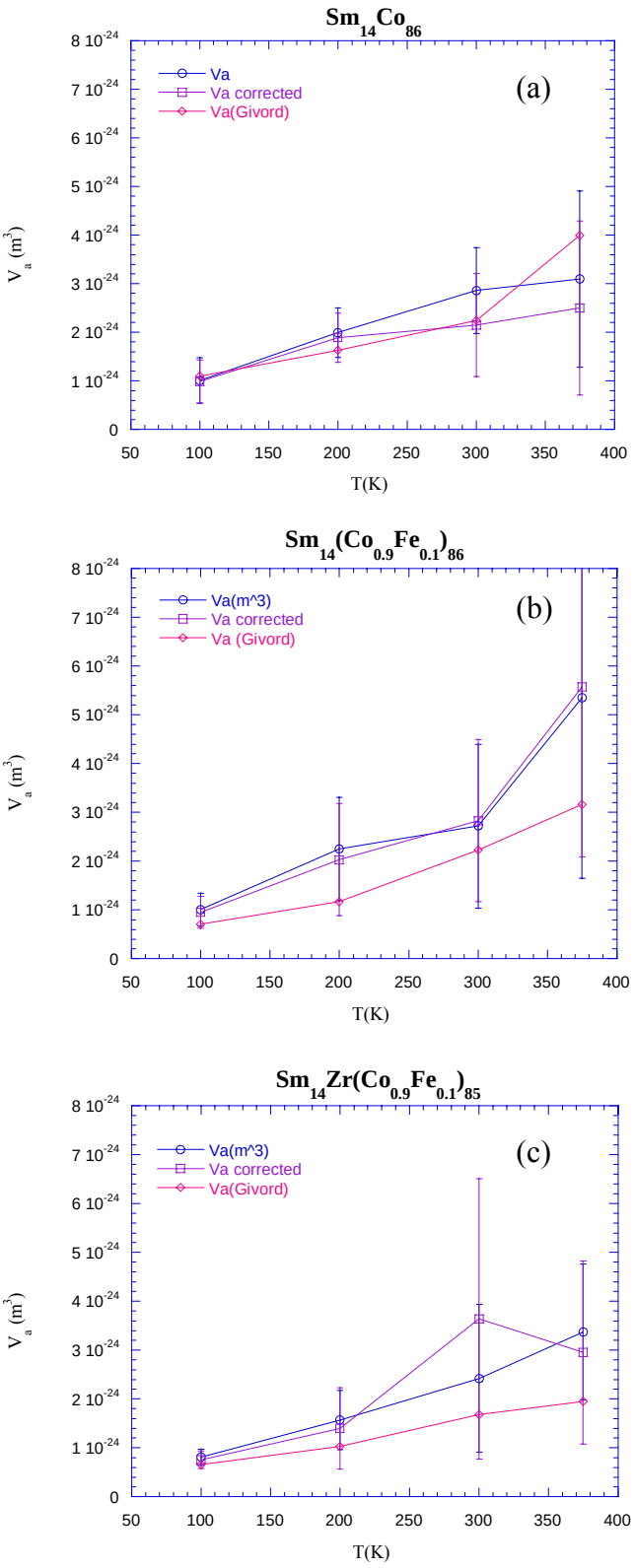

Figure 3.22. Temperature dependence of activation volume for (a) $Sm_{14}Co_{86}$, (b) $Sm_{14}(Co_{0.9}Fe_{0.1})_{86}$, and (c) $Sm_{14}Zr(Co_{0.9}Fe_{0.1})_{86}$. The Givord method of calculation of V_a does not yield significantly different results from the standard method, and correction with η is not significant.

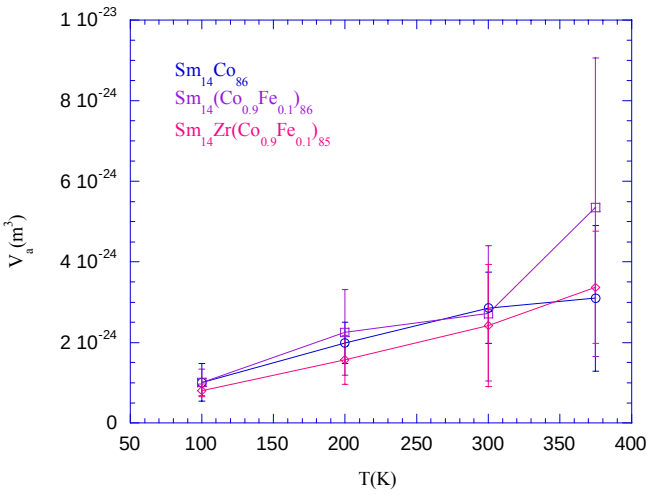

Figure 3.23. Comparison of activation volumes. Fe addition does not change V_a, while Zr slightly lowers it.

[1] Gary A. Novak and Alan A. Colville, "A practical interactive least-squares cell-parameter program using an electronic spreadsheet and a personal computer," *American Mineralogist* 74 (1989), 488-490

[2] B.D. Cullity, *Elements of X-Ray Diffraction* (Reading, Massachusettes: Addison-Wesley, 1978).

4 INTERPRETATION AND CONCLUSIONS

In the $Sm_xZr_y(Co_{1-z}Fe_z)_{100-x-y}$ materials produced by mechanical alloying, depending on composition, coercivities in the range of 1 - 2 T and energy products in the range 50 - 100 kJ/m^3 have been achieved at room temperature. These values are comparable to those achieved by others for similar materials. Chen and coworkers found a coercivity of 1 T and energy product of 88 kJ/m^3 for mechanically milled $Sm_{12}Co_{88}$ powders with a Sm_2Co_{17} structure[1]. Substitutions including Cu, Zr, and Fe could be used to increase H_c or $(BH)_{max}$, and caused a two phase microstructure of $SmCo_5$ and Sm_2Co_{17}. Wecker *et al* produced mechanically alloyed $SmCo_5$ and Sm_2Co_{17} with $\mu_0 H_c$ = 2.8 T and 0.3 T, respectively[2]. Coercivities of 1-2 T and energy products of 90-100 kJ/m3 were achieved in mechanically milled $Sm_{12.5}(Co, Zr)_{87.5}$ materials by Tang et al[3].

These results are not better than those achieved for bulk Sm-Co based magnets. Commercial Sm_2Co_{17}-type magnets can achieve coercivities in the range 2.5 – 3.5 T and energy products in the range[4] 220 – 250 kJ/m^3. However, the results are outstanding when compared with those for bulk materials of similar composition. Coercivity in bulk $Sm_{11}Co_{89}$, for example, is nearly zero[5]. The microstructure in this alloy consists mainly of the Sm_2Co_{17} phase, with no cellular nature at all. Without the cellular microstructure, there is a lack of pinning sites, and hence a low coercivity. In bulk materials it is necessary to add Cu and Zr to develop a cellular microstructure that pins domain walls to develop reasonable coercivity. While coercivity is increased, the addition of these nonmagnetic elements also decreases the remanence and hence the energy product. Here we have achieved coercivities in excess of 1 T for binary compounds, and as high as 2 T for compounds without Cu. The materials have high remanences, and so $(BH)_{max}$ is as large as 100 kJ/m^3.

The development of coercivity by ball milling of materials without Cu or Zr has recently been attributed to the reduction in particle size achieved through this processing technique[6]. Chen *et al* see an increase in coercivity as particle size is reduced from 14 μm to 1.5 μm using various techniques,

including mechanical milling (Figure 4.1). Interestingly, they have been unable to make particles less than 1 μm in size by any technique. At first, this coercivity dependence on particle size would seem to be the same effect as the 1/D dependence of coercivity on grain size illustrated by Herzer (Figure 1.20). However, it is known that each particle (μm dimensions) in mechanically alloyed/milled Sm-Co materials is composed of many grains (nm dimensions)[7]. There is no reason to believe at this time that there is a linear

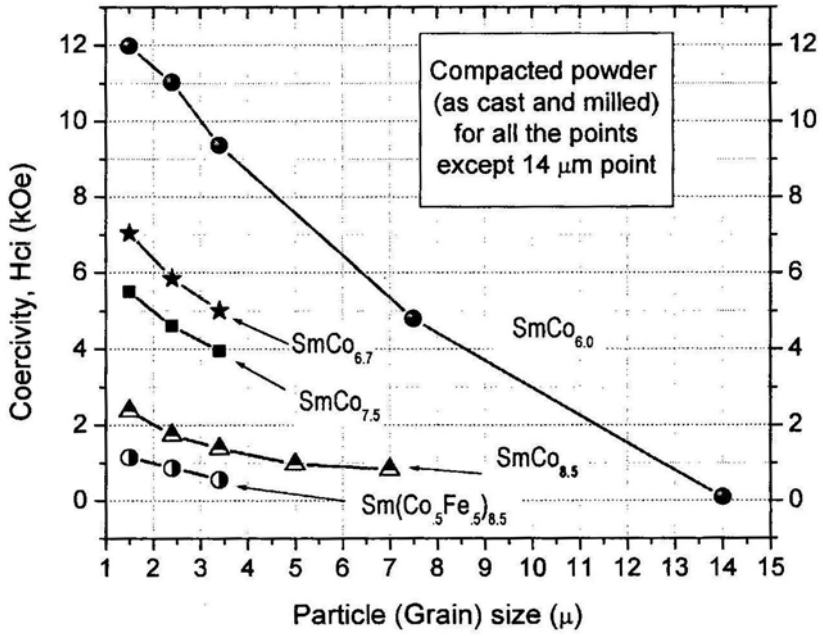

Figure 4.1. Coercivity versus particle size of Sm-Co alloys. Materials made by melting, milling, and compaction except for the 14 mm point, which was a sintered magnet after heat treatment. (After Chen *et al*, 2002)

relationship between particle size and grain size, and so it is not actually clear whether this increase in coercivity is due to a decrease in grain size as the particles size is reduced. Electron microscopy studies, utilizing both SEM and TEM are necessary to examine the relationship between particle size, grain size and coercivity.

Addition of Fe to these materials has the expected effect of increasing M_r. The increase is due to an increased amount of the $Sm_2(Co, Fe)_{17}$ phase present with increasing Fe. The coercivity is also increased for small addition of Fe, up to z = 0.1 (Figure 3.11). This is surprising since the activation

volume remains nearly the same (Figure 3.23). The decrease for higher amounts of Fe is due partly to the increased amount of the lower coercivity $Sm_2(Co, Fe)_{17}$ phase present. In addition, the narrowing of peaks in XRD patterns with Fe substitution suggests that there is an increase in the grain size of the sample (Figure 3.7). A grain size increase would also decrease the coercivity. Sherrer analysis was not used to calculate the grain size in this case, because nearly all of the peaks for the $SmCo_5$ and Sm_2Co_{17} phases overlap each other, making it difficult to determine the true peak width. Transmission electron microscopy will have to be used to determine the actual grain size.

Zr addition has the effect of increasing the coercivity in all compositions studied, but remanence and energy product are also decreased. These effects are due to both a decrease in the grain size, as indicated by increased XRD peak width, and an increase in the amount of $SmCo_5$ phase present. It is surprising that Zr stabilizes the $SmCo_5$ phase, because it is commonly accepted that Zr addition to bulk precipitation hardened Sm_2Co_{17}-type magnets stabilizes the hexagonal Sm_2Co_{17} lamella phase[8].

It is interesting to note that increased Zr content has the same effect on the magnetic properties as increased Sm content. With more Sm, the coercivity increases, while the remanence and energy product decrease (Figure 3.12, Table 3.1). The same holds true for increased Zr content. This points towards a question that is still the subject of debate: which lattice site does the Zr occupy? From the lattice parameters, it appears that Zr goes into both the $SmCo_5$ and the Sm_2Co_{17} phases, but it is difficult to tell whether it replaces Sm or the transition metal. The atomic radius of Zr, at 160 pm, is more similar to that of Sm (180 pm) than Co (125 pm), which suggests that Zr might subsitute into the rare earth site more easily than the transition metal site. It has recently been demonstrated that Zr occupies the rare earth site when substituted into the $Nd_2Fe_{14}B$ system[9]. These results suggest that Zr may also occupy the RE site in this case. In any event, it is useful to know that through Zr addition, the amount of (expensive) rare earth in these materials can be reduced.

At room temperature, all compositions exhibit smooth demagnetization curves with enhanced remanence. The remanence ratio σ_r/σ_s is greater than 0.6

in most compositions. This indicates the existence of exchange interactions among the fine grains. At high temperature, the formerly smooth demagnetization curves become that of a two-phase mixture. At 400ºC, σ(1.4T) is larger than it had been at 200ºC and 300ºC, and the loop crosses over itself as it returns to the maximum positive field. This suggests that the sample is undergoing some irreversible change as it is held at high temperature for the duration of the measurement, which is approximately 30 minutes. The final loop taken at 200ºC confirms this.

There are two suggestions for what this irreversible change could be. First, the two-phase nature of the demagnetization curves at high temperature suggests grain growth in the sample. However, an increase in σ(1.4T) would not be expected with an increase in grain size. Consequently, the second suggestion is that the sample undergoes phase segregation, nucleating a softer Co-rich phase. A further clue to the identity of a possible phase change is found in the high temperature hysteresis loops for compositions without Zr. In these compositions, the demagnetization curves are smoother than those of Zr-containing alloys, and the increase in σ(1.4T) is much smaller. In addition, there is not as great a difference between the loops taken at 200ºC. X-ray diffraction on a Zr-substituted sample annealed at 400ºC for 30 min under Ar offers little insight. The peaks are only very slightly narrower. In addition, there is the slight suggestion of the presence of the cubic Zr_6Co_{23} phase, but it is difficult to resolve because the lines for the phase overlap with those for the $SmCo_5$ and Sm_2Co_{17} phases. It is most likely that both a phase change, involving the nucleation of a Co-Zr phase, and grain growth are occurring at temperatures greater than 300ºC in these materials.

The β(20-300) value of –0.21 %/ºC for $Sm_{13}(Co_{0.9}Fe_{0.1})_{87}$ is lower than that of –0.30 %/ºC typically observed in Sm_2Co_{17}-type magnets, but the room temperature coercivity is low at only 1.2 T. The Zr-substituted alloys have much better room temperature coercivity, but to make them suitable for high temperature applications the problems of phase change and possible grain growth must be addressed. Optimization of the annealing procedure to improve high temperature properties could eliminate the grain growth problem, but at the cost of room temperature coercivity. It has been shown[10]

that small additions of B to mechanically milled $Sm(Co,Ti)_7$ can improve high temperature loops from that characteristic of a two phase mixture to smooth, single-phase type loops. Such addition probably causes the formation of a ZrB_2 grain boundary phase that inhibits grain growth. A similar addition to these $Sm_zZr_y(Co_{0.9}Fe_{0.1})_{100-z-y}$ mechanically alloyed materials could have a similar effect. Unfortunately, addition of B in the $Sm(Co,Ti)_7$ alloys leads to a decrease in room temperature coercivity without change in β. It may be useful to study the B substitution on the high temperature stability in the $Sm_zZr_y(Co_{0.9}Fe_{0.1})_{100-z-y}$ alloys, but if the boron significantly affects the room temperature coercivity without improving β, then these alloys would still not be good candidates for high temperature applications.

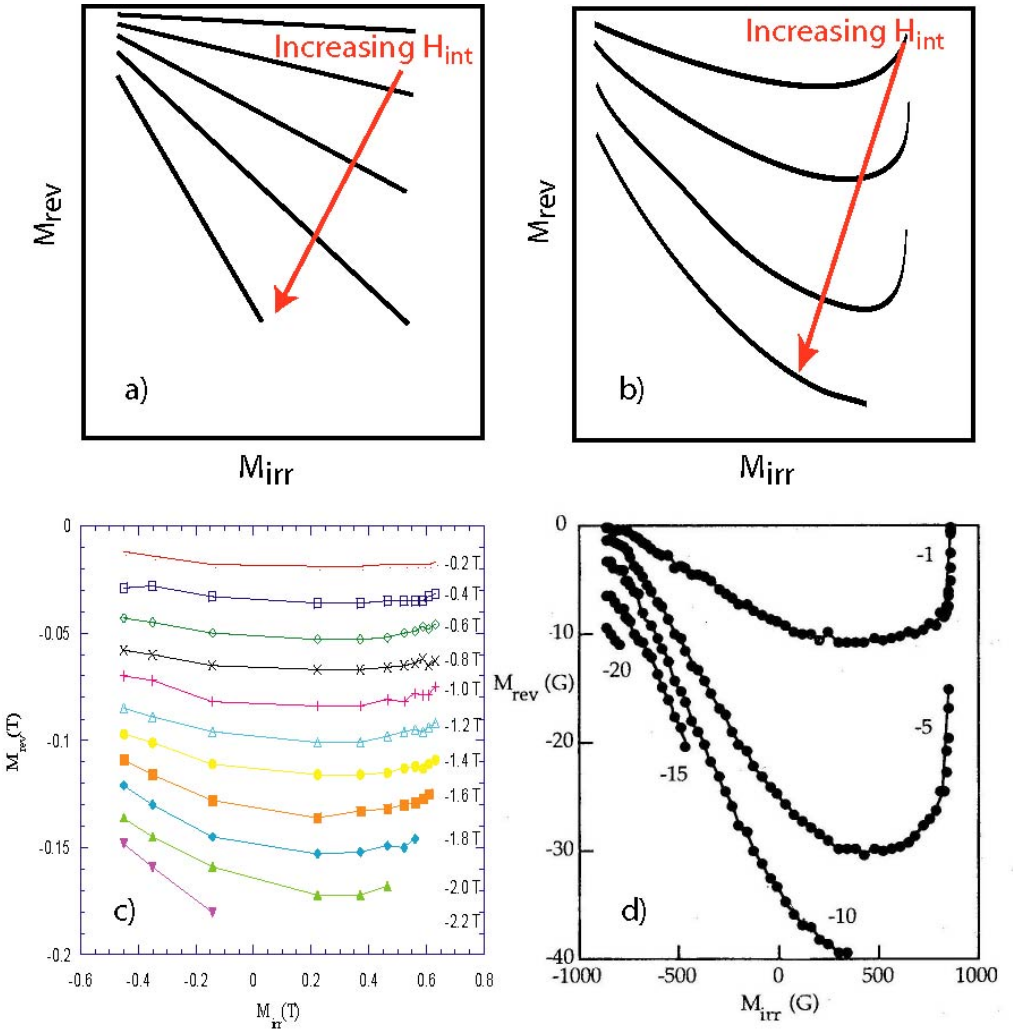

Figure 4.2. M_{rev} vs. M_{irr} curves. a) Illustration of prediction for coherent rotation. b) Illustration of prediction for domain wall bowing. c) experimental results from this study for $Sm_{14}Zr(Co_{0.9}Fe_{0.1})_{85}$ at 200 K at constant internal field, as indicated at right d) Results for commercial $Sm_2(Co, Fe, Cu, Zr)_{17}$ at room temperature for a selection of internal fields as indicated, obtained by Crew *et al*; note the difference in scale (1000 G = 0.1 T)

Recoil and magnetic viscosity measurements suggest that there is little pinning type behavior in these materials. The first clue comes from the initial magnetization curves, which are of mixed type, suggesting nonuniform pinning . Examination of M_{rev} vs M_{irr} curves shows a behavior that is somewhere in between that expected for nucleation controlled and pinning controlled behavior. Figure 4.2 a) and b) illustrate the behavior that is expected for the situations where the easy axes reverse by coherent rotation and rotation of domain magnetization by domain wall bowing respectively. In the case of coherent rotation, at constant field M_{rev} is a linear function of M_{irr}, with a negative gradient that increases with increasing field magnitude[11]. In the case of magnetization reversal by domain wall bowing (e.g. due to pinning), M_{rev} vs. M_{irr} curves are no longer monotonic. The curves now exhibit a minimum. This is further demonstrated in Figure 4.2 d), which shows experimental results obtain by Crew and coworkers for a commercial Sm_2(Co, Fe, Cu, Zr)$_{17}$ magnet, which is known to reverse by a pinning controlled mechanism. The curves decrease from the left with a steep slope, go through a minimum and then increase again with an even steeper slope. This is in sharp contrast to the M_{rev} vs. M_{irr} curves obtain in this study, which have only a slight bend. From this difference it can be deduced that the ball-milled Sm-Co materials do not have a pinning-controlled mechanism like that of bulk Sm-Co. The fact that the curves do bend slightly suggests that there are still some pinning sites. These sites are most likely the grain boundaries between the $SmCo_5$ and Sm_2Co_{17} phases. Those grain boundaries would not be strong pinning sites, because without the presence of Cu in the $SmCo_5$ phase, the two phases are magnetically very similar.

The other interesting difference between Crew and coworker's results for commercial Sm_2(Co, Cu, Fe, Zr)$_{17}$ and our results for mechanically alloyed $Sm_xZr_y(Co_{1-z}Fe_z)_{100-x-y}$ is in the reversal of the phases. Crew *et al* observe a double peak in the magnetic viscosity parameter with field (Figure 4.3(a)). The double peak is associated with two different pinning sites. This is in agreement with calculations by Katter, that show there are two different pinning sites with pinning fields that differ by a factor of two in Sm_2(Co, Cu, Fe, Zr)$_{17}$ magnets[12]. The model Katter uses assumes that the domain walls are

pinned at two different sites: in low fields at the edges of the 2:17 cells, and in higher fields at the intersection of the Z phase and the Cu-rich (1:5) boundary phase. In the mechanically alloyed materials, the two phases are reversing together, as shown by the sharp peaks in χ_{tot} (Figure 3.20) and the single peak in curves of S vs. H_{int} (Figure 4.3). This points to a strong coupling between the two phases.

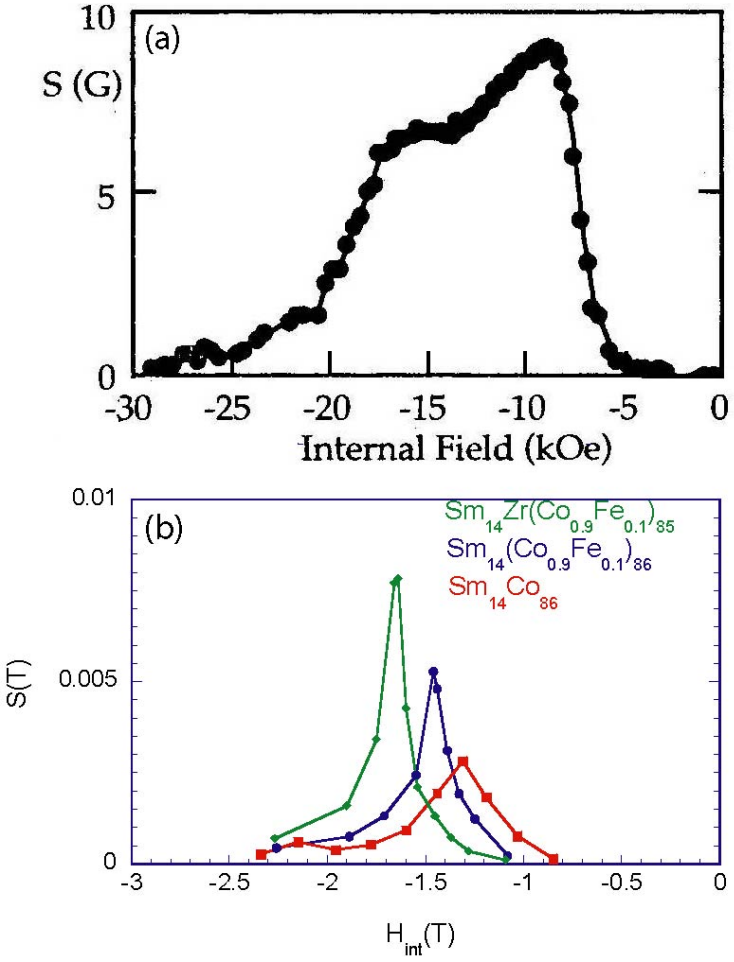

Figure 4.3. Plots of magnetic viscosity parameter S with internal field Hint at room temperature: (a) Crew *et al*'s results for $Sm_2(Co, Fe, Cu, Zr)_{17}$ precipitation hardened magnet, and (b) results from this study for mechanically alloyed $Sm_xZr_y(Co_{0.9}Fe_{0.1})_{100-x-y}$.

The activation volume in mechanically alloyed $Sm_xZr_y(Co_{1-z}Fe_z)_{100-x-y}$ materials is about 5 times larger than that for commercial Sm_2Co_{17}-type magnets. Figure 4.4 shows a comparison of results for the mechanically alloyed materials with those obtained by Dr. I. Panagiotopoulos for commercial $Sm_2(Co, Cu, Fe,Zr)_{17}$ grades and presented at the meeting of the HITEMAG project on 22 March 2002. The mechanically alloyed materials

reverse mainly by a nucleation controlled mechanism, and hence the activation volume in these materials corresponds to the formation of a nucleus of reversed magnetization and so is related to the domain wall width. Taking the cube root of the activation volume for the mechanically alloyed materials gives an activation length of 10 – 15 nm. This length is very similar to the $Sm_2(Co, Fe)_{17}$ domain wall width of approximately 10 nm, while it is 3 or 4 times the domain width of $SmCo_5$ of 3.4 nm. This suggests that reversal is initiated in the Sm_2Co_{17} phase. In contrast, in the 2:17-type materials, the activation volume is related to pinning and depinning of domain walls[13]. The domain walls are pinned in the $SmCo_5$ phase in these magnets, and as such the activation volume is related to the domain wall width of the $SmCo_5$ phase. This explains why the mechanically alloyed materials have a larger activation volume than the precipitation hardened materials. The activation volume in both types of material increases with temperature because of the decrease in anisotropy with temperature.

In summary, $Sm_xZr_y(Co_{1-z}Fe_z)_{100-x-y}$ produced in this study by

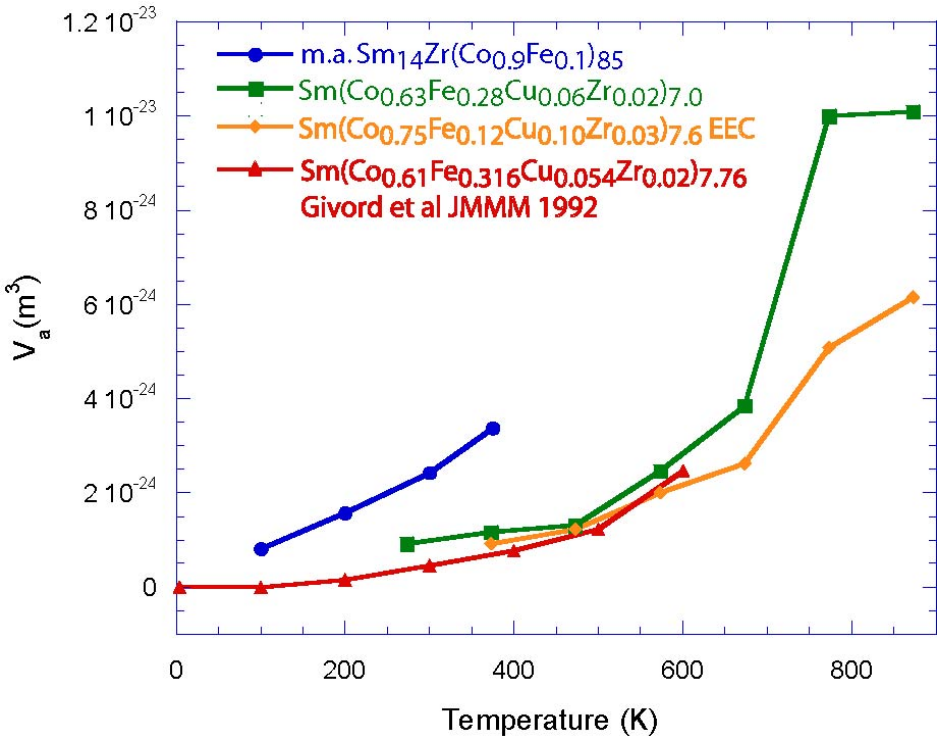

Figure 4.4. Comparison of activation volumes for material from this study, mechanically alloyed $Sm_{14}Zr(Co_{0.9}Fe_{0.1})_{85}$, and commercial grades of $Sm_2(Co, Cu, Fe, Zr)_{17}$ magnets, including one from Electron Energy Corporation (EEC).

mechanical alloying had similar properties to other mechanically alloyed/milled Sm-Co based materials. The properties were not as good as those obtained for precipitation hardened materials, but they are a great improvement on the properties of Cu-free bulk materials. The improvement in coercivity is due to the reduction in particle size due to milling. X-ray diffraction showed that all samples contain a mixture of $SmCo_5$ and Sm_2Co_{17} phases. Fe addition favored Sm_2Co_{17} phase formation and hence increased remanence. Surprisingly, Zr addition favored formation of $SmCo_5$, leading to increased coercivity. At room temperature and below, demagnetization curves are smooth and χ_{tot} exhibits a sharp peak at the coercivity, indicating strong coupling between the two phases. At high temperature this coupling breaks down as the materials go through a phase change and grain growth at temperatures greater than 300ºC. These changes make the materials unsuitable for high temperature use. Measurement of recoil and magnetic viscosity show that these materials reverse by a nucleation controlled process, although there may be a few pinning sites. As a result, the activation volume is larger in these materials than in bulk precipitation hardened Sm-Co materials.

---

[1] Chen, Z., X. Meng-Burany, H. Okumura, and G.C. Hadjipanayis, "Magnetic Properties and Microstructure of Mechanically Milled $Sm_2(Co,M)_{17}$-based powders with M=Zr, Hf, Nb, V, Ti, Cr, Cu, and Fe," *Journal of Applied Physics* 87, no. 7 (2000), 3409-3414.

[2] Wecker, J., M. Katter, and L. Schultz, "Mechanically Alloyed Sm-Co Materials," *Journal of Applied Physics* 69, no. 8 (1991), 6058-6060.

[3] Tang, H., Y. Liu, and D.J. Sellmyer, "Nanocrystalline $Sm_{12.5}(Co, Zr)_{87.5}$ Magnets: Synthesis and Magnetic Properties," *Journal of Magnetism and Magnetic Materials* 241 no. 2-3 (2002) 345-356.

[4] Marlin S. Walmer, and Christina H. Chen, "A New Class of Sm-TM Magnets for Operating Temperatures Up to 550°C," *IEEE Transactions on Magnetics* 36, no. 5 (2000), 3376-3381

[5] Tang, W., Y. Zhang, A.M. Gabay, H. Kronmuller, and G.C. Hadjipanayis, "Effect of Compositions and Processing on the Microstructure and Magnetic Properties of $Sm(Co_{bal}Fe_vCu_yZr_x)_z$ Magnets," *Proceedings of the Seventeenth International Workshop on Rare Earth Magnets and Their Applications* (Newark, DE, 2002), 685-695.

[6] Zeng, Q., S. Wang, Y. Zhang, E.V. Belozerov, and G.C. Hadjipanayis, "Effect of Particle Size on the Coercivity of Rare Earth Magnets Prepared by Ball Milling," *Proceedings of the Seventeenth International Workshop on Rare Earth Magnets and Their Applications* (Newark, DE, 2002), 983-989; and Chen, C.H., S. Kodat, M.H. Walmer, S.-F. Cheng, M.A. Willard, and V.G. Harris, "Magnetic and Structural Properties of $Sm(Co_{1-x}Fe_x)_z$ Based Powders and Spin Cast Ribbons," *Proceedings of the Seventeenth International Workshop on Rare Earth Magnets and Their Applications* (Newark, DE, 2002),844-852.

[7] Chen, Z., *et al*, (2000) 3411; and Chen, S.K., J.L. Tsai, and T.S. Chin, "Coercivity and Transmission Electron Microscopy Study of Nanocomposite Sm-Co Powders by Mechanical Alloying," *Journal of Applied Physics* 81, no. 8 (1997), 5631-5633.

[8] Y. Zhang, W. Tang, and G.C. Hadjipanayis, "Effect of Zr on the Microstructure, Magnetic Domain Structure, Microchemistry and Magnetic Properties in Sm(Cobal,Cu0.088, Fe0.01, Zrx)8.5 Magnets," *Proceedings of the Seventeenth International Workshop on Rare Earth Magnets and Their Applications* (Newark, DE, 2002), 975-982.

[9] Bao-Min Ma *et al*, "Effect of Zr substitution for Rare Earth in $R_2Fe_{14}B$," Intermag 2002 Conference, in press

[10] Rhen, F.M.F., and I.R. Harris, unpublished.

[11] Crew, D.C., R.C. Woodward, and R. Street, "Reversible Magnetization Behavior in $Sm_2(Co,Fe,Cu,Zr)_{17}$," Journal of Applied Physics 85, no. 8 (1999), 5675-5677.

[12] M. Katter, "Coercivity calculation of $Sm_2(Co,Fe,Cu,Zr)_{17}$ magnets," *Journal of Applied Physics* 83 no.11 (1998), 6721-6723.

[13] D. Givord and M.F. Rossignol, "Coercivity" in J.M.D. Coey, ed. *Rare-Earth Iron Permanent Magnets* (Oxford:Clarendon Press, 1996), 225.

5 FUTURE WORK

5.1 TRANSMISSION ELECTRON MICROSCOPY

There is a serious need for microstructural analysis to complete this study. In materials science, there is a very strong interrelationship between the microstructure and properties of materials. At this point, it is difficult to definitively conclude the study of these materials without actually seeing what the microstructure looks like, and what the grain size is. For example, it is suggested by the magnetic and x-ray data that these materials do not have a precipitation hardened cellular microstructure, but instead a fine mixture of $SmCo_5$ and Sm_2Co_{17} nanoscale grains. The high coercivity could be attributed to nanometer-sized grains, but this still needs to be confirmed.

Microstructural analysis should be carried out using transmission electron microscopy (TEM). This may show how the two types of grains are arranged in the materials, and measure grain size. Effects, if any, of annealing time and alloying addition on the grain sizes could be determined. Also, TEM data on grain size can be used in conjunction with SEM data on particle size to see if there is a linear relationship between particles size and grain size. Finally, Lorentz microscopy could be used to study domain structures in the materials. It will be interesting to see if the domains are smaller or larger than grains (interaction domains), or even particles, and to try to determine what the few pinning sites suggested by magnetization reversal data are.

The major obstacle to performing TEM at the moment is the particle size of the materials. The average particle size of about 9 μm means that most of the particles are too large for an electron beam to pass through. Generally, for 50-200 kV microscopes, thicknesses around 200-400 nm are desirable, while thicknesses of tens of nanometers are necessary for higher resolution work[1]. Usually samples for TEM are thinned using mechanical thinning, chemical thinning, or ion beam thinning, but these techniques cannot be used on these fine powders. Preparation of fine powder samples for TEM is not a new problem, and several solutions have been developed. The first solution is to suspend the particles in methanol and then place the mixture in an ultrasonic

bath to break up agglomerates. When the solution settles for a few minutes after ultrasonication, the smallest particles migrate to the top of the solution where they can be caught on a standard carbon grid[2]. The problem with this method is that it only allows the smallest particles to be examined, and these may or may not be a good representation of the rest of the sample. Other methods include mixing the powders in an epoxy and then placing the mixture in a copper tube[3]. The tube supports the mixture for further slicing and thinning operations. This leads to the suggestion that the materials could be pressed with a soft metal, such as Cu or Zn, making a composite that could be sliced and thinned using conventional techniques. Another variation on the epoxy technique is to use a low viscosity, slow curing epoxy that is mixed with the powders and then placed in a small plastic tube. The tube is then centrifuged, with the objective of compacting the particles into a minimal amount of epoxy matrix. The centrifuged sample is then cured for a few days and finally sliced and ion milled for the TEM investigation[4]. Any of the techniques with epoxy or metal bonders could be used to good effect to get a good cross section of the sample.

After sample preparation it is still difficult to actually look at magnetic particles in a TEM. This is because the powders are attracted to the lenses in the TEM, which are magnetic. There are many anecdotes among the magnetism community of magnetic particles getting sucked out of the epoxy and into the column. This not only leaves the investigator with no sample to look at, but it also is detrimental to the lenses. One solution to this problem is to use a TEM that is equipped with post-column magnification, so the objective lens can be turned off during the investigation[5].

5.2 EXAFS

The role of Zr in rare earth permanent magnets is still an unresolved question. Zr is used universally as a substitution to inhibit grain growth and hence increase coercivity. It's effects on the magnetic properties are quite well known, but the crystallography of Zr substitution is not well understood. What site in the Sm-Co lattice does Zr occupy? It could go to a transition metal site. However, the fact that an increase in Zr content usually has the

same effect on the magnetic properties as an increase in rare earth suggests that maybe Zr occupies the RE site. Reinforcing this argument is the fact that the atomic radius of Zr is more similar to that of Sm than that of Co. Ma has recently stated that Zr goes to the Nd site in $Nd_2Fe_{14}B$[6]. Perhaps the same holds true for $SmCo_5$ and/or Sm_2Co_{17}.

A specialized technique that takes advantage of the relatively new, high intensity synchrotron radiation sources could solve this problem. Extended X-ray Absorption Fine Structure (EXAFS) is a technique that uses high intensity white radiation to probe the symmetry of the local environment around a selected atom. When an X-ray photon matches with the binding energy of the core electron of the selected atom, the energy of the photon can be transferred to this core electron. This yields a photoelectron of variable kinetic energy, and hence variable wavelength. This electron wave is part scattered by neighbors of the excited atom and interference at the source atom between outgoing and incoming waves results in oscillation in the final state, and hence in the absorption coefficient. Through careful manipulation of EXAFS oscillations data, a spectroscopist can extract information about the coordination number and the distances of the neighbors[7].

An EXAFS experiment to determine which site the Zr occupies will be be performed using a single phase Sm-Co-Zr material. This material can have either the Sm_2Co_{17} or the $SmCo_5$ structure. The material will be melted in the arc melter and then subjected to a solutionizing heat treatment, with the object of obtaining a single phase material for the experiment. The EXAFS experiment will be performed by Dr. Bruce Ravel of the US Naval Research Laboratories, an expert in the field. If the Zr does indeed occupy the Sm site in these materials, The EXAFS oscillations should show that the Zr is surrounded by a ring of 6 Co atoms, as shown in Figures 1.11 and 1.12. The other case, where Zr occupies a transition metal site, is more complicated. In one transition metal site, the Zr atom would be surrounded only by Co atoms, while in the other it would be surrounded by a mixture of Co and Sm atoms.

5.3 MAGNETIC MELT SPINNING

5.3.1 Motivation

The materials produced in this study are all isotropic. The c-axes (easy magnetization axis) of the grains are randomly oriented. One way to improve the properties of a hard magnetic material is to produce an anisotropic material, i.e. a material where all the c-axes are aligned. This leads to an increased remanence, and hence increased energy product.

Legrand *et al* have recently shown that Sm-Co materials can be textured by solidification in a magnetic field[8]. They found that binary and commercial compositions of $SmCo_5$ and Sm_2Co_{17} magnets all solidified with their c-axes aligned along the applied field direction, regardless of composition. In the case of $Sm(Co,Cu,Fe,Zr)_z$ materials, they had an average misalignment of only 15 % and improved magnetic properties. The drawback to this process is that it requires a minimum field of 2.5 T.

Yan and coworkers have also recently demonstrated crystal texturing of

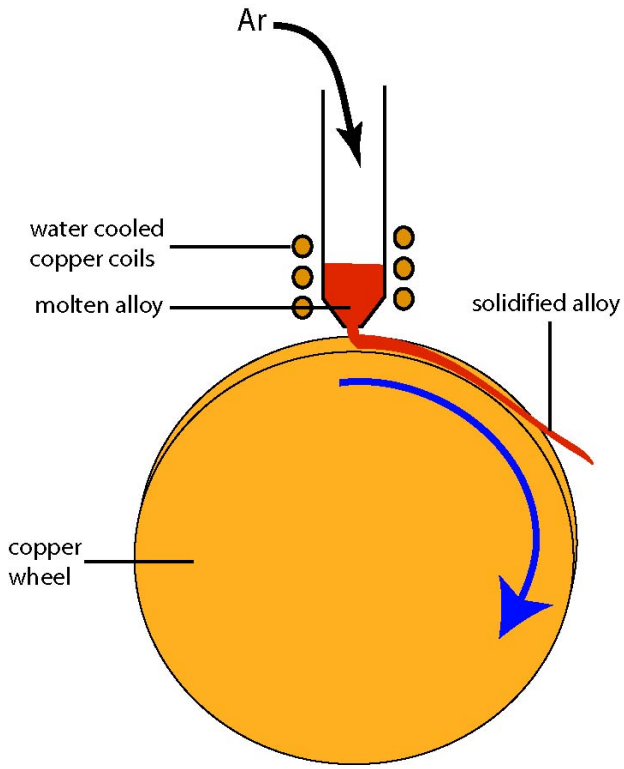

Figure 5.1. Schematic of melt spinning. An alloy is melted by induction and then an overpressure of Ar gas is applied to eject the metal onto spinning wheel. The alloy solidifies on the wheel at a rate of up to 10^6 K/s, producing amorphous or nanocrystalline ribbons, often with metastable phases present.

magnetically hard rare earth based materials[9]. Yan achieved this by melt spinning the materials at a slow wheel speed of approximately 5 m/s. Melt spinning is a rapid solidification technique where a molten alloy is ejected onto the surface of a spinning wheel (Figure 5.1). Typically, melt spun materials are produced at speeds of 25-50 m/s, resulting in amorphous ribbons which are then annealed to achieve the desired microstructure. This approach provides a microstructure having isotropic oriented grains. When the materials are melt-spun at slow speeds they undergo directional solidification in the thermal gradient. In the case of hexagonal Sm-Co materials, the c-axis (the magnetic easy axis) lies in the longitudinal ribbon direction, with an average deviation of 27º. Addition of Gd improves this texture[10], reducing the average deviation to 21.5º, while addition of C causes the texture to change so the c-axis is normal to the plane[11]. For tetragonal Nd/Pr-Fe-B materials melt spun at slow speeds, the c-axis (easy axis) lies normal to the ribbon surface[12].

Both techniques achieve reasonable good texture. But, can this be

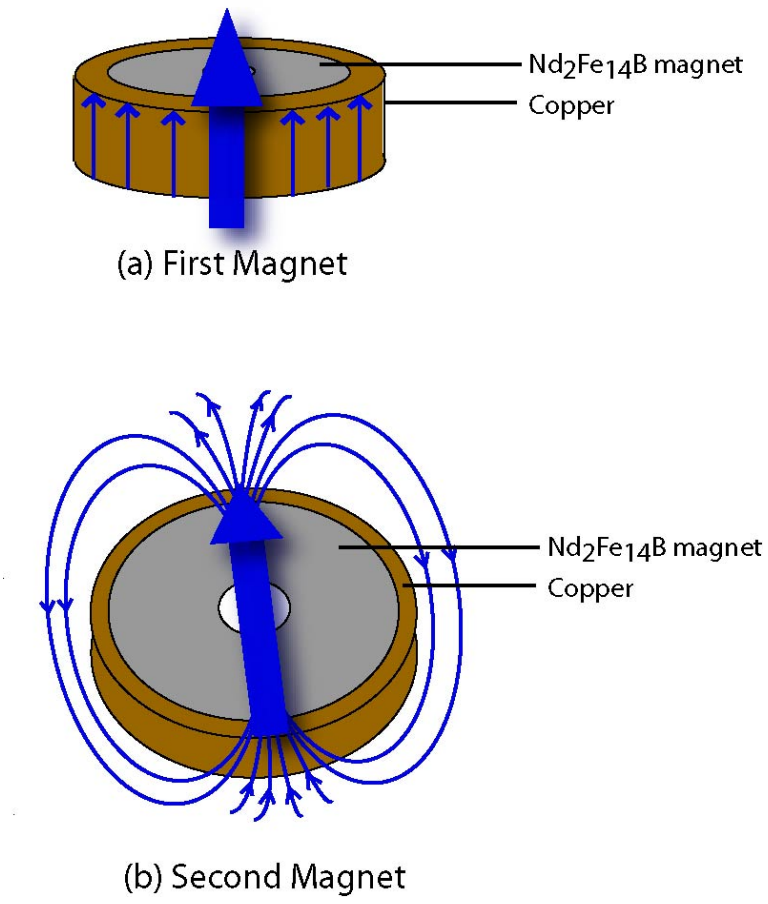

Figure 5.2. Schematic of magnetic wheels for magnetic melt spinning

improved upon? The objective of this work would be to combine the two techniques to produce even more strongly anisotropic materials, and so improve the remanence again. To do this, a magnetic wheel has been designed for an existing melt spinner at TCD. Preliminary tests of melt spinning Sm-Co materials at slow speed onto the magnetic wheel have been performed.

5.3.2 Preliminary Results

New wheels were produced for the existing melt spinning apparatus at TCD. The wheels consisted of a $Nd_2Fe_{14}B$ magnet covered with a 3 mm Cu sheath. Two wheels were magnetized as shown in Figure 5.2, with a maximum measured field of 400 mT at the Cu surface. Measured field profiles for both wheels are tabulated in Appendix C. The first magnetic wheel proved

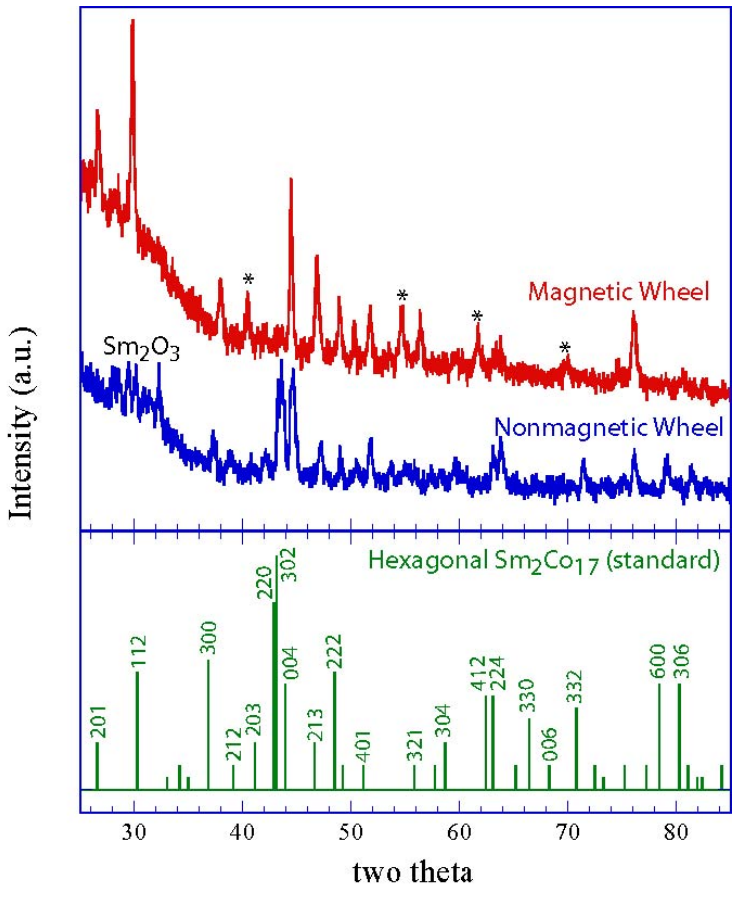

Figure 5.3. (top) XRD patterns for Sm-Co materials melt spun at 4 m/s onto magnetic and non-magnetic wheels. (bottom) Standard pattern (from International Centre for Diffraction Data) for untextured hexagonal Sm_2Co_{17}. Experimental results appear to correspond to textured Sm_2Co_{17}. Peaks in the experimental data that do not correspond to the hexagonal Sm_2Co_{17} standard shown, but do correspond to rhombohedral Sm_2Co_{17} are marked with an asterix (*).Additional peaks around $2\theta = 30^o$ correspond to Sm_2O_3, while all peaks at higher angles correspond to either hexagonal or rhombohedral Sm_2Co_{17}.

impossible to use without redesigning the melt spinner to reduce magnetic forces in the chamber. Consequently, only the second magnetic wheel was used for this first attempt. The $Nd_2Fe_{14}B$ insert for a third wheel was thermally demagnetized before use. Samples of $SmCo_5$ + 10 wt% Sm were prepared using an arc melter prior to melt spinning. The samples were then melt spun under 1 mbar of Ar using an overpressure of 1 bar to eject the molten alloy onto the wheel spinning at 4 m/s. The same process was used with both the nonmagnetic wheel and the nonmagnetic wheel. Ribbons obtained from the melt spinner were annealed under vacuum for 1 hour at 800ºC and then quenched to room temperature.

Figure 5.3 shows XRD patterns for the melt spun and annealed materials. The samples from both wheels exhibit patterns that are characteristic of textured Sm_2Co_{17}. In the sample produced on the non-magnetic wheel, the (004) peak is the same size as the (302) peak. In an isotropic sample, the latter would be much the largest peak. In the pattern for the sample produced on the magnetic wheel, the (303) peak is completely absent. In both materials there is a slight suggestion of the presence of Sm_2O_3. Hysteresis loops for the two materials are shown in Figure 5.4.The magnetization for the sample produced on the magnetic wheel is twice that of the sample produced on the nonmagnetic wheel.

From these results, it appears that melt spinning onto a magnetic wheel may slightly improve texture. However, these results are only preliminary. More work needs to be done first of all to eliminate oxygen from the system, and the process needs to be tested to be sure this is actually a real effect. It appears that the effect is small, but it would be interesting to see if texturing can be achieved at higher wheel speeds when using a magnetic wheel. This is because smaller grain size is achieved at higher speeds (and hence higher quench rates) when melt spinning. The combination of small grains and a high degree of orientation of those grains should lead to high coercivity and improved remanence, yielding a higher energy product.

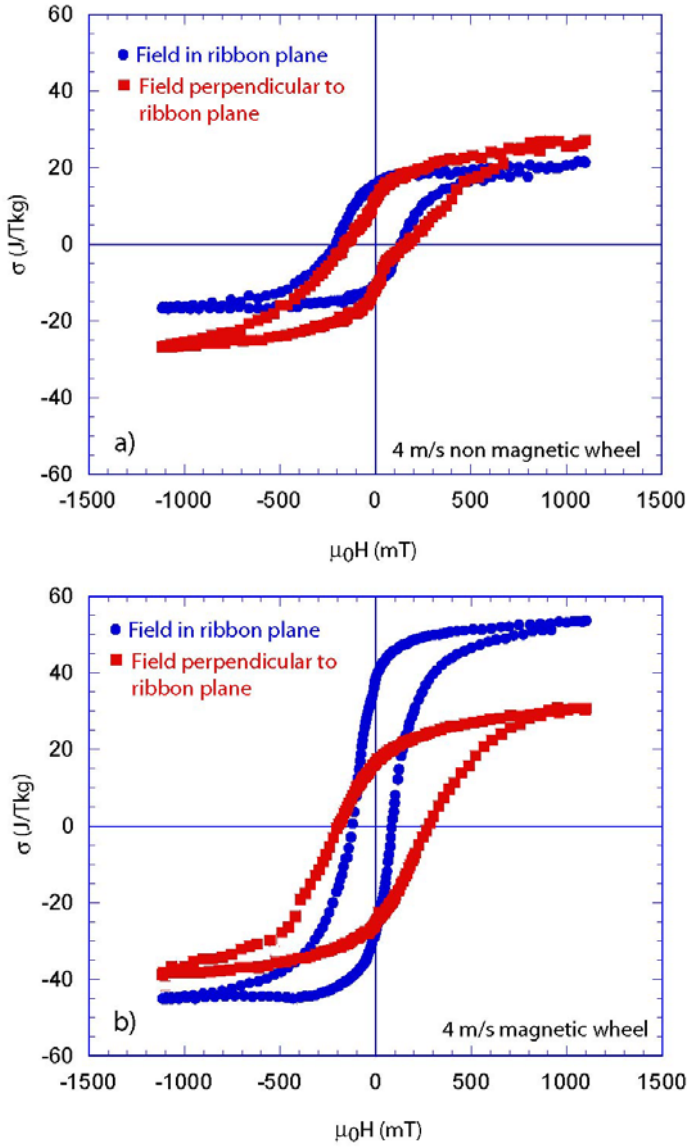

Figure 5.4. Hysteresis loops for melt spun samples. a) Sample spun at 4 m/s onto nonmagnetic wheel. b) Samples spun at 4 m/s onto magnetic wheel.

[1] M. De Graef, *Introduction to Electron Microscopy* (Carnegie Mellon University, course notes, 1997), 35.

[2] K. O'Donnell, Remanence Enhancement in Two-Phase Nanostructures Prepared by Mechanical Alloying (Trinity College Dublin, Ph.D. thesis, 1996), 60.

[3] P.A.I. Smith, personal communication 2002.

[4] A.E. Berkowitz, M.F. Hansen, K.S. Vecchio, F.T. Parker, H. Harper, and F.E. Spada, "Exchange-Spring Magnets Produced by Spark Erosion," *Proceedings of the Seventeenth International Workshop on Rare Earth Magnets and Their Applications* (Newark, DE, 2002), 749-759.

[5] M. DeGraef, personal communication.

[6] Bao-Min Ma *et al*, "Effect of Zr substitution for Rare Earth in $R_2Fe_{14}B$," Intermag 2002 Conference, in press

[7] A. Fontaine, "Interaction of X-rays with Matter: X-ray Absorption Spectroscopy," *Theory, Instruments, and Methods*, vol. 1 of *Neutron and Synchrotron Radiation for Condensed Matter Studies* (Paris: Springer-Verlag, 1993), 325.

[8] B.A. Legrand, D. Chateigner, R. Perrier de la Bathie, R. Tournier, "Orientation by solidification in a magnetic field A new processes to texture SmCo compounds used as permanent magnets," *Journal of Magnetism and Magnetic Materials* 173 (1997) 20-28.

[9] A-R. Yan, W-Y. Zhang, H-W. Zhang, and B. Shen., "Melt spun magnetically anisotropic $SmCo_5$ ribbons with high permanent performance," *Journal of Magnetism and Magnetic Materials* 210 no. 1-3 (200)10-14.

[10] W-Y. Zhang, A-R. Yan, H-W. Zhang, S-Y Zhang, and B-G. Shen., " Effect of the substitution of Gd for Sm on magnetic anisotropy of melt-spun $Sm_{1-x}Gd_xCo_5$ ribbons," *Journal of Physics D – Applied Physics* 34 no. 7 (2001)1065-1068.

[11] A-R. Yan, Z-G. Sun, W-Y Zhang, H-W. Zhang, and B-G. Shen, " Magnetic properties, domain structure, and microstructure of anisotropic $SmCo_{6.5}Zr_{0.5}$ ribbons with C addition," *Journal of Materials Research* 16 no.3 (2001) 629-632.

[12] R. Coehoorn and J. Duchateau, " Preferential crystallite orientation in melt spun Nd-Fe-B permanent magnet materials," *Materials Science and Engineering* 99 (1988)131-135; and C.R. Paik, M. Okada, and M. Homma, "Magnetic properties of anisotropic Pr-Fe-B melt-spun ribbons," *IEEE Translation Journal on Magnetics in Japan* 7 no. 1 (1992) 57-63.

A APPENDIX : IS GADOLINIUM FERROMAGNETIC?

My first project at Trinity focused on an investigation of the spin structure of pure Gadolinium (Gd). In this work, behavior unexpected for a ferromagnet was found in the AC Susceptibility traces with temperature. What follows here is the text of the paper "AC susceptibility of a gadolinium crystal," published in *Journal of Applied Physics* **87** (pp. 7028-30) and presented at the joint MMM/Intermag meeting in San Antonio, January 2000. Details of this work can also be found elsewhere[1].

A.1 INTRODUCTION

Gadolinium, together with iron, cobalt and nickel, is one of four elements which may be ferromagnetic at room temperature; its Curie point T_C is just 293 K. The following heavy rare earths (Tb, Dy Ho) first order in a helical antiferromagnetic structure before settling into a ferromagnetic state at lower temperature[2], the width of helical region varying from 8 K in Tb to 112 K in Ho. These incommensurate helical structures correspond to a minimum in the spin-wave energy and a maximum in the exchange integral J(q) at a nonzero value q_m which decreases in the sequence Ho, Dy, Tb. Extrapolating these data to gadolinium suggests that a similar long wavelength modulation might occur just below T_C.

There were proposals in the 1960s[3] that a helical spin structure similar to that observed in other heavy rare earths also occurred in Gd, but that small fields (up to 1.2 kA/m applied in the 210 - 293 K region) were sufficient to transform the spiral into a collinear ferromagnetic structure. However, this idea was discounted on the basis of neutron diffraction measurements on a crystal[4]; it was deduced from the width of the magnetic reflections below T_C that the turn angle would be smaller than 2°. It is now generally accepted that Gd is the only simple ferromagnet among the rare earths, with magnetic moments lying along the hexagonal c-axis between the Curie temperature, T_C, and the spin reorientation temperature, T_{sr}. Below T_{sr} = 225 K they are

inclined at an angle θ to c, with a maximum value of θ of about 65° occurring at 180 K.

The temperature dependence of the anisotropy constants has been studied by several authors[5]. The second anisotropy constant K_2 and the basal plane anisotropy K_3' are always positive. A change of sign of the first single-ion anisotropy constant K_1 from positive above T_{sr} to negative below T_{sr} is the origin of the spin reorientation. In the vicinity of T_C, the single-ion anisotropy is expected to vary as M_s^3, where M_s is the spontaneous magnetization[2]. It becomes negligible compared with the two-ion, magnetic dipole contribution, which varies as M_s^2, but also favors the c-axis[6]. Both contributions tend to zero at T_c.

Previous ac susceptibility studies of Gd have focussed on the temperature range near T_c where a shoulder or maximum in the real component was reported for polycrystalline samples[7]. A single crystal studied by Aliev *et al*[8] showed a shallow peak in the real component of susceptibility when the field was applied perpendicular to the c axis, but no peak was seen in the parallel direction. A recent study of another crystal by Dan'kov *et al*[9] including measurements in a dc bias field, showed no peak, but the parallel susceptibility saturated at T_C. A maximum of the temperature dependence of susceptibility related to the spin reorientation transition at T_{sr} has been reported[10]. In c-plane thin films there is a sharp susceptibility peak at T_c[11] and another susceptibility maximum below T_c depending on the film thickness[12], which has been related to competing shape and c-axis anisotropy terms. In most of these studies, including those on the single crystals, the susceptibility is reported in relative units. Furthermore, many of the measurements, other than those on thin films, were clearly limited by saturation of the susceptibility due to the demagnetising field, giving susceptibility curves which are featureless and lacking in information. A detailed study by Srinath *et al*[13] of the critical behavior of gadolinium uses crystals with demagnetizing factors N = 0.3.

Here we present the ac susceptibility of long thin samples of a Gd crystal cut parallel or perpendicular to the hexagonal c-axis. The susceptibility diverges at the spin reorientation temperature T_{sr} = 225 K, but there is no

divergence of the susceptibility in either direction at T_C. The data suggest that the order between T_{sr} and T_C is not truly ferromagnetic.

A.2 EXPERIMENTAL DETAILS

The temperature dependence of the ac susceptibility of a Gd single crystal, in absolute units, was measured using a system of compensated concentric coils. Two thin bars with approximate dimensions 4.3 x 0.4 x 0.2 mm^3, and 5.9 x 0.4 x 0.2 mm^3 were cut from the crystal; in the first one the long dimension coincides with the hexagonal c-axis, whereas in the second it is in the basal plane. Demagnetizing factors, N, are 0.015(1) and 0.011(1), respectively. The quality of the c-axis crystal was checked by taking Laue patterns at several positions along the long axis. These patterns revealed no variation in the c-axis direction and only a 1 - 2° spread in the basal plane at one end of the crystal.

The temperature dependence (80 K - 300 K) of both real χ' and imaginary χ'' components of ac susceptibility $\chi = \chi' - i\chi''$ have been measured on warming in fields of 8, 80, and 800 A/m at fixed frequencies of 10 Hz, 100 Hz, and 1 kHz. The ac field was applied along the long dimension in order to minimize the demagnetizing field. The Earth's magnetic field of 50 A/m directed at about 30° to the applied ac field direction, was compensated using Helmholz coils in some of the measurements. The effect of a superimposed 50 Hz field of 50 A/m was also investigated. Dimensionless SI volume susceptibility was calculated from the sample mass and density. CGS susceptibility is smaller by a factor of 4π.

A.3 RESULTS AND DISCUSSION

The temperature dependence of the real component $\chi'(T)$ of external susceptibility is shown on Figure A.1. The external susceptibility is the susceptibility in the external applied field, uncorrected for demagnetizing effects. When measured parallel to the c axis $\chi'_{\|}(T)$ shows only a shoulder in at T_c where the value is about 10. $\chi'_{\|}(T)$ increases at lower temperature reaching the value of 65 at 230 K which is essentially the saturation value; the curve is concave. When the field is applied perpendicular to the c axis the

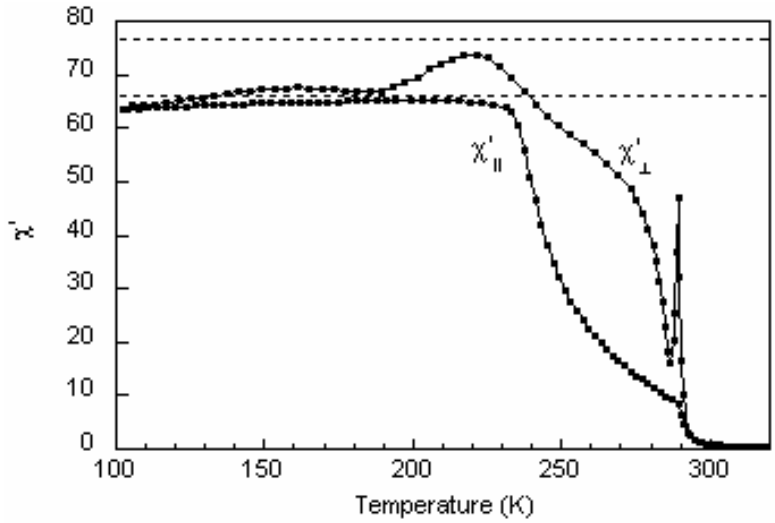

Figure A.1. Real and imaginary parts of the external susceptibility measured on a crystal of Gd parallel(||) and perpendicular (⊥) to the c-axis. The susceptibility is independent of frequency in the range 10 Hz to 1 kHz and field in the range 8 A/m to 800 A/m. The horizontal dotted lines indicate the saturation values expected from the sample shape.

behavior is quite different. $\chi'_{\perp}(T)$ increases rapidly at the magnetic transition exhibiting a sharp peak at 291 K with a peak value of 49(4). With further decrease of temperature the susceptibility increases from a value of 15 at about 286 K to a maximum value of 71, the $\chi'_{\perp}(T)$ curve being convex. After the broad maximum at about 220 K $\chi'_{\perp}(T)$ changes little with decreasing temperature below 190 K. Figure 2 illustrates the components χ' and χ'' for the two directions in the vicinity of T_c after correction for the demagnetizing effect[14]. In the parallel case, where $\chi'_{\parallel}$ only reaches 10 at T_C, $\chi''_{\parallel}$ is zero within the experimental error.

The absence of any divergence in the susceptibility at T_c is obvious. In order to see if domain wall pinning was related to the observed non-divergence of the c-axis susceptibility, a 50 Hz ac bias field of 80 A/m was applied to mobilize the domain walls. However, the form of χ' and χ'' did not change. The peak in the perpendicular susceptibility, $\chi'_{\perp}(T)$, at the magnetic transition is accompanied by a small peak in the $\chi''_{\perp}(T)$ component with a peak value 3. No frequency dependence was found for either direction in the range 10 Hz – 1 kHz.

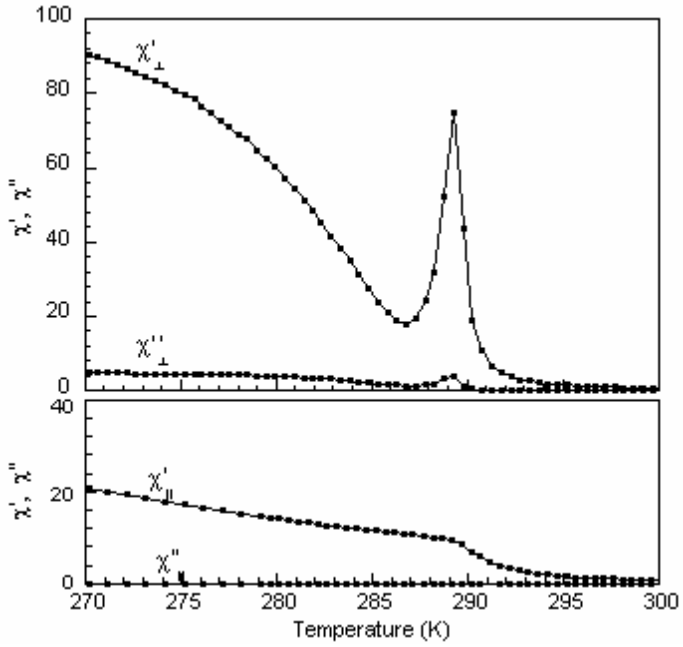

Figure A.2. Internal susceptibility parallel(||) and perpendicular (⊥) to the c-axis of Gd in the vicinity of T_C, corrected for demagnetizing effect. There is no frequency dependence in the range 10 Hz – 1 kHz and no field dependence in the range 8 – 800 A/m.

Before discussing these results we recall the behaviour normally expected for a uniaxial ferromagnet. Approaching T_C from above the susceptibility diverges as $\varepsilon^{-\gamma}$ where $\varepsilon = (T - T_c)/T_c$ and γ is a critical exponent. Below T_C, the critical divergence, $\chi \sim |\varepsilon|^{-\gamma'}$, has the same exponent ($\gamma'=\gamma$). The value of γ is 1.39 for no anisotropy (Heisenberg model) and 1.24 for uniaxial anisotropy (Ising model). Mean field theory gives $\gamma = 1$. The domain structure which appears as M and K_1 grow below T_C should also be taken into account when considering the susceptibility of the ferromagnetic state. The magnetization of the domains lies along the easy axis. For field applied parallel to this axis the susceptibility is limited by domain wall displacement and it will be given by Kersten's formula[15]

$$\chi_{\|} = Sl^2\mu_0 M_s^2/3\gamma_B \approx M_s/K_1^{1/2} \qquad (A.1)$$

where S is the area of mobile or deformable walls per unit volume, l is the wavelength of stress variation of the wall, and γ_B is the domain-wall energy density. Because of the temperature dependence of $K_1 \approx M_s^n$, where n $\approx 2–3$ near T_C, the parallel susceptibility often exhibits a Hopkinson maximum

somewhat below T_C. When the field is applied perpendicular to the ferromagnetic axis, susceptibility will be almost solely governed by domain magnetization rotation processes and is given by

$$\chi_\perp = \mu_0 M_s^2 / 2K_1. \qquad (A.2)$$

Moreover, the anisotropy is negligible close to T_C, or close to a spin reorientation transition so the applied field direction rather than anisotropy then determines the ferromagnetic axis. In any case, whatever the value or nature of the anisotropy, the susceptibility of a ferromagnet is expected to diverge at the Curie temperature in sufficiently small fields. In real samples, the divergence is limited by demagnetizing effect, so the external susceptibility should saturate at a value 1/N.

From the crystals cut with their long axis parallel and perpendicular to c the expected saturated values of $\chi'(T)$ are 66 and 77 respectively. The susceptibility of our Gd crystal indeed reaches these values at the spin reorientation transition at 235 K, but not at the Curie point at 291 K; the c-axis susceptibility is only 10 at T_C. The data with the 50 Hz modulated field is identical to the data without the superimposed field, indicating that $\chi_\parallel$ is not limited by domain wall pinning. The sharp peak observed at T_C when the field is applied in the basal plane strongly resembles the peak at the Néel point T_N = 230 K of Tb, where an in-plane helical structure is established[16] and χ' reaches a value of 8. Terbium itself has recently been shown to have a very long period structure below 223 K, at least in thick, single crystal films[17]. It appears that near T_C, in the absence of magnetocrystalline anisotropy, when a sample can be magnetized in-plane the susceptibility of Gd resembles that of a long-period helix rather than a true ferromagnet.

The value of the exchange stabilization energy of the helix $J(q_m)$-$J(0)$ may be estimated from the peak susceptibility using the expression[18]

$$\chi_{max} = \mu_0 N m^2 / (S^2 (J(q_m) - J(0))) \qquad (A.3)$$

where m is the atomic moment of Gd and S = 7/2. χ_{max} = 75 gives $J(q_m)$-$J(0)$ = 0.013 K. Extrapolating data from the heavy rare earths, where $J(q_m)$-$J(0) \sim q_m^4$, we estimate q_m = 0.029 Å^{-1} and the wavelength of the modulated structure λ_m is 70 Å.

Thus, when the field is applied along the c axis of gadolinium, the magnetic order is expected to be modulated at this wavelength in a longitudinal-wave structure, like that found in Er between 85 and 53.5 K, where $\lambda_m \approx$ 20 Å. The parallel susceptibility of Gd resembles that of Er near T_N where χ' is smaller but there is also a change in slope but no peak[19]. We suggest that this is actually the stable magnetically ordered state in Gd just below T_C, and on reducing the temperature towards T_{sr} the wavelength increases and the longitudinal-wave structure progressively squares up, under the influence of the c-axis anisotropy.

On the question why earlier measurements of the susceptibility of Gd did not reveal the nonferromagnetic behaviour, it should be noted that much of the data were recorded on samples with $0.1 \leq N \leq 0.3$, for which χ' saturates at a value less than 10, and the features in Fig.1 cannot be observed[9]. In other cases the data have been normalized, or given in arbitrary units[20]. Only thin films show an effectively divergent susceptibility, which suggests that ferromagnetism can be stabilized in these samples. It is now a challenge to examine single crystal gadolinium close to T_C by techniques that could observe a long-period modulated structure directly, and confirm that the fourth ferromagnetic element is really not quite ferromagnetic in the bulk.

A.4 SINCE THEN…

Kaul and Srinath later argued against the hypothesis of a modulated spin structure in Gadolinium[21]. They present data that shows the expected behavior for a ferromagnet. However, their data is for cube shaped crystals. These crystals have a larger demagnetization factor than our needles, and hence a much lower demagnetization limit. This makes it impossible for Kaul and Srinath to observe the features we have seen.

A magnetic X-ray diffraction experiment performed on Gd single crystals at the European Synchrotron Radiation Facility (ESRF) was inconclusive. A peak in energy was observed while sitting on the Bragg peak, i.e. q = 0. This peak occurred at about the right energy for a quadrupole

resonance. This suggests that the peak might have been ferromagnetic resonance diffraction. This is unlikely because ferromagnetic resonance diffraction has never been observed because of high background signals from the Bragg peak. Also, the peak had anomalous temperature dependence. So, it is unclear whether the observation is true or due to some experimental error.

More recently, J. Collingwood has observed results more similar to ours for needle shaped Gd crystals[22]. In fact, the shape of her data is the same as ours, with the lack of divergence at Tc. But, opposite to our results, she observes a small peak in $\chi'_{\parallel}(T)$ and only a shoulder in $\chi'_{\perp}(T)$. The reason for this is still unexplained (crystal orientation for all needles has been double checked), but it does show that the spin structure of Gadolinium is still an open question.

---

[1] Coey, J.M.D., V. Skumryev, and K. Gallagher, "Is gadolinium really ferromagnetic?" *Nature* **401** (1999), 35-36

[2] J. Jensen, P. R. Macintosh, Rare Earth Magnetism, Oxford University Press, (1991).

[3] K. P. Belov and A. L. Pedko, Zh. Eksper. Theor. Fiz. 47, 87 (1962) (English transl.: Soviet. Phys.-JETP 15, 62 (1962)).

[4] J. W. Cable and E. O. Wollan, Phys.Rev. 165, 733 (1968).

[5] W. D. Corner, W. C. Roe, K. N. R. Taylor, Proc. Phys. Soc. (London) 80, 927 (1962); and C. D. Graham, Jr., J. Appl. Phys. 38, 1375 (1967); and W. D. Corner, B. K.Tanner, J. Phys.C: Solid State Phys. 9, 627 (1976).

[6] D. J. W. Geldart, P. Hargraves, N. M. Fujiki, R. A. Dunlap, Phys. Rev. Lett. 62, 2728 (1989).

[7] K. R. Sydney, G. V. H. Wilson, D. H. Chaplin, T. J. McKenna, J. Phys. F: Metal Phys. 4, L99 (1974).

[8] Kh. K. Aliev, I. K. Kamilov, A. M. Omarov, Zh. Eksp. Teor. Fiz. 94, 153 (1988) (English transl.: Soviet. Phys.-JETP 67, 2262 (1988)).

[9] S. Yu. Dan'kov, A. M. Tishin, V. K. Pecharsky, K. A. Gschneider, Jr., Phys.Rev.B 57, 3478 (1998).

[10] F. Milstein, L. B. Robinson, Phys. Rev. 177, 904 (1969).

[11] U. Stetter, M. Farle, K. Baberschke, W. G. Clark, Phys. Rev. B 45, 503 (1992); and A. Aspelmeier, F.Gerhardter, K. Baberschke, J. Magn. Magn. Matter. 132, 22 (1994).

[12] A. Berger, A. W. Pang, H. Hopster, J. Magn. Magn. Matter. 1137, L1 (1994).

[13] S. Srinath, S. N. Kaul, H. Kronmüller, Phys. Rev. B. 59, 1145 (1999).

[14] D.-X. Chen, A. Sanchez, J.Appl.Phys. 70, 5463 (1991).

[15] S. Chikazumi, Physics of Ferromagnetism, 2nd ed. (Oxford: Clarendon Press, 1997).

[16] A. del Moral, E. W. Lee, J. Phys. F: Metal Phys. 4, 280 (1974).

[17] C. Dufour, K. Dumesnil, A. Mougin, Ph. Mangin, M. Hennion, J. Phys: Condens. Matter 11, L497-L503 (1999)

[18] Y. Kitano, T. Nagamia, Progr. Theor. Phys., 31, 1 (1964).

[19] H. U. Åström, D.-X.Chen, G. Benediktsson, K. V.Rao, J. Phys.:Condens. Matter 2, 3349 (1990).

[20] K.R. Sydney *et al*; and Kh.K. Aliev *et al;* and F. Milstein and L.B. Robinson.

[21] S.N. Kaul and S. Srinath, "Gadolinium: A helical antiferromagnet or a collinear ferromagnet," Physical Review B 62 no. 2 (2000) 1114-1117.

[22] J. Collingwood, Ph.D. Thesis, University of Warwick.

B APPENDIX: SEQUENCE FILES FOR SQUID

On the SQUID magnetometer, it is necessary to write sequence files to run the experiments. This appendix shows samples of sequences used for measurements in this work. Generally the sequence files were tailored for each sample. Sometimes this meant just changing the datafile names. Other times this meant modifying the program to take a lot of points in the range of the coercivity, or to spread recoil curves evenly over the loop. Datafile names here are only examples.

B.1 SEQUENCE FOR HYSTERESIS MEASUREMENT

Sequence file: demag2.seq

```
Set Datafile: C:\QdMpms\Data\katie\Sm1411
Set Temperature 300.000K at 10.000K/min.
Waitfor Temp:Stable Delay:10secs
Scan Field from 50000.00Oe to 10000.00 Oe in -4000.00 Oe
     increments (11 steps) Hysteresis Mode
     Measure RSO: 1.00 cm, 5 cyc, 1 meas, 4.0 Hz, Center,
          AutoRng, Long, Iterative Reg., track:Yes, raw:No,
          diag:No
End Scan
Scan Field from 5000.00 Oe to -5000.00 Oe in 6 steps (-2000.00
     Oe/step) Hysteresis Mode
     Measure RSO: 1.00 cm, 5 cyc, 1 meas, 4.0 Hz, Center,
          AutoRng, Long, Iterative Reg., track:Yes, raw:No,
          diag:No
End Scan
Scan Field from -7500.00 Oe to -25000.00 Oe in 25 steps (-
     729.17 Oe/step) Hysteresis Mode
     Measure RSO: 1.00 cm, 5 cyc, 1 meas, 4.0 Hz, Center,
          AutoRng, Long, Iterative Reg., track:Yes, raw:No,
          diag:No
End Scan
Scan Field from -27000.00 Oe to -50000.00 Oe in 10 steps (-
     2555.56 Oe/step) Hysteresis Mode
     Measure RSO: 1.00 cm, 5 cyc, 1 meas, 4.0 Hz, Center,
          AutoRng, Long, Iterative Reg., track:Yes, raw:No,
          diag:No
End Scan
Set Magnetic Field 0.00 Oe, No Overshoot, Hi Res Enabled
Magnet Reset
```

B.2 SEQUENCES FOR RECOIL AND VISCOSITY MEASUREMENTS

B.2.1 Main Sequence

Sequence file: bigprogram.seq

```
Set Temperature 300.000K at 10.000K/min.
Waitfor Temp:Stable Delay:5secs
Set Datafile: C:\QdMpms\Data\katie\recoil\Sm1411_300
Run Sequence: C:\QdMpms\Data\katie\virgin.seq
```

```
Run Sequence: C:\QdMpms\Data\katie\recoilloop300.seq
Set Magnetic Field 0.00 Oe, Hysteresis Mode,
Set Temperature 200.000K at 10.000K/min.
Waitfor Temp:Stable Field:Stable Delay:5secs
Set Datafile: C:\QdMpms\Data\katie\recoil\Sm1411_200
Run Sequence: C:\QdMpms\Data\katie\recoilloop200.seq
Set Magnetic Field 0.00 Oe, Hysteresis Mode,
Set Temperature 100.000K at 10.000K/min.
Waitfor Temp:Stable Field:Stable Delay:5secs
Set Datafile: C:\QdMpms\Data\katie\recoil\Sm1411_100
Run Sequence: C:\QdMpms\Data\katie\recoilloop100.seq
Set Magnetic Field 0.00 Oe, Hysteresis Mode,
Set Temperature 375.000K at 10.000K/min.
Waitfor Temp:Stable Field:Stable Delay:5secs
Set Datafile: C:\QdMpms\Data\katie\recoil\Sm1411_375
Run Sequence: C:\QdMpms\Data\katie\recoilloop375.seq
Set Magnetic Field 0.00 Oe, Hysteresis Mode,
Set Temperature 300.000K at 10.000K/min.
Waitfor Temp:Stable Field:Stable Delay:5secs
Set Temperature 10.000K at 10.000K/min.
Waitfor Temp:Stable Delay:5secs
Set Temperature 5.000K at 2.000K/min.
```

B.2.2 Sub-Sequences

Sequence file: virgin.seq

```
Scan Field from 0.00Oe to 18000.00 Oe in 750.00 Oe increments
     (25 steps) Hysteresis Mode
     Measure RSO: 1.00 cm, 5 cyc, 1 meas, 4.0 Hz, Center,
          AutoRng, Long, Iterative Reg., track:Yes, raw:No,
          diag:No
End Scan
Scan Field from 19000.00 Oe to 50000.00 Oe in 5 steps (7750.00
     Oe/step) Hysteresis Mode
     Measure RSO: 1.00 cm, 5 cyc, 1 meas, 4.0 Hz, Center,
          AutoRng, Long, Iterative Reg., track:Yes, raw:No,
          diag:No
End Scan
```

Sequence file: recoilloop300.seq (recoilloop*.seq are all similar to this)

```
Scan Field from 50000.00 Oe to 0.00 Oe in 11 steps (-5000.00
     Oe/step) Hysteresis Mode
     Measure RSO: 1.00 cm, 5 cyc, 1 meas, 4.0 Hz, Center,
          AutoRng, Long, Iterative Reg., track:Yes, raw:No,
          diag:No
End Scan
Scan Field from -1000.00 Oe to -8000.00 Oe in 8 steps (-1000.00
     Oe/step) Hysteresis Mode
     Measure RSO: 1.00 cm, 5 cyc, 1 meas, 4.0 Hz, Center,
          AutoRng, Long, Iterative Reg., track:Yes, raw:No,
          diag:No
End Scan
Set Magnetic Field -9000.00 Oe, Hysteresis Mode,
Waitfor Field:Stable Delay:0secs
Run Sequence: C:\QdMpms\Data\katie\viscosity.seq
Scan Field from -9000.00 Oe to 0.00 Oe in 8 steps (1285.71
     Oe/step) Hysteresis Mode
```

```
     Measure RSO: 1.00 cm, 5 cyc, 1 meas, 4.0 Hz, Center,
          AutoRng, Long, Iterative Reg., track:Yes, raw:No,
          diag:No
End Scan
Scan Field from -1285.71 Oe to -9000.00 Oe in 7 steps (-1285.71
     Oe/step) Hysteresis Mode
     Measure RSO: 1.00 cm, 5 cyc, 1 meas, 4.0 Hz, Center,
          AutoRng, Long, Iterative Reg., track:Yes, raw:No,
          diag:No
End Scan
Scan Field from -9500.00 Oe to -10500.00 Oe in 2 steps (-
     1000.00 Oe/step) Hysteresis Mode
     Measure RSO: 1.00 cm, 5 cyc, 1 meas, 4.0 Hz, Center,
          AutoRng, Long, Iterative Reg., track:Yes, raw:No,
          diag:No
End Scan
Set Magnetic Field -11000.00 Oe, Hysteresis Mode,
Waitfor Field:Stable Delay:0secs
Run Sequence: C:\QdMpms\Data\katie\viscosity.seq
Scan Field from -11000.00 Oe to 0.00 Oe in 10 steps (1222.22
     Oe/step) Hysteresis Mode
     Measure RSO: 1.00 cm, 5 cyc, 1 meas, 4.0 Hz, Center,
          AutoRng, Long, Iterative Reg., track:Yes, raw:No,
          diag:No
End Scan
Scan Field from -1222.22 Oe to -11000.00 Oe in 9 steps (-
     1222.22 Oe/step) Hysteresis Mode
     Measure RSO: 1.00 cm, 5 cyc, 1 meas, 4.0 Hz, Center,
          AutoRng, Long, Iterative Reg., track:Yes, raw:No,
          diag:No
End Scan
Scan Field from -11400.00 Oe to -11800.00 Oe in 2 steps (-
     400.00 Oe/step) Hysteresis Mode
         Measure RSO: 1.00 cm, 5 cyc, 1 meas, 4.0 Hz, Center,
          AutoRng, Long, Iterative Reg., track:Yes, raw:No,
          diag:No
End Scan
Set Magnetic Field -12000.00 Oe, Hysteresis Mode,
Waitfor Field:Stable Delay:0secs
Run Sequence: C:\QdMpms\Data\katie\viscosity.seq
Scan Field from -12000.00 Oe to 0.00 Oe in 10 steps (1333.33
     Oe/step) Hysteresis Mode
     Measure RSO: 1.00 cm, 5 cyc, 1 meas, 4.0 Hz, Center,
          AutoRng, Long, Iterative Reg., track:Yes, raw:No,
          diag:No
End Scan
Scan Field from -1333.33 Oe to -12000.00 Oe in 9 steps (-
     1333.33 Oe/step) Hysteresis Mode
     Measure RSO: 1.00 cm, 5 cyc, 1 meas, 4.0 Hz, Center,
          AutoRng, Long, Iterative Reg., track:Yes, raw:No,
          diag:No
End Scan
Scan Field from -12400.00 Oe to -12800.00 Oe in 2 steps (-
     400.00 Oe/step) Hysteresis Mode
     Measure RSO: 1.00 cm, 5 cyc, 1 meas, 4.0 Hz, Center,
          AutoRng, Long, Iterative Reg., track:Yes, raw:No,
          diag:No
End Scan
Set Magnetic Field -13000.00 Oe, Hysteresis Mode,
Waitfor Field:Stable Delay:0secs
```

```
Run Sequence: C:\QdMpms\Data\katie\viscosity.seq
Scan Field from -13000.00 Oe to 0.00 Oe in 11 steps (1300.00
     Oe/step) Hysteresis Mode
     Measure RSO: 1.00 cm, 5 cyc, 1 meas, 4.0 Hz, Center,
          AutoRng, Long, Iterative Reg., track:Yes, raw:No,
          diag:No
End Scan
Scan Field from -1300.00 Oe to -13000.00 Oe in 10 steps (-
     1300.00 Oe/step) Hysteresis Mode
     Measure RSO: 1.00 cm, 5 cyc, 1 meas, 4.0 Hz, Center,
          AutoRng, Long, Iterative Reg., track:Yes, raw:No,
          diag:No
End Scan
Scan Field from -13400.00 Oe to -13800.00 Oe in 2 steps (-
     400.00 Oe/step) Hysteresis Mode
     Measure RSO: 1.00 cm, 5 cyc, 1 meas, 4.0 Hz, Center,
          AutoRng, Long, Iterative Reg., track:Yes, raw:No,
          diag:No
End Scan
Set Magnetic Field -14000.00 Oe, Hysteresis Mode,
Waitfor Field:Stable Delay:0secs
Run Sequence: C:\QdMpms\Data\katie\viscosity.seq
Scan Field from -14000.00 Oe to 0.00 Oe in 12 steps (1272.73
     Oe/step) Hysteresis Mode
     Measure RSO: 1.00 cm, 5 cyc, 1 meas, 4.0 Hz, Center,
          AutoRng, Long, Iterative Reg., track:Yes, raw:No,
          diag:No
End Scan
Scan Field from -1272.73 Oe to -14000.00 Oe in 11 steps (-
     1272.73 Oe/step) Hysteresis Mode
     Measure RSO: 1.00 cm, 5 cyc, 1 meas, 4.0 Hz, Center,
          AutoRng, Long, Iterative Reg., track:Yes, raw:No,
          diag:No
End Scan
Scan Field from -14400.00 Oe to -14800.00 Oe in 2 steps (-
     400.00 Oe/step) Hysteresis Mode
     Measure RSO: 1.00 cm, 5 cyc, 1 meas, 4.0 Hz, Center,
          AutoRng, Long, Iterative Reg., track:Yes, raw:No,
          diag:No
End Scan
Set Magnetic Field -15000.00 Oe, Hysteresis Mode,
Waitfor Field:Stable Delay:0secs
Run Sequence: C:\QdMpms\Data\katie\viscosity.seq
Scan Field from -15000.00 Oe to 0.00 Oe in 12 steps (1363.64
     Oe/step) Hysteresis Mode
     Measure RSO: 1.00 cm, 5 cyc, 1 meas, 4.0 Hz, Center,
          AutoRng, Long, Iterative Reg., track:Yes, raw:No,
          diag:No
End Scan
Scan Field from -1363.64 Oe to -15000.00 Oe in 11 steps (-
     1363.64 Oe/step) Hysteresis Mode
     Measure RSO: 1.00 cm, 5 cyc, 1 meas, 4.0 Hz, Center,
          AutoRng, Long, Iterative Reg., track:Yes, raw:No,
          diag:No
End Scan
Scan Field from -15400.00 Oe to -15800.00 Oe in 2 steps (-
     400.00 Oe/step) Hysteresis Mode
     Measure RSO: 1.00 cm, 5 cyc, 1 meas, 4.0 Hz, Center,
          AutoRng, Long, Iterative Reg., track:Yes, raw:No,
          diag:No
```

```
End Scan
Set Magnetic Field -16000.00 Oe, Hysteresis Mode,
Waitfor Field:Stable Delay:0secs
Run Sequence: C:\QdMpms\Data\katie\viscosity.seq
Scan Field from -16000.00 Oe to 0.00 Oe in 13 steps (1333.33
     Oe/step) Hysteresis Mode
     Measure RSO: 1.00 cm, 5 cyc, 1 meas, 4.0 Hz, Center,
          AutoRng, Long, Iterative Reg., track:Yes, raw:No,
          diag:No
End Scan
Scan Field from -1333.33 Oe to -16000.00 Oe in 12 steps (-
     1333.33 Oe/step) Hysteresis Mode
     Measure RSO: 1.00 cm, 5 cyc, 1 meas, 4.0 Hz, Center,
          AutoRng, Long, Iterative Reg., track:Yes, raw:No,
          diag:No
End Scan
Scan Field from -16400.00 Oe to -16800.00 Oe in 2 steps (-
     400.00 Oe/step) Hysteresis Mode
     Measure RSO: 1.00 cm, 5 cyc, 1 meas, 4.0 Hz, Center,
          AutoRng, Long, Iterative Reg., track:Yes, raw:No,
          diag:No
End Scan
Set Magnetic Field -17000.00 Oe, Hysteresis Mode,
Waitfor Field:Stable Delay:0secs
Run Sequence: C:\QdMpms\Data\katie\viscosity.seq
Scan Field from -17000.00 Oe to 0.00 Oe in 14 steps (1307.69
     Oe/step) Hysteresis Mode
     Measure RSO: 1.00 cm, 5 cyc, 1 meas, 4.0 Hz, Center,
          AutoRng, Long, Iterative Reg., track:Yes, raw:No,
          diag:No
End Scan
Scan Field from -1307.69 Oe to -17000.00 Oe in 13 steps (-
     1307.69 Oe/step) Hysteresis Mode
     Measure RSO: 1.00 cm, 5 cyc, 1 meas, 4.0 Hz, Center,
          AutoRng, Long, Iterative Reg., track:Yes, raw:No,
          diag:No
End Scan
Scan Field from -17500.00 Oe to -18500.00 Oe in 2 steps (-
     1000.00 Oe/step) Hysteresis Mode
     Measure RSO: 1.00 cm, 5 cyc, 1 meas, 4.0 Hz, Center,
          AutoRng, Long, Iterative Reg., track:Yes, raw:No,
          diag:No
End Scan
Set Magnetic Field -19000.00 Oe, Hysteresis Mode,
Waitfor Field:Stable Delay:0secs
Run Sequence: C:\QdMpms\Data\katie\viscosity.seq
Scan Field from -19000.00 Oe to 0.00 Oe in 15 steps (1357.14
     Oe/step) Hysteresis Mode
     Measure RSO: 1.00 cm, 5 cyc, 1 meas, 4.0 Hz, Center,
          AutoRng, Long, Iterative Reg., track:Yes, raw:No,
          diag:No
End Scan
Scan Field from -1357.14 Oe to -19000.00 Oe in 14 steps (-
     1357.14 Oe/step) Hysteresis Mode
     Measure RSO: 1.00 cm, 5 cyc, 1 meas, 4.0 Hz, Center,
          AutoRng, Long, Iterative Reg., track:Yes, raw:No,
          diag:No
End Scan
Scan Field from -19500.00 Oe to -20500.00 Oe in 2 steps (-
     1000.00 Oe/step) Hysteresis Mode
```

```
     Measure RSO: 1.00 cm, 5 cyc, 1 meas, 4.0 Hz, Center,
          AutoRng, Long, Iterative Reg., track:Yes, raw:No,
          diag:No
End Scan
Set Magnetic Field -21000.00 Oe, Hysteresis Mode,
Waitfor Field:Stable Delay:0secs
Run Sequence: C:\QdMpms\Data\katie\viscosity.seq
Scan Field from -21000.00 Oe to 0.00 Oe in 17 steps (1312.50
     Oe/step) Hysteresis Mode
Measure RSO: 1.00 cm, 5 cyc, 1 meas, 4.0 Hz, Center, AutoRng,
     Long, Iterative Reg., track:Yes, raw:No, diag:No
End Scan
Scan Field from -1312.50 Oe to -21000.00 Oe in 16 steps (-
     1312.50 Oe/step) Hysteresis Mode
     Measure RSO: 1.00 cm, 5 cyc, 1 meas, 4.0 Hz, Center,
          AutoRng, Long, Iterative Reg., track:Yes, raw:No,
          diag:No
End Scan
Scan Field from -21500.00 Oe to -24500.00 Oe in 4 steps (-
     1000.00 Oe/step) Hysteresis Mode
     Measure RSO: 1.00 cm, 5 cyc, 1 meas, 4.0 Hz, Center,
          AutoRng, Long, Iterative Reg., track:Yes, raw:No,
          diag:No
End Scan
Set Magnetic Field -25000.00 Oe, Hysteresis Mode,
Waitfor Field:Stable Delay:0secs
Run Sequence: C:\QdMpms\Data\katie\viscosity.seq
Scan Field from -25000.00 Oe to 0.00 Oe in 20 steps (1315.79
     Oe/step) Hysteresis Mode
     Measure RSO: 1.00 cm, 5 cyc, 1 meas, 4.0 Hz, Center,
          AutoRng, Long, Iterative Reg., track:Yes, raw:No,
          diag:No
End Scan
Scan Field from -1315.79 Oe to -25000.00 Oe in 19 steps (-
     1315.79 Oe/step) Hysteresis Mode
     Measure RSO: 1.00 cm, 5 cyc, 1 meas, 4.0 Hz, Center,
          AutoRng, Long, Iterative Reg., track:Yes, raw:No,
          diag:No
End Scan
Scan Field from -25500.00 Oe to -50000.00 Oe in 12 steps (-
     2227.27 Oe/step) Hysteresis Mode
     Measure RSO: 1.00 cm, 5 cyc, 1 meas, 4.0 Hz, Center,
          AutoRng, Long, Iterative Reg., track:Yes, raw:No,
          diag:No
End Scan
Set Magnetic Field 0.00 Oe, Hysteresis Mode,
Waitfor Field:Stable Delay:5secs
```

Sequence file:viscosity.seq

```
Measure RSO: 1.00 cm, 5 cyc, 1 meas, 4.0 Hz, Center, AutoRng,
     Long, Iterative Reg., track:Yes, raw:No, diag:No
Waitfor Delay:5secs
Measure RSO: 1.00 cm, 5 cyc, 1 meas, 4.0 Hz, Center, AutoRng,
     Long, Iterative Reg., track:Yes, raw:No, diag:No
Waitfor Delay:5secs
Measure RSO: 1.00 cm, 5 cyc, 1 meas, 4.0 Hz, Center, AutoRng,
     Long, Iterative Reg., track:Yes, raw:No, diag:No
Waitfor Delay:5secs
```

```
Measure RSO: 1.00 cm, 5 cyc, 1 meas, 4.0 Hz, Center, AutoRng,
     Long, Iterative Reg., track:Yes, raw:No, diag:No
Waitfor Delay:5secs
Measure RSO: 1.00 cm, 5 cyc, 1 meas, 4.0 Hz, Center, AutoRng,
     Long, Iterative Reg., track:Yes, raw:No, diag:No
Waitfor Delay:5secs
Measure RSO: 1.00 cm, 5 cyc, 1 meas, 4.0 Hz, Center, AutoRng,
     Long, Iterative Reg., track:Yes, raw:No, diag:No
Waitfor Delay:5secs
Measure RSO: 1.00 cm, 5 cyc, 1 meas, 4.0 Hz, Center, AutoRng,
     Long, Iterative Reg., track:Yes, raw:No, diag:No
Waitfor Delay:5secs
Measure RSO: 1.00 cm, 5 cyc, 1 meas, 4.0 Hz, Center, AutoRng,
     Long, Iterative Reg., track:Yes, raw:No, diag:No
Waitfor Delay:5secs
Measure RSO: 1.00 cm, 5 cyc, 1 meas, 4.0 Hz, Center, AutoRng,
     Long, Iterative Reg., track:Yes, raw:No, diag:No
Waitfor Delay:5secs
Measure RSO: 1.00 cm, 5 cyc, 1 meas, 4.0 Hz, Center, AutoRng,
     Long, Iterative Reg., track:Yes, raw:No, diag:No
Waitfor Delay:5secs
Measure RSO: 1.00 cm, 5 cyc, 1 meas, 4.0 Hz, Center, AutoRng,
     Long, Iterative Reg., track:Yes, raw:No, diag:No
Waitfor Delay:5secs
Measure RSO: 1.00 cm, 5 cyc, 1 meas, 4.0 Hz, Center, AutoRng,
     Long, Iterative Reg., track:Yes, raw:No, diag:No
Waitfor Delay:5secs
Measure RSO: 1.00 cm, 5 cyc, 1 meas, 4.0 Hz, Center, AutoRng,
     Long, Iterative Reg., track:Yes, raw:No, diag:No
Waitfor Delay:5secs
Measure RSO: 1.00 cm, 5 cyc, 1 meas, 4.0 Hz, Center, AutoRng,
     Long, Iterative Reg., track:Yes, raw:No, diag:No
Waitfor Delay:5secs
Measure RSO: 1.00 cm, 5 cyc, 1 meas, 4.0 Hz, Center, AutoRng,
     Long, Iterative Reg., track:Yes, raw:No, diag:No
Waitfor Delay:5secs
Measure RSO: 1.00 cm, 5 cyc, 1 meas, 4.0 Hz, Center, AutoRng,
     Long, Iterative Reg., track:Yes, raw:No, diag:No
Waitfor Delay:5secs
Measure RSO: 1.00 cm, 5 cyc, 1 meas, 4.0 Hz, Center, AutoRng,
     Long, Iterative Reg., track:Yes, raw:No, diag:No
Waitfor Delay:5secs
Measure RSO: 1.00 cm, 5 cyc, 1 meas, 4.0 Hz, Center, AutoRng,
     Long, Iterative Reg., track:Yes, raw:No, diag:No
Waitfor Delay:5secs
Measure RSO: 1.00 cm, 5 cyc, 1 meas, 4.0 Hz, Center, AutoRng,
     Long, Iterative Reg., track:Yes, raw:No, diag:No
Waitfor Delay:5secs
Measure RSO: 1.00 cm, 5 cyc, 1 meas, 4.0 Hz, Center, AutoRng,
     Long, Iterative Reg., track:Yes, raw:No, diag:No
Waitfor Delay:5secs
Measure RSO: 1.00 cm, 5 cyc, 1 meas, 4.0 Hz, Center, AutoRng,
     Long, Iterative Reg., track:Yes, raw:No, diag:No
```

C APPENDIX: FIELD PROFILE MEASUREMENTS FOR MAGNETIC WHEELS

C.1 DEFINITIONS

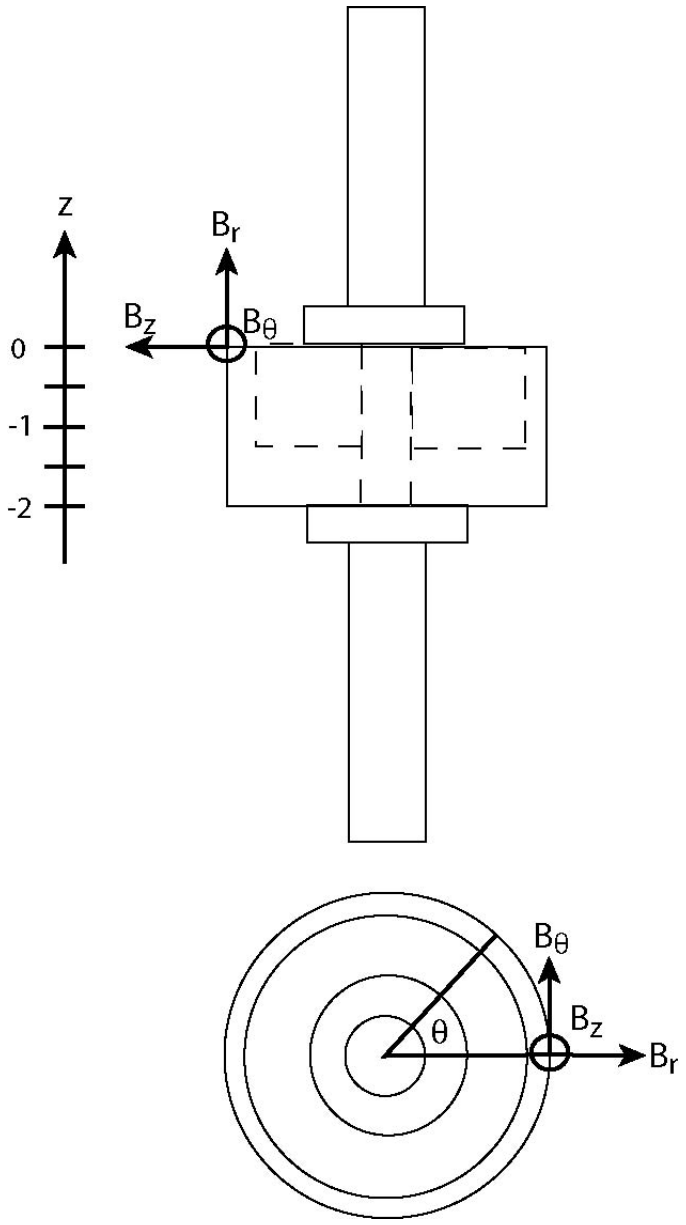

Figure C.1. Definitions for magnetic wheels field profile measurements

C.2 WHEEL 1

θ	B_θ (mT)	B_r (mT)	B_θ (mT)	B_r (mT)	B_θ (mT)	B_r (mT)	B_θ (mT)	B_r (mT)	B_θ (mT)	B_r (mT)
0	3.01	113.2	8.05	197.6	15.14	173.6	10.96	-29.4	-5.87	-209.9
10	5.10	122.3	12.03	208.8	16.32	175.5	8.10	-40.8	-4.10	-193.5
20	3.40	119.0	6.60	200.8	11.85	164.6	8.65	-40.5	1.72	-183.1
30	2.86	106.3	6.35	186.4	10.85	211.1	8.60	-2.9	2.54	-203.4
40	-0.22	106.3	3.57	190.5	9.95	205.5	10.11	10.0	3.69	-183.7
50	2.85	110.6	7.55	193.5	14.91	193.4	9.53	-19.2	0.65	-206.4
60	9.27	110.6	17.89	196.8	21.96	188.0	6.97	-18.8	-11.13	-203.7
70	7.56	116.5	15.69	203.1	19.88	175.7	7.37	-40.1	-8.14	-212.4
80	-0.16	117.5	3.88	202.4	10.81	179.0	11.42	-37.5	5.78	-212.0
90	0.40	114.2	5.78	200.2	12.83	179.1	10.96	-28.5	2.61	-209.1
100	11.15	116.9	21.68	204.0	24.20	176.0	5.75	-33.3	-10.83	-209.7
110	9.72	117.4	18.25	201.7	21.47	176.8	7.01	-35.6	-11.63	-208.4
120	9.15	119.5	18.45	208.7	22.50	186.4	6.83	-43.1	-12.03	-210.2
130	16.87	117.2	30.10	203.2	32.20	177.4	4.35	-44.0	-21.64	-211.5
140	11.31	114.5	21.09	202.4	24.34	168.9	4.80	-43.0	-13.40	-212.0
150	6.02	119.1	13.41	206.2	17.99	172.8	7.15	-50.7	-7.33	-212.0
160	7.03	120.3	15.35	206.9	20.87	162.6	8.81	-47.2	-6.24	-210.5
170	13.96	118.9	26.80	205.1	30.50	167.2	9.46	-51.4	-13.92	-209.9
180	4.75	121.3	11.43	206.5	18.20	163.7	11.46	-49.8	-3.17	-207.9
190	9.50	111.5	19.00	187.1	28.42	166.1	12.22	-29.5	-9.15	-203.6
200	9.03	112.7	18.72	190.9	27.04	177.9	12.76	-27.5	-6.67	-209.9
210	7.37	113.8	16.60	195.4	25.21	176.9	14.06	-26.2	-4.72	-208.9
220	6.20	113.9	14.76	197.0	24.11	175.4	14.83	-30.2	-1.20	-207.5
230	7.54	113.8	16.40	195.3	26.80	184.5	16.77	-18.6	-0.58	-206.7
240	8.00	111.5	18.73	194.4	30.80	183.2	18.12	-20.2	1.16	-205.2
250	9.83	112.7	20.10	195.5	30.20	172.3	16.10	-22.2	-7.80	-204.9
260	9.52	114.2	20.50	196.0	30.80	177.8	16.40	-16.6	-5.13	-204.5
270	5.54	111.1	15.02	195.0	25.95	175.8	15.58	-16.5	-1.44	-201.4
280	9.74	113.0	18.60	193.7	29.85	178.2	15.60	-18.8	-9.10	-199.1
290	15.41	114.2	28.20	195.7	39.30	186.2	14.66	-16.9	-15.55	-203.7
300	10.40	110.4	20.10	198.4	30.40	197.1	15.33	-11.5	-6.85	-202.0
310	4.20	110.7	11.74	195.2	22.78	198.6	15.33	-8.8	-0.15	-205.8
320	-1.00	111.7	2.82	200.2	11.65	198.0	13.82	-13.9	6.87	-205.8
330	12.60	111.8	24.40	198.6	33.40	203.7	14.90	-8.4	-10.60	-205.9
340	8.60	111.0	18.20	192.8	26.20	201.1	13.45	-13.2	-6.98	-203.9
350	8.52	111.1	17.80	195.1	26.50	205.8	13.60	-15.6	-6.00	-206.2

C.3 WHEEL 2

	z=-2		z=-1		z=-0.5		z=0	
θ	B_θ(mT)	B_r(mT)	B_θ(mT)	B_r(mT)	B_θ(mT)	B_r(mT)	B_θ(mT)	B_r(mT)
0	-50.9	12.72	-101.9	174.9	136.5	213.1	-78.4	137.9
10	-46.8	16.01	-96.4	221.1	134.3	264.0	-65.4	171.7
20	-40.8	19.60	-83.6	263.0	126.1	318.0	-52.7	207.3
30	-32.9	20.60	-68.1	296.0	115.0	361.0	-41.1	233.2
40	-25.3	24.10	-51.7	321.0	100.7	393.0	-23.1	252.6
50	-15.7	25.60	-30.9	333.0	81.3	413.0	-6.5	260.8
60	-6.1	24.30	-10.2	333.0	61.8	419.0	10.3	259.7
70	3.3	24.50	9.3	327.0	40.3	411.0	27.0	252.0
80	12.8	22.70	29.3	310.0	15.4	390.0	42.0	237.0
90	22.2	23.00	49.0	285.0	-8.3	358.0	53.5	217.0
100	31.1	19.42	66.7	248.0	-34.2	311.0	67.6	182.7
110	38.5	19.48	81.2	248.0	-58.1	257.0	76.0	185.1
120	44.9	16.34	95.6	208.9	-78.0	202.0	83.9	157.6
130	49.8	13.38	105.2	157.1	-94.5	134.5	87.3	114.6
140	54.0	8.04	111.7	103.0	-108.5	65.4	89.9	71.2
150	55.4	8.97	113.2	101.4	-118.5	-0.3	89.4	74.4
160	55.4	3.69	113.2	44.9	-125.8	-68.4	86.1	31.2
170	54.8	-0.62	110.4	-6.0	-128.6	-134.3	79.7	-6.5
180	51.5	-5.95	103.2	-68.0	-127.1	-205.8	70.8	-52.0
190	46.8	-10.39	93.5	-119.6	-122.0	-262.1	60.7	-88.4
200	40.9	-14.95	81.6	-177.1	-114.4	-315.0	49.6	-130.9
210	32.4	-18.77	63.0	-221.8	-102.4	-359.0	33.9	-160.7
220	20.7	-22.70	34.6	-266.0	-84.5	-390.0	14.9	-185.2
230	11.7	-22.90	14.6	-267.0	-66.6	-408.0	-3.3	-188.3
240	2.6	-25.50	-4.2	-296.0	-47.7	-414.0	-19.4	-210.6
250	-6.6	-25.90	-23.3	-317.0	-31.5	-409.0	-35.5	-235.3
260	-15.3	-26.40	-41.0	-316.0	-8.0	-391.0	-49.6	-221.0
270	-23.6	-24.20	-57.9	-287.0	11.4	-357.0	-63.2	-208.2
280	-31.7	-20.90	-72.6	-246.5	36.1	-315.0	-76.0	-178.5
290	-37.7	-17.61	-84.5	-211.6	57.1	-262.0	-84.1	-150.9
300	-42.9	-13.74	-93.9	-158.6	78.6	-200.0	-91.3	-112.2
310	-46.3	-8.90	-100.8	-104.8	94.9	-138.7	-95.2	-80.0
320	-49.9	-4.23	-105.7	-46.9	109.5	-67.6	-96.9	-34.2
330	-51.6	0.65	-107.5	13.7	121.1	10.2	-95.4	11.8
340	-51.5	5.04	-104.7	72.2	130.2	75.0	-89.4	52.5
350	-49.1	9.30	-101.1	124.4	135.3	143.0	-83.8	97.6
360	-50.9	12.72	-101.9	174.9	136.5	213.1	-78.4	137.9

D PUBLICATIONS RELATED TO THIS WORK

Gallagher, K., M. Venkatesan, and J.M.D. Coey. 2002. High temperature magnetic properties of mechanically-alloyed SmZr(CoFe) nanophase hard magnets. *Proceedings of the Seventeenth International Workshop on Rare Earth Magnets and Their Applications*. Newark, DE. 913-919.

Gallagher, K., A. le Gouil, M. Venkatesan, and J.M.D. Coey. 2002. Structure and magnetic properties of mechanically alloyed SmZr(Co,Fe) nanophase hard magnets. *IEEE Transactions on Magnetics*. in press.

Jiang, C.B., M. Venkatesan, **K. Gallagher**, and J.M.D. Coey. 2001. Magnetic and structural properties of $SmCo_{7-x}Ti_x$ magnets. *J. Magnetism and Magnetic Materials* **236**(1-2): 49-55.

Gallagher, K., M. Venkatesan, and J.M.D. Coey. 2001. Magnetic properties of mechanically-alloyed Sm-Co nanophase hard magnets. *IEEE Transactions on Magnetics* **37**(4):2528-2530.

Coey, J.M.D., **K. Gallagher**., and V. Skumryev. 2000. Alternating current susceptibility of a gadolinium crystal. *J. Appl.Phys.* **87**: 7028-30.

Coey, J.M.D., V. Skumryev, and **K. Gallagher**. 1999. Is gadolinium really ferromagnetic? *Nature* **401**: 35-36